Università degli Studi di Napoli "Federico II", Napoli, Italy

Graduate School of Physical Sciences

Research Doctorate (PhD) in Fundamental and Applied Physics

"Transport Properties of Transition Metal Oxide Thin Films and Interfaces under Light Irradiation"

Muhammad Riaz

Supervisor:
Dr. Fabio Miletto Granozio

A Dissertation submitted for the Degree of Doctor of Philosophy at the University of Naples “Federico II”, Napoli, Italy

November 2011

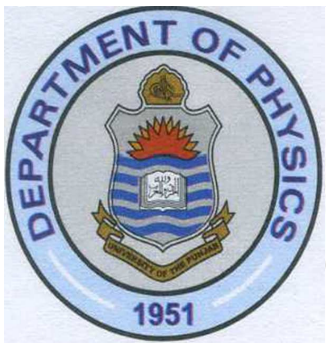


Università degli Studi di Napoli "Federico II", Napoli, Italy
Scuola di dottorato in Scienze Fisiche
Dottorato di Ricerca in Fisica Fondamentale ed Applicata

TESI SPERIMENTALE DI DOTTORATO

"Transport Properties of Transition Metal Oxide Thin Films and Interfaces under Light Irradiation"

Candidato:
Muhammad Riaz

Supervisore:
Dr. Fabio Miletto Granozio
Coordinatore:
Prof. Raffaele Velotta

23° ciclo di Dottorato
di Ricerca in Fisica Fondamentale ed Applicata
Dipartimento di Scienze Fisiche dell'Università di Napoli "Federico II",
Compl. universitario Monte S. Angelo, Via Cintia – I, Napoli, Italy

For my family and parents,
specially my father Niaz Muhammad

"And HE has subjected to you whatever is in the heavens and whatever is on the earth - all from HIM.

Indeed in that are signs for a people who give thought."

Verse 13, Chapter 45, (Al-Quran)

The work described in this thesis was carried out at the department of physical sciences (Physics) and CNR-SPIN laboratories at the Faculty of Engineering and Technology, University of Naples "Federico II", Napoli, Italy. This work is financially supported by University of the Punjab, 54590-Lahore, Pakistan under "Overseas faculty development scholarship program".

Muhammad Riaz
Transport Properties of Transition Metal Oxide Thin Films and Interfaces under Light Irradiation
Ph.D. Thesis University of Naples "Federico II", Napoli, Italy
30-November-2011

Abstract

Complex oxide materials are special in their ability to show highly diverse electronic properties and go through many different phase transitions, including ferromagnetic, ferroelectric, metal-to-insulator and superconducting. Furthermore, the similarity of crystal structures makes it possible to stack in epitaxial heterostructures layers possessing different functional properties and interacting with each other through electric or magnetic fields, charge transfer, exchange bias, strain, etc, opening the way to the design of almost unlimited multifunctional device concepts. In this context, this thesis is devoted to the transport characterization of transition metal oxides (TMOs) under the external perturbation of a photon field, with special attention dedicated to two quite outstanding cases, that are:

i) $Pr_{1-x}Ca_xMnO_3$ (PCMO), a narrow band manganite showing an insulating behaviour across it's whole phase diagram, and

ii) polar-non polar oxide interfaces, where the formation of a high mobility 2-dimensional electron gas (2DEG) in $SrTiO_3$ (STO) is triggered by the deposition of a polar overlayer.

Both systems are correlated systems, since their electronic properties are dominated by the narrow d-bands of the transition metals, Mn and Ti. STO is insulating, but doped STO has *d* carriers. The system is for this reason often defined as a 2-dimensional electron liquid (2DEL). In particular, there is a strong current interest arising on the photoconductance properties of both kinds of systems addressed in this thesis. In the first case it is established that by shedding light we do not simply dope the system with photocarriers within a rigid band picture, but we undisclose a hidden state which is quasi-degenerate in energy with the insulating ground state and has a different distribution of its density of states in k space. The second case might well be envisaged as a simple photodoping of STO, but, as we will show in this thesis work, there are some quite intriguing aspects to consider. The effects seen in interfaces is not seen in pure STO, and – furthermore – persistent photoconductivity (PC) with very long decay times (on the time scale of months) and at photon energies far below the STO gap is found. Also in view of the recently suggested phase separation, we can not exclude that something more complex than photodoping is taking place. In a more general framework, the present investigation may be considered as an attempt to add a tile to the wide mosaic of the physics of inhomogeneous states in TMO.

Certificate

It is certified that the work contained in this thesis entitled “Transport properties of transition metal oxide thin films and interfaces under light irradiation” by Muhammad Riaz, has been carried out under my supervision and that this work has not been submitted elsewhere for a degree.

Dr. Fabio Miletto Granozio
CNR-SPIN and Department of Physics
University of Naples Federico II,
Napoli, Italy

30 November 2011

Acknowledgements

In the beginning, I want to thank Almighty ALLAH for blessing me through out my life. This thesis is the end of my long journey to obtain a PhD degree in Physics. The journey would not have succeeded without the cooperation and encouragement I received all along. The first person I would like to thank is my supervisor, Dr. Fabio Miletto Granozio. I joined him in May 2008 as a doctorate student. His constant guidance, enthusiasm and mission to achieve the best quality results have direct impact on the final form and quality of this work. I owe him lots of gratitude for having me shown this way of research. I will remain indebted to him. I thank him for being both patient and decisive when needed and for the possibility he gave me to know other labs, and very good scientists.

My sincere thanks are due to Prof. Vittorio Cataudella and Prof. Salvatore Amoruso. I am highly indebted to Prof. Umberto Scotti di Uccio of Physics department, Napoli, who assisted me in all the transport characterization and spent hours with me in the lab. fixing many things. He is an excellent scientist and a good friend, I am proud to be his student. I owe my special thanks to Prof. Lorenzo Marrucci (Ex-coordinator) and Prof. Raffaele Velota, the coordinators of the PhD program, for their care during these four years.

I wish to express my sincere thanks to Prof. Antonio Cassinese, Dr. Mario Barra and Prof. Francesco Bloisi. Special thanks to Mario Barra who is an excellent friend and researcher, he assisted me with sputtering of Ag-contacts and PIPT experiments on PCMO thin films together with Prof. Bloisi. I am grateful to my colleagues in engineering department Dr. Giovanni Ausanio and Dr. Emiliano Di Gennaro of CNR-SPIN Napoli for their assistance in high magnetic field measurements. I would like to thank my lab mates Dr. Paolo Perna and Davide. They spared their valuable time and helped me in getting acquainted with various experimental parts of the MODA setup for the PLD deposition. Special thanks are due to Dr. Carmela Aruta for providing me samples always on time and encouraging me in my research work.

I am grateful to my departmental staff for always being supportive both in research and official matters. Especially, I am thankful to the my friend Stefano Marrazzo in engineering

department for being always kind to me and helping me in building up of photoconductivity setup and providing me the cuppor holders of my requirements whenever needed. I would like to thank all my friends; Antonio Scialdone, Ndubuisi OMAGHALI (ND), Lorenzetti, Riccardo, Vitto, Marco, Nicolla, Mario Barra, for their affection, friendly company and cooperation.

This thesis would not have been possible without the support I have received outside the lab. Very special thanks to Guido Celentano for helping me in fight against Administrative problems in and out of University and for his constant supply of solutions to every problem. On a personal note, Guido is an extremely good friend whose friendship I will cherish forever. Unlimited thanks to Prof. Iaia Masullo (Masullo Maria Rosaria) for her care, kindness and love towards my family, I do not have the words to say “thank you Iaia”.

I would like to thank all those from the wonderful city of Napoli who showed their kindness towards me, including dr.ssa Michela Mingione dell'Ospedale SS.Annunziata di Napoli, Paola Celentano and her colleagues from ASL Mergellina and my house owner Mr and Mrs. Rino. I thanks Andrea the student of Iaia for picking us from Napoli to Rome air port at 4.30am in a rainy winter day, we reached exactly on time.

The pleasant stay I had in La Morella, I will never forget, a huge “thank you” to Miletto Family. You all will be in my memory always, for you too I do not have the words to say “Thanks”. I would also take this opportunity to thank all the staff of La Morella for making my stay really comfortable. Special thanks are due to my little friends Enrico and Riccardo for involving me in playing football.

In the end, I would say, whatever little I have achieved would not have been possible without the blessings and good wishes of my elders. I take this opportunity to thank all my past teachers for imparting the knowledge that became the stepping stone for this PhD. I would like to thank all my teachers in “Federico II” university.

It is my pleasure to acknowledge the University of the Punjab, Lahore-54590, Pakistan for sending me in Italy for this PhD study and the financial support they have provided for this research through Overseas Faculty Development Scholarship. Many thanks due to Punjab University’s department of Physics and my colleagues, friends and students over there praying for my success. Special thanks to Dr. Rashid Ali for filling my surety bond.

Finally, my loving thanks go to my wife, my beloved soul, who has shown great understanding and patience towards this work as well as everything else I do. Her patience

and support have helped ease the writing process. My special love and thanks to my kids Zainab and Abdullah for giving me all the happiness of my life, I love you all.

Above everything, this PhD would not have been possible without the constant support, encouragement, blessings and good wishes of my parents. I would never be able to repay their unconditional support and personal sacrifices they made, which made it possible for me to accomplish this task. I gratefully acknowledge my mother, and my father, my brothers and specially my younger sisters for their constant love. There are not enough words in the world to thank them. I also would like to thank my father-in-law and mother-in-law.

Personally I want to thank my parents for the way they educated me. To be persistent even in difficult moments, to work good just for a personal pleasure and to try always to be the best in what you do.

To me I want to thank myself that I didn't gave up even if this step in my life was very difficult, now I seat here and look back…..look my work and I am proud of myself. Proud to see all my effort written in this thesis and I can just say it is a very beautiful work. I dedicate this thesis to my family, my sweet mother and specially my father **Niaz Muhammad**.

In the end, I want to thank once again Almighty ALLAH for all HE puts in my way.

Muhammad Riaz,

Napoli, 30 November 2011

Index

List of Figures

List of Tables

Introduction

Complex oxide materials are special in their ability to show highly diverse electronic properties and go through many different phase transitions, including ferromagnetic, ferroelectric, metal-to-insulator and superconducting. Such multiple order parameters, corresponding to multiple functionalities to be potentially exploited in device fabrication, can be coupled to each other due to the high degree of correlation experienced by the conduction electrons. Furthermore, the similarity of crystal structures makes it possible to stack in epitaxial heterostructures layers possessing different functional properties and interacting with each other through electric or magnetic fields, charge transfer, exchange bias, strain, etc, opening the way to the design of almost unlimited multifunctional device concepts.

In this context, this thesis is devoted to the transport characterization of TMOs under the external perturbation of a photon field, with special attention dedicated to two quite outstanding cases, that are:

i) $Pr_{1-x}Ca_xMnO_3$ (PCMO), a narrow band manganite showing an insulating behaviour across it's whole phase diagram, and

ii) polar-non polar oxide interfaces, where the formation of a high mobility 2-dimensional electron gas (2DEG) in $SrTiO_3$ (STO) is triggered by the deposition of a polar overlayer [1].

Both systems are correlated systems, since their electronic properties are dominated by the narrow d-bands of the transition metals, Mn and Ti. STO is insulating, but doped STO has *d* carriers. The system is for this reason often defined as a 2-dimensional electron liquid (2DEL) [2].

A wide variety of experimental results and theoretical investigations in recent years have convincingly demonstrated that several transition metal oxides and other materials have dominant states that are not spatially homogeneous. According to a recent report by E. Dagoto [3] TMOs are certainly not as simple as standard metals. The many active degrees of freedom (spin, charge, lattice, and orbital) interact in a nonlinear, synergetic manner, leading to an intrinsic complexity. This electronic complexity could have potential consequences for applications of correlated electronic materials, because not only charge (semiconducting

electronics), or charge and spin (spintronics) are of relevance, but in addition the lattice and orbital degrees of freedom are active, leading to giant responses to small perturbations. Moreover, several metallic and insulating phases compete, increasing the potential for novel behavior. Phase competition rules the behavior of these compounds. In view of above context [3], both systems can be considered as “complex”. PCMO is intrinsically “complex”, while a complex behaviour of LAO/STO, although not seen in the single materials, can be envisaged as a result of the interfacial nature of the 2DEG, as suggested by the recently reported electronic phase separation phenomena [4, 2] with possible coexistence of different order parameters (magnetism, superconductivity).

In the last 15 years PCMO, in it’s “borderline” doping level composition $Pr_{0.7}Ca_{0.3}MnO_3$, has become subject of immense research since the first report of magnetic-field-induced insulator-metal transition by Y. Tomioka et al. [5]. The peculiarity of the insulating state of PCMO is quite spectacular since it adjoins a hidden metallic state, characterized by enormous changes in resistivity, that can be reached by application of external stimuli (e.g., magnetic, electric, pressure, or radiation fields (visible light, x-rays)) [5, 6, 7, 8, 9]. Any of these perturbations drives the system to the conductive state, associated with the melting of the charge-ordered and orbitally-ordered state. Though magnetic or pressure induced transitions seems to be homogeneous, there is evidence that electric and radiation fields may cause transitions in phase-separated regions of the system where nucleation of metallic patches in the form of filaments within the system body have been observed [8].

In addition, the celebrated discovery of a two-dimensional electron gas (2DEG) at the interface between two band insulators, e.g., the polar $LaAlO_3$ (LAO) and the nonpolar $SrTiO_3$ (STO), raised great interest for both fundamental and applicative perspectives. 2DEGs (also defined sometimes as 2D electron liquids – 2DEL - to highlight the correlated nature of the charges carriers confined at the STO interface) are probably the most interesting system realized so far using oxide heterostructure technology. The issue of the origin of the 2D electron layer in $SrTiO_3/LaAlO_3$ interfaces has been raised. The main theory, the so-called “polar catastrophe" paradigm, has been extremely controversial since the very beginning and has been challenged by different models invoking extrinsic effects. This scenario is further complicated by the experimental variation of results observed by different research groups. To understand the properties of this system, and to help engineering new conducting heterointerface, clarity is needed about the origin of the conducting charge layer.

During the past few years a great interest has arisen on photoinduced effects in correlated transition metal oxides. Indeed, when shone by only a few visible photons, these solids give rise to a macroscopic excited domain that has new structural, electronic and even magnetic orders quite different from the starting ground state. This phenomenon is called "photoinduced phase transition (PIPT)" and we can generate new long-lived locally stable macroscopic nonequilibrium phases through the excitations or stimulations by a few visible photons [10]. Theoretically, systems with competing degrees of freedom predict the formation of transient hidden phases that can be accessed by optical stimulation in the dynamical processes of PIPTs. In this regard, strongly correlated TMO are promising in searching for PIPTs because they are likely to have hidden phases that are energetically almost degenerate but thermally inaccessible.

In particular, there is a strong current interest arising on the photoconductance properties of both kinds of systems addressed in this thesis, as demonstrated by the recent reports of photoinduced effects in narrow-band manganites [11] and in STO-based interfaces [12]. In the first case it is established that by shedding light we do not simply dope the system with photocarriers within a rigid band picture, but we undisclose a hidden state which is quasi-degenerate in energy with the insulating ground state and has a different distribution of its density of states in k space. The second case might well be envisaged as a simple photodoping of STO, but, as we will show in this thesis work, there are some quite intriguing aspects to consider. The effects seen in interfaces is not seen in pure STO, and – furthermore – persistent photoconductivity (PC) with very long decay times (on the time scale of months) and at photon energies far below the STO gap is found. Also in view of the recently suggested phase separation [4], we can not exclude that something more complex than photodoping is taking place.

Many recent studies have investigated PIPTs and related phenomena, including hidden phases. Most of them used dynamic all-optical spectroscopic measurements to probe the local structural and electronic changes caused by transient states. A complete picture in terms of variable temperature photoconductance is still lacking and is addressed therefore in this work. In a more general framework, the present investigation may be considered as an attempt to add a tile to the wide mosaic of the physics of inhomogeneous states in TMO.

This thesis work was carried out at the laboratories of department of Physics and CNR-SPIN Napoli, Italy. This manuscript is divided into four chapters, in which the

transport properties of TMO thin films and interfaces, also under light irradiation, will be addressed.

- In chapter 1, the main properties of transition metal oxides in the form of current experimental results and theoretical predictions obtained during the last years, will be discussed. In particular, the general characteristics of $Pr_{1-x}Ca_xMnO_3$ (PCMO) manganite compound and novel conducting interfaces of TMO will be described. The brief overview of TMO given in this chapter can provide a starting point to the research work which is explained in the later chapters.
- The experimental setups and procedures of the experiments that took place in this study are summarized in chapter 2. The growth technique, pulsed laser deposition, and reflection high energy electron diffraction are briefly described. In addition, the transport characterization techniques are presented.
- In chapter 3, I report on the transport properties of PCMO manganite characterized both in dark and under UV irradiation. A set of experimental results concerning epitaxial films grown on (001) and (110) $SrTiO_3$ substrates by pulsed laser deposition will be presented, with the aim of adding novel information on the transport properties of the different observed phases. Particular reference will be made to the charge (orbital) ordered CO (OO) phase and to the ferromagnetic-insulating FMI transition occurring in this system also as a function of externals perturbations as the biaxial stress imposed by the substrate or the exposure to a photon field.
- In chapter 4, the attention will be mainly concentrated on analysing and comparing the transport properties of high quality $NdGaO_3/SrTiO_3$, $LaGaO_3/SrTiO_3$ and $LaAlO_3/SrTiO_3$ heterostructures, all hosting a two dimensional electron gas at the interface. The results of transport characterization in dark and the effects induced by UV light illumination will be presented and discussed, also in the framework of the present debate about the origin of interface conductivity in oxides.
- The summary and main conclusions of the thesis are given in a separate, last section.

Chapter 1

Survey of $Pr_{1-x}Ca_xMnO_3$ manganite compound and two-dimensional electron gases in oxide heterostructures

1.1 Strongly correlated materials: the case of transition metal oxides

Strongly correlated electron systems (SCESs) are a wide class of materials that show unusual electronic and magnetic properties. In many cases, transition metal oxides are SCESs, which, although chemically similar, exhibit the full breadth of electronic properties from band insulator, through Mott insulator, semiconductor, metal, to superconductor, and also many unusual magnetic properties such as colossal magnetoresistance, to name a few. The electronic structure of SCESs can neither be described by assuming nearly free electrons, nor by a completely ionic model. Rather, the situation is intermediate, involving a complex set of correlated electronic and magnetic phenomena, hence the term "strongly correlated electrons". Such systems are difficult to model, because the balance between competing phenomena is easily shifted by small changes in the atomic structure, resulting in large physical effects. Therefore, the possibility of engineering new and unexpected physical properties and understanding the complexity of the underlying mechanisms represents a mushrooming field of research in modern condensed matter physics.

Transition metal oxides (TMO) form overall a very wide class of materials, which has attracted the huge attention of scientists for showing highly diversified and unusual electronic properties. Such electronic properties are typically dominated by the narrow d-bands of the TMs, where the physics is dominated by strong electronic correlations, often hybridized with O p-bands. According to the specific properties of the single materials, the "ideal" octahedra (see Fig. 1.1) in TMO are often found to be distorted, rotated, elongated, or even to

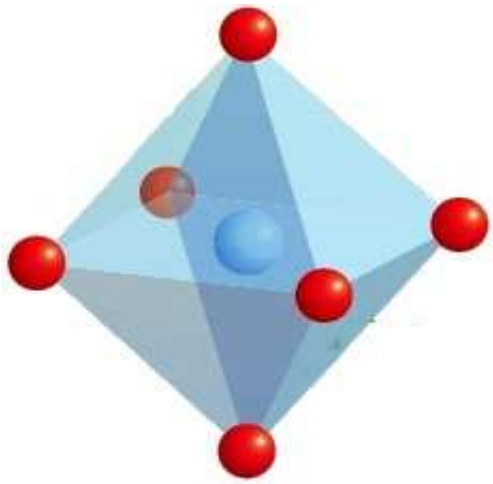

Figure 1.1: BO_6 octahedral as structural block in ABO_3 unit cell.

show unoccupied oxygen planes (as in layered materials), thus further affecting the single orbitals and the resulting bands, and eventually the overall electronic properties.

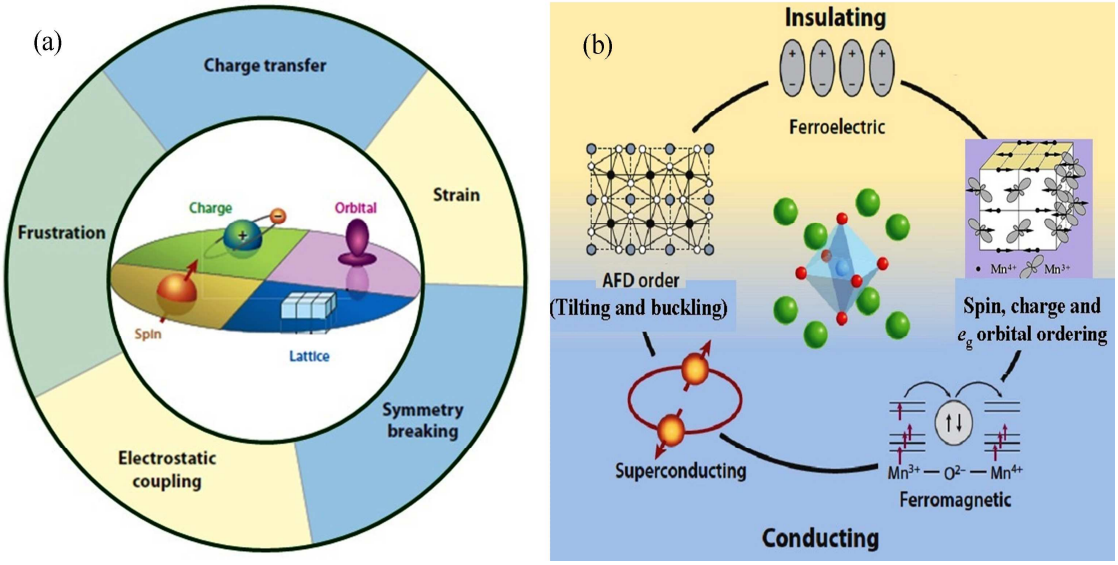

Figure 1.2: Richness in behavior of transition metal oxides (a) the complex interactions among their charge, orbital, spin, and lattice degrees of freedom, which leads to (b) a broad spectrum of functional properties. Taken from [13]

Figure 1.2a, shows the rich behavior of transition metal oxides arising from the complex interactions between their orbital, charge, spin, and lattice degrees of freedom. These interactions can be modified at interfaces between different oxides through the effects of local symmetry breaking, charge transfer, electrostatic coupling, strain, and frustration, leading to fascinating new phenomena. Figure 1.2b, illustrate the subtle interplay between competing energy scales for strongly correlated compounds which results in a variety of orderings of the spin, charge, and orbital degrees of freedom. It endows these materials with a broad spectrum of functional properties; for instance, charge transport can exhibit colossal magnetoresistance, metal-to-insulator transitions, or insulator-to-superconductor transitions. Cooperative alignment of electric dipoles or spins leads to ferroelectricity or ferromagnetism, respectively. Tilting and buckling of oxygen octahedra, which result in antiferrodistortive (AFD) structural ordering, can couple to other modes in the system, driving structural and electronic phase transitions.

1.2 Manganites: an overview

In 1950 Jonker and Van Santen [14] reported about the first crystallization and magnetic characterization of the mixed-valence "manganites", belonging to the pseudo-binary systems $LaMnO_3$-$CaMnO_3$, $LaMnO_3$-$SrMnO_3$, $LaMnO_3$-$BaMnO_3$ and $LaMnO_3$-$CdMnO_3$. The manganite system, treated for this thesis work, crystallizes in the perovskite structure whose atomic arrangements was first described in 1830s by the geologist Gustav Rose, who named it after the famous Russian mineralogist, Count Lev Alekseevich Perovskii. The manganites contain a rich variety of insulating, metallic and magnetic phases strongly coupled with transport properties and structure.

The perovskite manganites have the general formula $AMnO_3$, but most interesting for the applicative research are this $A_{1-x}A'_xMnO_3$ type of complex perovskites. The A'_x is termed as dopant specie. The insert of a dopant specie modifies some properties depending on the doping fraction x. The doped manganites have the general formula $R_{1-x}A_xMnO_3$, where R stands for a trivalent rare earth element such as La, Pr, Nd, Sm, Eu, Gd, Ho, Tb, Y etc, and *A* for a divalent alkaline earth ion such as Sr, Ca and Ba. For the stoichiometric oxide, the proportions of Mn ions in the valence states 3+ and 4+ are respectively, $1 - x$ and x.

1.2.1 The perovskite crystal structure

The ideal perovskite structure (general formula ABO_3), that crystallizes in cubic symmetry with space group Pm 3m and lattice parameter $a \approx 4$ Å, consists of a three-dimensional framework of corner-sharing BO_6 octahedra in which the A cations reside in the dodecahedral sites surrounded by twelve oxygen anions. The described structure is centrosymmetric. Only very few perovskites have this simple cubic structure at room temperature, but many of them acquire this ideal structure at higher temperatures. The manganites too have a perovskite structure of the type ABO_3 as shown in Figure 1.3.

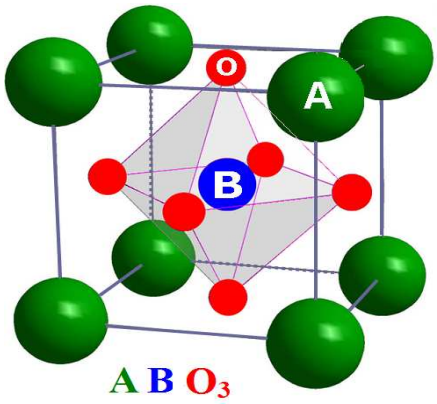

Figure 1.3: Simple cubic perovskite ABO_3.

It is worth noting that this structure can alternatively be seen as a stacking of AO and BO_2 atomic planes. Surprisingly, this perovskite (ABO_3) cubic structure can accommodate more than 30 elements on A-site, mainly alkaline metals and rare earths, and half of the periodic table on the B site, mainly transition metal elements, as shown in Fig. 1.4.

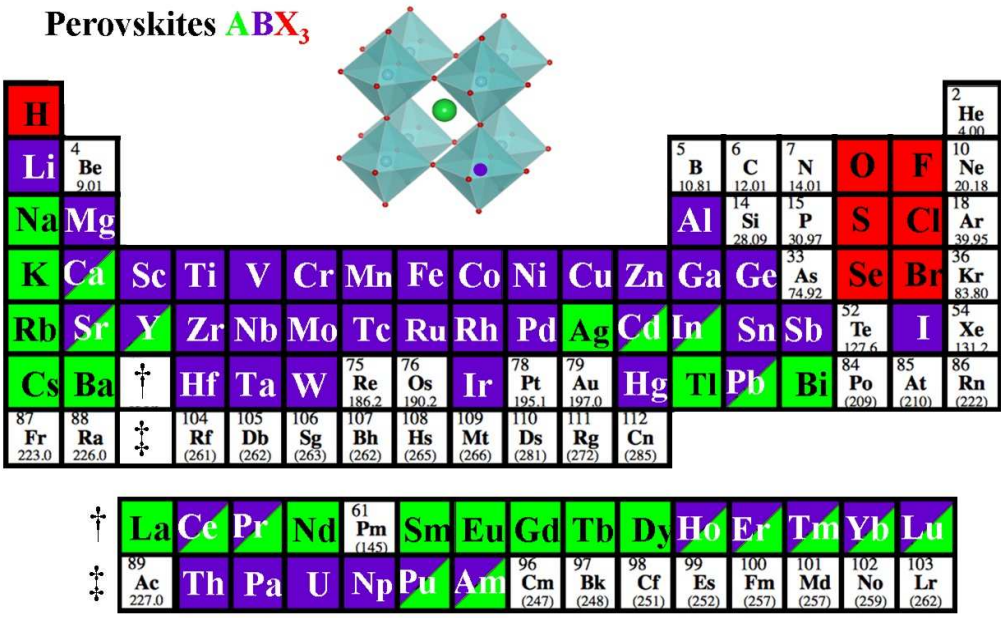

Figure 1.4: Periodic table, clearly, showing which element can occupy the sites of the perovskite structure with 100% occupancy. Taken from [15].

1.2.1.1 A-site cation size and Tolerance factor

The lattice structure of manganites is perovskite-like (i.e., nearly cubic), but rhombohedral, orthorhombic or other lattice distortions result from the tilting and stretching of oxygen octahedra around Mn ions. These distortions appear for structural (mismatch of ionic radii) and electronic (JT effect of Mn^{3+}) reasons. The Goldschmidt tolerance factor [16], which measures the deviation from perfect cubic symmetry, calculated from ionic radii in a general ABO_3 perovskite structure (Figure 1.3) is given as;

$$f = \frac{d_{A-O}}{\sqrt{2}\,d_{B-O}} = \frac{r(A)+r(O)}{\sqrt{2}\left[r(B)+r(O)\right]} \qquad (1.1)$$

with site B inside the oxygen octahedron, accounts for which elements fit into the Mn perovskite lattice and at what lattice site. *r(*A*)* and *r(*B*)* denote the average ionic radii at the A and B sites and *r(*O*)* is the radius of the O^{2-} ion. Since for an undistorted cube the B–O–B

(i.e., Mn–O–Mn) bond is straight, $f = 1$. However, sometimes the A ions are too small to fill the space in the cubic centers, and due to this the oxygen tend to move toward this center, reducing d_{A-O}. For this reason, the tolerance factor becomes smaller than one, $f < 1$, as the A-site radius is reduced, and the B–O–B angle becomes smaller than 180◦.

The stable perovskite structure (distorted structure) occurs over a range of $0.89 < f < 1.02$. For lower values of f the cubic structure is distorted to optimize the A–O bond lengths. For values of f between 0.75 and 0.9, the MnO_6 octahedra tilt cooperatively to give an enlarged orthorhombic unit cell [17]. This distortion (i.e., the reduction of Mn–O–Mn angle from 180◦) affects the conduction band, which appears as hybridization of the p level of the oxygen and the e_g levels of the Mn.

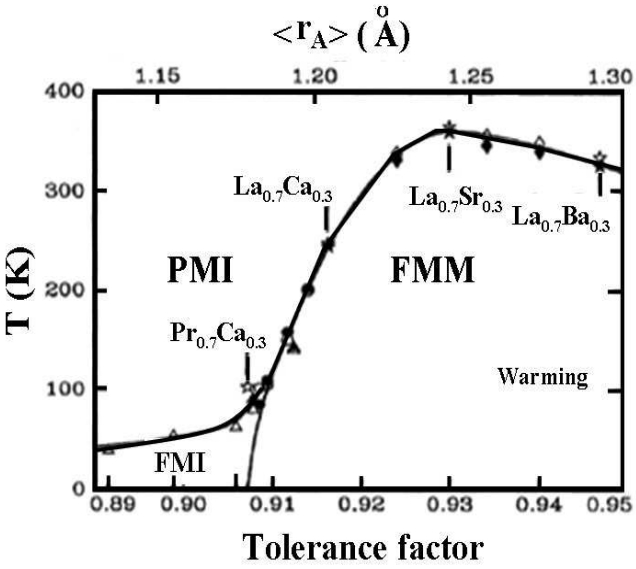

Figure 1.5: Phase diagram of temperature versus tolerance factor for the system $R_{0.7}A_{0.3}MnO_3$. Taken from [19].

The orbital overlap decreases with decrease in tolerance factor and the relation between the bandwidth W and θ has been estimated as $W \propto \cos^2 \theta$ [18]. Hwang *et al* [19] have carried out a detailed study of the structure–property correlation as a function of temperature and tolerance factor t, for the $R_{0.7}A_{0.3}MnO_3$ compound for a variety of R and A ions. The typical relationship is shown in Fig. 1.5, it shows the clear presence of three dominant regions; a paramagnetic insulator at high temperature, a low temperature ferromagnetic metal at large tolerance factor and a low temperature charge ordered ferromagnetic insulator (FMI) at small tolerance factor. The size mismatch of ions substituted into the perovskite lattice (the so-called *chemical pressure effect*) causes a reduction in the Mn–O–Mn bond angles from 180◦ down to 160◦ and below. Thus, the conduction band width (*W)* is reduced due to a smaller orbital overlap. Changes in the bond length are another consequence of the varied ionic radii, additionally influencing *W*. Most manganites have a tolerance factor $f < 1$, i.e. the ions on the La site are too small. By increasing r(A), one can observes both, increasing average bond angle (enhanced *W)* and bond length (reduced *W)* [20]. Hence, the ferromagnetic Curie temperature T_C of $R_{0.7}A_{0.3}MnO_3$ increases with r(A) but drops when the effect of the increasing bond length starts to dominate (for A = Pb, Ba).

1.2.2 Electronic configuration

Manganites have a complex electronic structure. Mn^{2+}, Mn^{3+} and Mn^{4+} valence states found in manganites have 5, 4 or 3 electrons in the 3d level, all with parallel spins according to Hund's first rule. Hund's rule coupling energy U_H is particularly large for Mn, about 2 eV [21]. For an isolated 3d manganese ion (Z = 25, electronic configuration $3d^5 4s^2$), five-fold degenerate orbital states are available to the 3d electrons (Fig. 1.6).

1.2.2.1 Crystal field and Hund's coupling

For a non isolated manganese ion, i.e., inside the MnO_6 octahedra, the hybridization and the electrostatic interaction with the oxygen p-electrons give rise to an octahedral crystal field. This, in turn, partially lifts the orbital degeneracy. As a result, the degeneracy of the d-band is partially lifted and it splits into two states: a lower-energy three fold degenerate t_{2g} (d_{xy}, d_{xz}, d_{yz}) and a higher energy two fold degenerate e_g (d_{x2-y2} , d_{z2}), with a separation 10Dq ~ 1.5 eV [22, 23], as showed in Fig. 1.6. The notation "e_g" used for higher energy state orbitals is borrowed from the irreducible representations of the O_h point group. Mn mixed valence is determined by doping (x): mathematically,

$$Mn^{3+} \rightarrow Mn^{4+}$$

$$\Rightarrow Mn^{3+}\left(3d^4, t_{2g}^{3\uparrow} e_g^{1\uparrow}, S=2, \approx 4\mu_B\right) \rightarrow Mn^{4+}\left(3d^3, t_{2g}^{3\uparrow} e_g^{0}, S=3/2, \approx 3\mu_B\right)$$

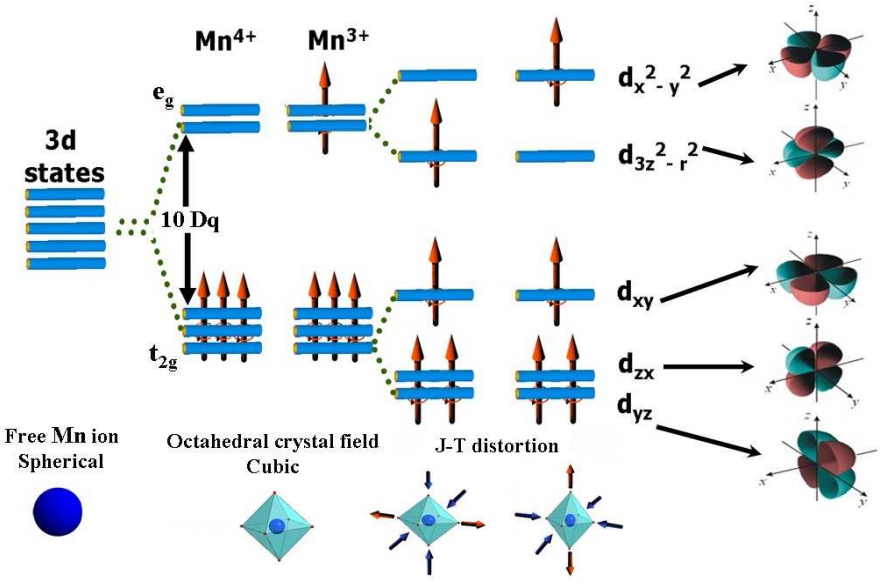

Figure 1.6: Effect of the octahedral crystal field on *d* states of a transition metal atom.

The three lower orbitals have symmetry label as t_{2g}. The e_g orbitals are oriented towards the neighbouring oxygen while the t_{2g} states have nodes in these directions. This means e_g

orbitals can overlap with oxygen *p* orbitals. The electrons aligned in the t_{2g} level form a "core spin" with total spin S=3/2. The electrons on the t_{2g} level do not contribute to the transport process because they are strongly localized around the nucleus [24]. The last *d* electron on the e_g level of Mn^{3+} is well separated in energy and aligned to the core spin via strong Hund's coupling, this e_g electron plays a vital role in transport and magnetic properties of manganites.

1.2.2.2 The Jahn-Teller effect

The orbital configuration is clearly strongly connected with the structural distortion of MnO_6 octahedra. In perovskite manganites, the degree of buckling of MnO_6 octahedra is expressed by the tolerance factor *f* (Eq. 1). There is another type of MnO_6 structural distortion taking place which is associated with the Jahn-Teller (JT) effect [25]. It is most pronounced when an odd number of electrons occupy the e_g orbital and a doubly-degenerate ground state is present. As such, Mn^{3+} is Jahn-Teller active chemical specie while Mn^{4+} is not. The Jahn-Teller theorem basically states that, the high-symmetry state with an orbital degeneracy is unstable with respect to a spontaneous decrease of symmetry, hence lifting this degeneracy [26]. Therefore a structural distortion in the form of compressed or elongated BO_6 octahedra occurs, lifting the degeneracy of e_g states. Infact when the long range orbital order exist the JT distortion is always present [27]. When the environment of a single Mn ion is taken into account, the JT effect is local. However, if the JT distortion involves the octahedra cooperatively throughout the crystal, a distortion of the whole lattice occurs, called cooperative JT effect (Fig. 1.7).

This effect occurs in manganites when the concentration of Mn^{3+} ions is sufficiently high (i.e., at low doping level). The effect of cooperative Jahn-Teller effects in manganites is to localize the e_g electrons on Mn^{3+} sites, and to stabilize insulating phases, either locally or at long range. When Mn^{3+} is diluted into Mn^{4+} species by doping, the possibility of cooperative effects among JT active octahedra is reduced, and no static distortion will be observed. In

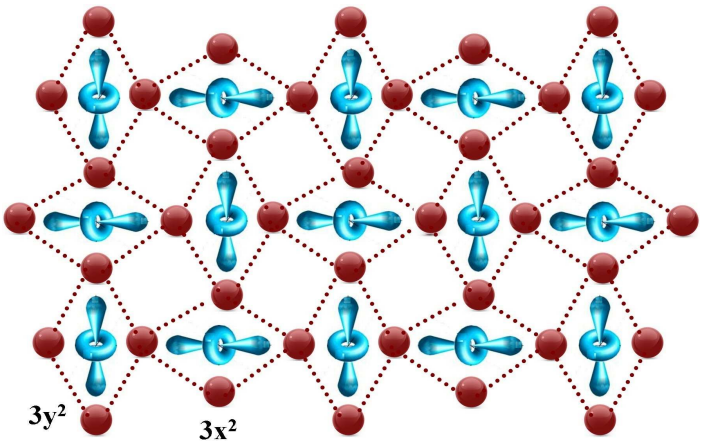

Figure 1.7: The cooperative JT distortions and resulting lattice.

opposition to the cooperative JT effect, the effects that are observed for high dilutions are called dynamic JT effects. A dynamic effect involves rapid hopping of the distortion from site to site. This is important in manganites which contain a mixture of Mn^{3+} and Mn^{4+} ions with low Mn^{3+} content.

1.3 Phenomenology of manganites

Manganites can be broadly classified into three classes, namely large, intermediate and low bandwidth manganites. This classification is on the basis of magnitude of hopping amplitude for e_g electrons. Larger the amplitude (bandwidth), more metallic the manganite should be. Large bandwidth manganites show a ferromagnetic metal (FM) phase. FM state tends to be less prominent as bandwidth is reduced. Bandwidth can also be tuned by applying pressure, changing size of the ions, etc. and so is the change in phenomenology as we will see below.

1.3.1 Colossal magnetoresistance and metal insulator transition

The colossal magnetoresistance (CMR) effect refers to the relative change in the electrical resistivity of a material and a shift in the resistivity curves versus higher temperature, on the application of an external magnetic field. The effect, observed in the manganese perovskites, was called "colossal" magnetoresistance to distinguish it from the giant magnetoresistance observed in magnetic multilayers. Actually the COI state of $Pr_{1-x}Ca_xMnO_3$ (PCMO) may collapses to a charge disordered state, which is observed as an insulator– metal transition, when an external perturbation like, magnetic field [28, 5], photon-excitation/light [8], x-rays [9], electron irradiation [29], high pressure [7], and a static electric field is applied [6]. The above type of insulator– metal transition is shown in Fig. 1.8, under pressure and magnetic fields.

In doped manganites $R_{1-x}A_xMnO_3$ the origin of the CMR is connected with the presence of a metal-insulator transition. The CMR effect is observed in manganites within a narrow window of composition x (i.e., x = 0.3 and 0.4), where the coexistence of two micrometric magnetic phases in the absence of the magnetic field exists: a ferromagnetic insulating (FMI) phase and an antiferromagnetic insulating (AMI) one. In the presence of a magnetic field, these phases transform into a ferromagnetic metallic phase at a Curie temperature T_C. In the vicinity of this T_C, the maximum CMR effect appears. The magnetoresistance is usually defined as:

$$\frac{\Delta R}{R} = \frac{R(H) - R(0)}{R(0)} \qquad (1.2)$$

where R(H) and R(0) represent the resistance in presence and in absence of the external magnetic field, respectively.

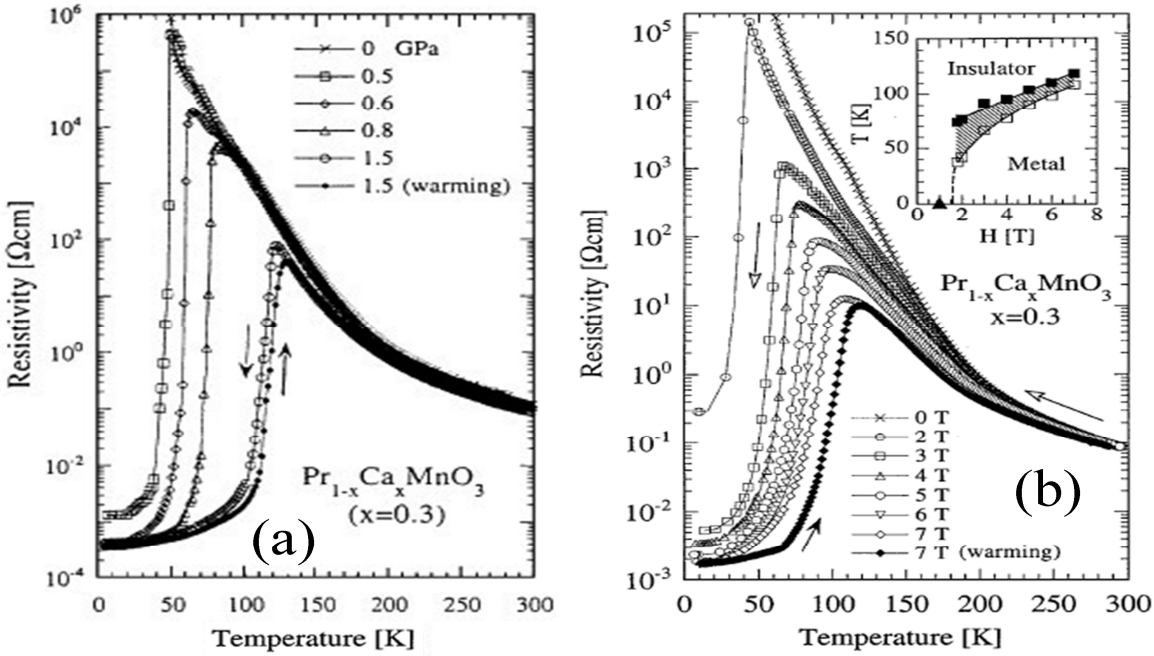

Figure 1.8: Effect of applied; (a) pressure [7] and (b) magnetic field [5] on PCMO resistivity.

As an example, Fig. 1.8b shows the Resistivity measurements versus temperature in applied magnetic field for the $Pr_{1-x}Ca_xMnO_3$**.** For manganites, the origin of the CMR is partly connected with the double exchange mechanism. In a Mn^{3+} ion, the t_{2g} electrons are tightly bound to the ion but the e_g electron is itinerant. Because of the double exchange interaction, the hopping of e_g electrons between Mn sites is only permitted if the two Mn core spins are aligned. The magnetic field aligns the core spins and, therefore, increases the conductivity, especially near T_C. The situation is actually more complicated because the carriers interact with phonons because of the Jahn-Teller effect. The strong electron-phonon coupling in these systems implies that the carriers are actually polarons above T_C. The transition to the magnetic state can be regarded as an unbinding of the trapped polarons [30]. In view of the models proposed to explain the origin of CMR effect in manganites, the percolation mechanism has got significant attraction during the last decade [31, 32]. This model is based on the idea that the CMR is due to percolation between nanoscale ferromagnetic metallic (FMM) clusters in an antiferromagnetic insulating (AFI) matrix [32].

1.3.2 Half metals and spin polarization

The manganites show large MR [33] and spin polarization effects, making them potential candidates for an arising spintronics technology [22, 34, 35]. However, it was realized that the way into technology is not as straightforward for manganites as it was, for example, for giant magnetoresistance (GMR) in metallic multilayers. GMR was discovered in 1988 [36, 37] and is currently applied in magnetic sensors including read heads of hard disc drives. On the other hand, the physics of manganites is only partially understood and, even now, new parameters and phenomena are being discovered. Half-metallic ferromagnetic materials appear as potential candidates for spintronic devices, and much work is under progress to synthesize magnetic oxides, such as $La_{0.67}Sr_{0.33}MnO_3$ (LSMO) [38, 39]. In ferromagnetic metals conduction electrons can be considered to reside in two "conduction channels", with the electron spin being either parallel (spin-up) or antiparallel (spin-down) with respect to the magnetization vector. There is no intermixing between the channels if no spin-flip scattering occurs, the conductivities of both channels just add up to the total conductivity. The electronic density of states (DOS) is split into a spin-up and a spin-down sub-band (Fig. 1.9a), with a relative shift of the spin-down band towards higher energy. The difference of the DOS in the two channels ($n\uparrow$; $n\downarrow$) at the Fermi energy (E_F) produces the *spin polarization* of conduction electrons,

$$P=(n\uparrow -n\downarrow)/(n\uparrow +n\downarrow) \qquad (1.3)$$

Note that the spin polarization of a current flowing in a material might differ from P due to different velocities of $n\uparrow$ and $n\downarrow$ electrons; this is the so-called *transport spin polarization*. Interestingly, some magnetic materials appear to have no states at E_F in one of the subbands, i.e. charge carriers have only one spin direction. They are called *half-metals*. Half-metals are particularly interesting for spintronics as a source of fully spin polarized electrons. In Fig. 1.9b, I present the two-channel model that provides a simple explanation for the best-known example of spin-polarized conduction, the GMR. In a spin valve structure (Fig. 1.9c), spin-polarized electrons travel through a non-magnetic metal interlayer separating two ferromagnetic (FM) layers.

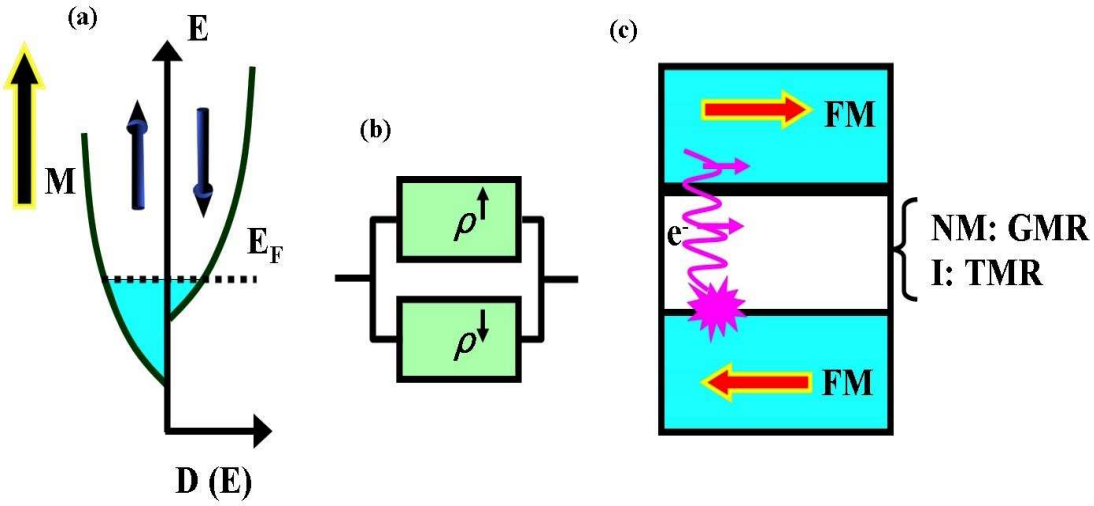

Figure 1.9: (*a*) Schematic density of electronic states (DOS) versus energy of a conducting ferromagnet. The subbands with electron spin parallel or antiparallel to the spontaneous magnetization (*M*) are split, resulting in different DOS at the Fermi level *EF*. (*b*) Two-channel model of electronic conduction, with spin up and spin down electrons in independent channels. (*c*) Trilayer junction comprising two ferromagnetic layers and a non-magnetic interlayer which is a metal in GMR junctions and an insulator in a tunnel junction. The small arrows indicate the spin of a majority electron moving through the layer stack and being strongly scattered (in case of GMR) at the interface to the electrode magnetized oppositely. Taken from [40].

Essentially, spin dependent scattering occurs only at the interfaces. For parallel magnetization directions of both FM layers, spin-up electrons can pass with little scattering at both interfaces; thus, resistance of the layer stack is lower than that for antiparallel magnetization directions. If the interlayer is replaced by an insulator with the thickness of a few nanometres, a magnetic tunnel junction is obtained, which is the other spintronics device that has already achieved commercial relevance (as magnetic random access memory, MRAM). Very recently R. Werner et al. reported [41], the largest TMR in manganite tunnel junction (i.e., $La_{0.65}Sr_{0.35}MnO_3$ / $SrTiO_3$ / $La_{0.65}Sr_{0.35}MnO_3$) grown by molecular-beam epitaxy, showing a large field window of extremely high tunneling magnetoresistance (TMR) at low temperature. The TMR reaches ~1900% at 4 K, corresponding to an interfacial spin polarization of~95% assuming identical interfaces. In the case of a half-metal, tunnelling is forbidden for antiparallel orientation of the magnetization vectors of FM layers. Alignment of magnetization by a modest magnetic field produces a huge resistance drop or *tunnelling MR* (TMR). There are several devices exploiting spin polarization of charge carriers and a magnetic field for the control of electrical resistance or current, which include the spin valve transistor [42], the magnetic tunnel transistor [43] and spin injection devices [44] to name a few.

1.3.3 Orbital and charge ordering

The orbital ordering consists in a spatially ordered arrangement of d orbitals in the crystal. Strongly associated with the carrier concentration, it develops when the d electrons occupy an asymmetric orbital. The direct electrostatic repulsion of the charge clouds, coupled with cooperative JT distortions, stabilises the effect generating an ordered sublattice of orbitals. A scheme of OO is shown in Fig. 1.10a and b.

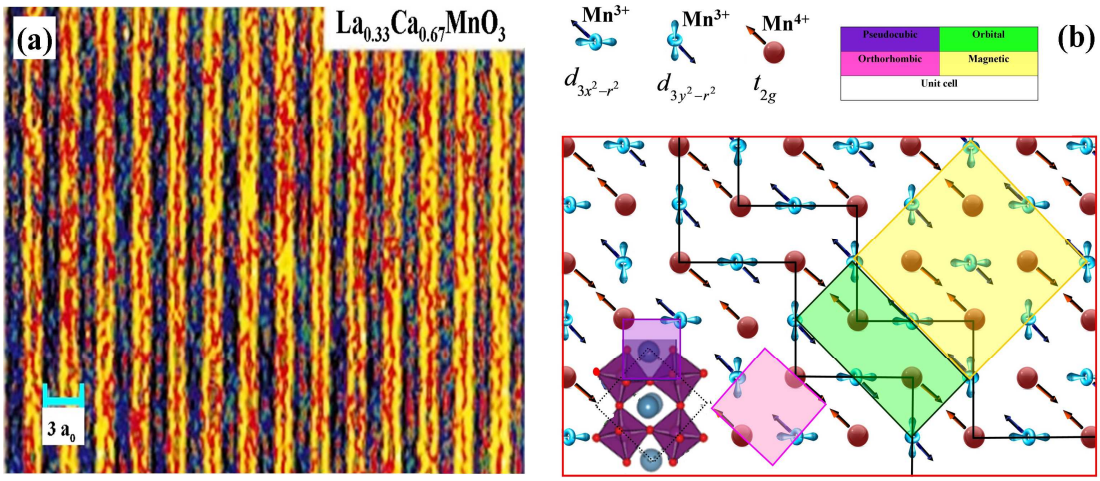

Figure 1.10: (a) Pairing of charge-ordered stripes in $La_{0.33}Ca_{0.67}MnO_3$, high-resolution lattice image obtained at 95 K showing $3a_0$ pairing of Jahn–Teller distorted diagonal $Mn^{3+}O_6$ stripes (JTS); (b) The CE-type magnetic structure present in x=0.5 PCMO at low temperatures (charge, orbital and spin order is also visible).

Indeed the ratio Mn^{3+}/Mn^{4+} is responsible for the phenomenon of charge ordering (CO). This consists of a periodic distribution of electric charge (i.e. e_g electrons of Mn^{3+} ions in the crystal lattice), driven by Coulomb interaction. The mobile e_g electrons may become localized at certain Mn ion positions in the lattice, forming an ordered sublattice. In principle, however, these charges do not need to be necessarily localized on the Mn sites, and in fact they could sit on the bond centres as well, or, in the most general case, on some intermediate point between those two. Such an intermediate CO state can be more generally seen as a charge-density wave, lacking inversion symmetry and then potentially capable to develop ferroelectric ordering. In the COI phase of the bulk $Pr_{0.5}Ca_{0.5}MnO_3$ (T_{CO} = 250 K and T_N =170 K) apart from the check-board like site-centred arrangement of Mn^{4+} and Mn^{3+} ions, there is also an orbital and CE-type magnetic arrangement present (Fig. 1.10b). In the ab-plane the ferromagnetic zigzag lines are antiferromagnetically coupled and the coupling is AF also in the c-direction. Along the zigzag lines the charged sequence

$Mn^{3+} - Mn^{4+} - Mn^{3+} - Mn^{4+}$ is followed by orbital ordering sequence $e_g\left(3x^2 - r^2\right) - t_{2g}^3 - e_g\left(3y^2 - r^2\right) - t_{2g}^3$. For the lower values of $x < 0.5$ a bond-centred model is proposed [45, 46]. In this view metal sites remain valence equivalent and the charge is located in the bond forming so called magnetic Zener polaron - a ferromagnetically linked JT distorted octahedra with enhanced double exchange. Moreover, according to reference [45], the coexistence of site and bond-centred mechanism leads to *ferroelectricity* opening the possible path to multiferroic behavior.

1.4 Magnetic/Exchange interactions

1.4.1 Direct exchange

The phenomenon of long range magnetic order contains exchange interactions at its heart. Although the consequences of the exchange interaction are magnetic in nature, yet the cause is not. Exchange interactions, being due primarily to electrostatic interactions, arising because charges of the same sign cost energy when they are close together and save energy when they are apart. Indeed, in general, the direct magnetic interaction between a pair of electrons is negligibly small compared to this electric interaction. If the electrons on nearest neighbour magnetic atoms interact via exchange interaction, this is known as direct exchange. The direct exchange is modelled by the Heisenberg exchange Hamiltonian:

$$H_{ex} = -\sum_{ij} J_{ij} S_i \bullet S_j \qquad (1.4)$$

Here J_{ij} is the exchange constant between the i^{th} and j^{th} spins, distributed on a regular lattice. Usually, the summation includes only nearest neighbours. The magnetic properties of the crystal depend on the sign and the strength of the interaction between spins: if $J_{ij} = J > 0$ the parallel orientation of the spins is favoured, giving a ferromagnetic state. If $J_{ij} = J < 0$, the magnetic order is antiferromagnetic, with the spins of nearest neighbours antiparallel. However for the manganites, as in many other magnetic materials, it is necessary to consider some kind of indirect exchange interaction, because the Mn ions are alternated with O in the lattice.

1.4.2 Indirect exchange: superexchange

Superexchange is an indirect exchange interaction between non-neighbouring magnetic ions mediated by a non-magnetic ion that is placed in between them. This interaction was first proposed by Kramers [47] in 1934. The main aim behind his work was to find an

explanation for the magnetic properties observed in insulating transition metal oxides, in which the magnetic ions are so distant that a direct exchange interaction could not explain the presence of magnetically ordered states, so the longer-range interaction that is operating in this case should be "super". The problem was thereafter treated theoretically by Anderson [48], who in 1950 gave the first quantitative formulation showing that the superexchange favours antiferromagnetic order.

1.4.3 Double exchange

In a few oxides, it is possible to have a ferromagnetic exchange interaction which occurs because the magnetic ion shows mixed valency. The "double exchange" (DE) mechanism proposed by Zener [49], is a theory that predicts the relative ease with which an electron may be exchanged between two species. The ferromagnetic coupling between Mn^{3+} and Mn^{4+} ions, participating in electron transfer, is due to the double exchange mechanism. The DE process was explained historically in two ways. In the first way, there are two simultaneous motions of electrons involving up spin electron moving from oxygen to the Mn^{4+} ion and up spin electron moving from Mn^{3+} ion to the oxygen as shown by arrows in the Fig. 1.11, and can be schematically (mathematically) written as,

$$Mn_{1\uparrow}^{3+}\, O_{2\uparrow,3\downarrow}\, Mn^{4+} \Rightarrow Mn^{4+} O_{1\uparrow,3\downarrow} Mn_{2\uparrow}^{3+},$$

where 1, 2, and 3 label electrons that belong either to the oxygen between manganese, or to the e_g level of the Mn-ions. In this process there are two *simultaneous* motions (thus the name double exchange) involving electron 2 moving from the oxygen to the right Mn-ion, and electron 1 from the left Mn-ion to the oxygen (see Fig. 1.11). The second way to visualize DE was involving a second order process in which the two states described above go from one to the other using an intermediate state $Mn_{1\uparrow}^{3+} O_{3\downarrow} Mn_{2\uparrow}^{3+}$ [50]. Briefly, the e_g electron on a Mn^{3+} ion can hop to a neighbouring site only if there is a vacancy of the same spin (since hopping proceeds without

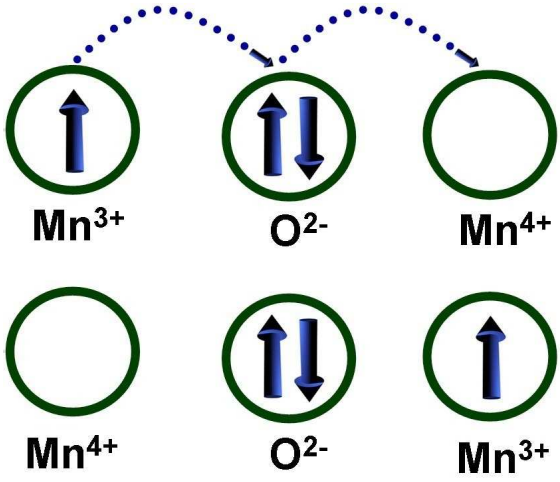

Figure 1.11: Sketch of the double exchange mechanism which involves two Mn ions and one O ion. The mobility of e_g electrons improves if the localized spins are polarized. Taken from [22]

spin-flip of the hopping electron). If the neighbour is a Mn^{4+} ion which has no electron in its e_g shell, this should present no problem.

However there is a strong exchange interaction (first Hund's rule) between the e_g electron and the three electrons in the t_{2g} level that want to keep them all aligned. This is not favourable for an e_g electron to hop to a neighbouring ion in which the t_{2g} spins will be antiparallel to the e_g electron (Fig. 1.12b). Furthermore, ferromagnetic alignment of neighbouring ions is therefore required to maintain the high spin arrangement on both the donating and receiving ion. Because the ability to hop gives a kinetic energy saving, allowing the hopping process reduces the overall energy. Thus, the ions align ferromagnetically to save energy. Moreover, the ferromagnetic alignment allows the e_g electrons to hop through the crystal and the material became metallic. It has been shown [50], that the electron transfer integral t between Mn ions in the double exchange process depends on the angle θ between their two core spins: $t = t_o \cos(\theta/2)$.

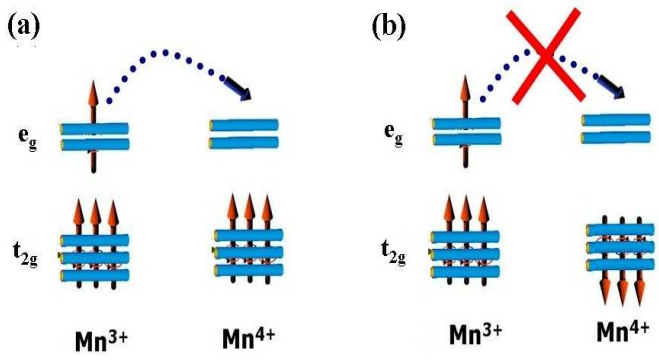

Figure 1.12: The double exchange interaction favours hopping if (a) neighbouring ions are ferromagnetically aligned, and not if (b) neighbouring ions are antiferromagnetically aligned.

1.5 $Pr_{1-x}Ca_xMnO_3$ compound

The narrow band manganites host a rich variety of phases characterized by different structure, magnetic ordering and transport properties. The applied fields [51], including magnetic, electric, stress, etc. may affect in a dramatic way the physical properties, as in the celebrated colossal magnetoresistance or electroresistive effects, or giant magnetostriction, etc.

1.5.1 Structure

The undoped $PrMnO_3$ has an orthorhombic distorted structure at room temperature that belongs to the P_{bnm} space group as shown in Fig. 1.13. To obtain $Pr_{1-x}Ca_xMnO_3$ (PCMO) from $PrMnO_3$ divalent Ca^{2+} is substituted with trivalent Pr^{3+} ions by chemical doping.

Here, the buckling of MnO_6 octahedra plays a significant role and the Mn-O-Mn angles deviate largely from the ideal 180°, lowering the role of double exchange mechanism. For undoped PMO, Mn-O-Mn angles are 155° and 165° for the apex and equatorial O, respectively.

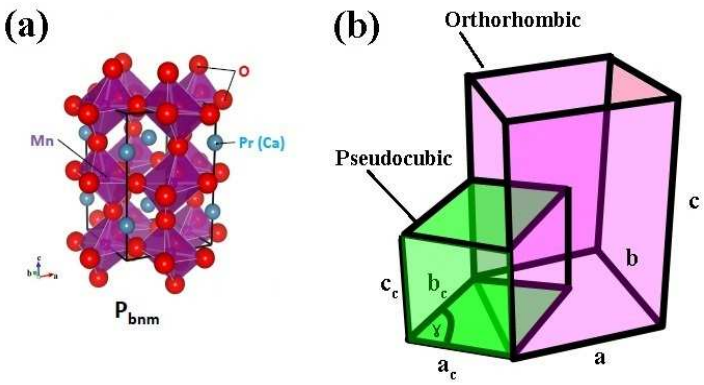

Figure 1.13: (a) PCMO structure; (b) Correspondence between orthorhombic and pseudo-cubic unit cell parameters.

1.5.2 Phase diagram

The phase diagram of PCMO is shown in Fig. 1.14. PCMO deserves a special attention, as it is in fact the only hole-doped manganite with insulating character throughout the whole x = [0,1] range. This is a consequence of the small ionic radius of Ca, which results in a pronounced orthorhombic distortion (see also Fig. 1.13) that favours charge localization.

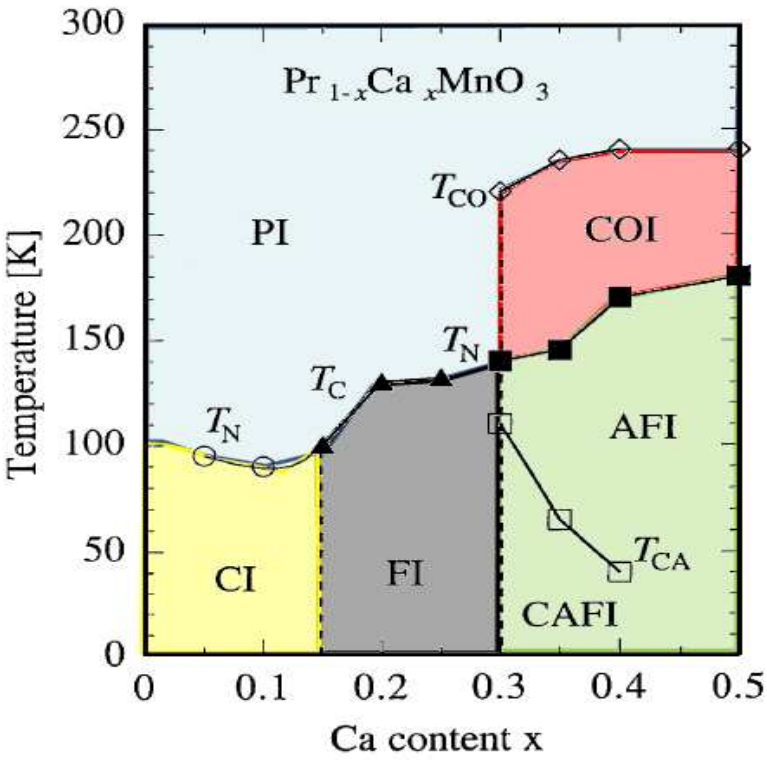

Figure 1.14: Phase diagram of $Pr_{1-x}Ca_xMnO_3$. After reference [17]. The canted AF insulating (CAFI) state also shows up below the AFI state in the COI phase $0.3 < x < 0.4$. A paramagnetic insulator (PI) phase is present at high temperatures.

At high temperature a paramagnetic insulating (PI) is present, while for low doping $x < 0.15$, a spin canted insulating (CI) phase exists. . For 0.3<x<0.5, PCMO exhibits antiferromagnetic insulating (AFI) behavior at lower temperature (T≤ 175 K). There is also a canted antiferromagnetic insulating (CAFI) region present for 0.3<x<0.4 at further low temperatures (T<100K). In the range of $0.15 < x < 0.30$ a ferromagnetic insulator (FI) state is present at lower temperatures. The nature of the FI phase present at low doping levels in the phase diagrams of several manganites is object of intensive theoretical and experimental investigations [52]. At present, there is still debate on the interpretation of the phenomenology and on the comprehension of the microscopic interactions that determine such FI state. Very general issues are its extension in the phase diagram and the origin of its competition with the ferromagnetic metallic (FM), charge (and/or orbital) ordered insulating (respectively, COI and OO), and with the antiferromagnetic insulating (AFI) phases. While the physical mechanism (i.e., the double exchange interaction) that leads to the FM state in manganites is well known [22, 53], the reason why an insulating state can persist in a ferromagnet is less evident. At low temperature (T≤ 240 K), for broad range of doping $0.3 \leq x \leq 0.75$, PCMO shows a Jahn–Teller distortion that causes a charge ordered insulating (COI) state at T_{CO} [54]. Moreover, in this compound at half doping (x=0.5), a COI is present, while intermediate and large bandwidth manganites exhibits a ferromagnetic-metallic behavior at this doping concentration. This COI state in PCMO may collapse to a charge disordered state, which is observed as an insulator– metal transition, when an external perturbation is applied

1.6 $Pr_{0.7}Ca_{0.3}MnO_3$ system

The present work focuses on the investigation of $Pr_{1-x}Ca_xMnO_3$ (PCMO) with $x = 0.3$. This compound represents, in our view, an outstanding example of the complexity of high correlated manganites. This system never shows a metallic state in the whole phase diagram, at difference to the better known LSMO. Further details about PCMO will be shown in chapter-3 together with experimental data. This concludes the phenomenology part on manganites. Now I would like to move onto next section which is related to two-dimensional electron gas at the interface between TMOs.

1.7 Two-dimensional electron gases

A gas of electrons free to move in two dimensions, but tightly confined in the third is termed as two-dimensional electron gas (2DEG). The most commonly encountered 2DEG is the layer of electrons found in MOSFETs. When the transistor is in inversion mode, the electrons underneath the gate oxide are confined to the semiconductor-oxide interface, and thus occupy well defined energy levels. In the ideal case only the lowest level ($k_z = 0$) is occupied, and so the motion of the electrons perpendicular to the interface can be ignored. However, the electron is free to move parallel to the interface, and so is quasi two-dimensional. A careful choice of the materials and alloy compositions allow control of the carrier densities within the 2DEG.

1.8 Building blocks of the heterostructure

1.8.1 $SrTiO_3$

The mineral responsible for the name of perovskite crystal structure is $CaTiO_3$, however, all the fame of these oxides is received by another titanium compound: strontium titanate $SrTiO_3$ (here after STO). At room temperature STO has cubic perovskite structure with unit cell dimensions equal to 3.905Å and Pm3m as crystallographic space group. One reason for its large scientific interest is that STO plays an important role as a standard substrate for many oxide materials. For example, it is possible to grow high-T_c superconductors [55], colossal magnetoresistance oxides or ferroelectrics epitaxially on STO due to high thermal stability, and structural as well as lattice compatibility. Moreover, STO is chemically inert. In many cases it does not react with the deposited materials. This success has been pushed further by the ability to chemically process its (001) surface to obtain a 100% TiO_2 termination. Technological applications of STO require the optimization of the processes that can reproducibly produce a given surface. However, polishing and etching of STO as a substrate lead to several kinds of defects on the surface and cannot be successfully used as a proper substrate for thin film growth. Obtaining of TiO2-terminated STO (001) with ultra-flat and molecularly layered steps by chemical etching in an NH_4F–HF buffer solution in combination with thermal treatment [56, 57] is already established as common way for the surface preparation. Stoichiometric STO has a relatively large indirect band gap of 3.25 eV and exceptional dielectric properties. The dielectric constant increases with decreasing temperature. Values from several hundred at 300K to up to 25000 at 4K in bulk samples [58, 59], and up to 4000 in thin films [60, 61] have been reported. At low

temperatures a strong reduction of the dielectric constant is found upon application of electric fields [62]. STO is chemically a very stable material up to the melting point of 2353 K, but during cooling down its cubic structure transforms to tetragonal at 105 K. Moreover, recently, J. Xing et al. [63] reported that STO single crystal is an attractive candidate for a UV detector.

1.8.2 $LaAlO_3$

Another building block of the studied heterostructures is $LaAlO_3$ (here after LAO), which has a good lattice matching with many oxide materials just like STO. Because of this property it was also thoroughly studied as substrate material [64]. In this thesis work LAO is not considered as a substrate but instead was used only as thin film on STO substrates. At high temperatures LAO has the cubic perovskite structure (space group Pm3m). At ~ 813K it undergoes a transition to a rhombohedral distorted perovskite structure [65]. Here LAO is always in the low temperature range, where the structure differs from the cubic perovskite only by small antiphase rotations of AlO_6 octahedra. It can be described as pseudocubic with a lattice constant of 3.791Å [66]. The reasonably small lattice mismatch of 3% to STO and the similarity of the thermal expansion coefficients [67, 68] allow the epitaxial growth of LAO films on STO. Optically, LAO single crystals are yellowish transparent. LAO is a band insulator with a wide gap of 5.6 eV. Like STO it belongs to the high-k oxides, having a dielectric constant of about 25 for temperatures between 300K and 4K [64, 69].

1.9 Polar/non-polar surfaces

The search for novel oxide heterostructures supporting the formation of a two dimensional electron gas (2DEG) at the interface between two robust band insulators is of major interest both for fundamental and applied physics. The availability of multiple kinds of such structures increases, on the one hand, the degrees of freedom in trying to address the physical mechanisms and the material issues underlying 2DEG formation. It possibly opens the route, on the other hand, to optimizing device properties by adopting suitable materials in view of specific applications. A classical electrostatic criterion says that, the stability of a compound surface depends on the characteristics of the charge distribution in the structural unit which repeats itself in the direction perpendicular to the surface. The mechanism of charge redistribution is strongly linked with the surface type. P. W. Tasker established a classification of surface types using basic electrostatic principles [70]. His classification is shown schematically in Fig.1.15.

In the type I surface the charge in each plane is spread in a way that these planes are charged neutrally. If planes are arranged with repeating units and are charged, but without dipole moment, the surface is called type II. Finally, type III surface is characterized in such a way that each layer parallel to the surface has a charge σ and the dipole moment. To which type a surface belongs depend mostly on: the surface orientation **n**, the characteristics of the polarization in the bulk unit cell, and on the crystal termination. Bulk electric polarization **(P)** of insulating crystals is defined by the centers of charge of the Wannier functions of the occupied bands. If the surface orientation is **n**, the bound charge density on the surface (σ_b), is described with equation σ_b = **P** · **n**. The polarization as vector has modulo as q/A, where A is the surface cell area. If condition that modulo q/A is equal to zero (σ_b = 0) is satisfied, the surface is nonpolar [71]. For most cases, simple models for the electronic structure can easily indicate when a surface is polar or not. Hence, it is necessary just to use the sign of the ions charge in the plane. For example, $SrTiO_3$ (110) contain SrTiO and O_2 layers as repeated units which are charged. If formal charges are assigned to the ions as: Sr^{2+}, Ti^{4+}, and O^{2-} the SrTiO has charge +4e and O^2 has -4e per unit cells in the plane. In general, polar surfaces have low stability. Let us briefly describe the origin of this instability. A very simple presentation of the crystalline compound cut along a polar direction is presented by Claudine Noguera [72].

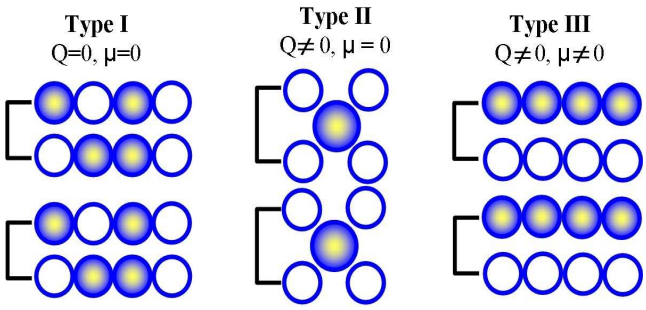

Figure 1.15: The surface types according to Tasker classification. Here Q represents charge and μ the dipole moment.

Fig.1.16a presents schematically inequivalent layers with equal but opposite charge densities ($\pm\sigma$), with interlayer spacing R_1 and R_2. The unit cell has a dipole moment density equal to $\mu = \sigma R_1$. With increasing number of the layers, the electrostatic potential increases monotonically across the system by an amount $\delta V = 4\pi\sigma R_1$ per double layer as shown in Fig. 1.16b. A potential, δV, is actually large, and could be of the order of several tens of eV in a pure ionic

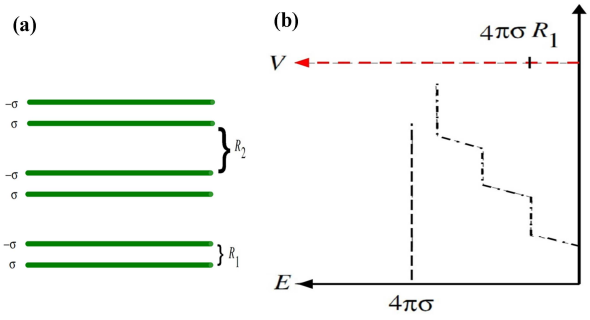

Figure 1.16: (a) Structured material with inequivalent charge layers, (b) Energy and potential dependences of the number of layers.

material like MgO [73] or a partially ionic material like LAO. The total dipole moment $M = N\,\sigma\,R_1$ of N bilayers is proportional to the thickness of the crystal, and the electrostatic energy amounts to $E = 2\pi N R_1 \sigma^2$. By increase in thickness ($N \to \infty$), the electrostatic contribution to the surface energy per unit area diverges and surface cannot exist and will collapse. However, several possibilities that would cancel the polarity and stabilize the surface are likely. One possibility is that one or several surface layers change chemical compositions respect to the bulk. This effect can be followed by reconstruction depending on order of the vacancies or adatoms which could be created. The second is connected with the environment where adsorbed atoms or ions may provide the charge compensation. Third situation for charge compensation can be due to the electron redistribution which can cancel out the macroscopic component of the dipole moment in response to the polar electrostatic field. However, this scenario can happen only on stoichiometric surfaces and graphically this effect is presented in Fig. 1.17. If the value ($\sigma' = \sigma R_2 / (R_1 + R_2)$) of the charge density is transferred on the external layers of the crystal this results that a total dipole moment is not any more proportional to the thickness of crystal ($M = \sigma R_1 R_2 / (R_1 + R_2)$.

Increasing of the electrostatic potential is also suppressed and, moreover, it saturates. Which process for stabilization of the surface will take place depends strongly on energetic considerations. However, the resulting surface energy, considering the process of depolarization, has to be as low as possible.

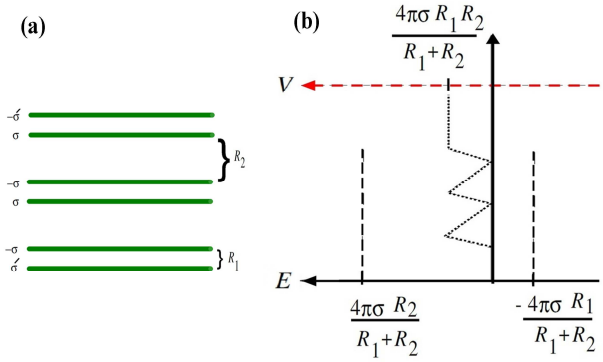

Figure 1.17: (a) Structured material with inequivalent charged layers, (b) Energy and potential dependencies of the number of layers with charge redistribution.

1.10 The case of $LaAlO_3/SrTiO_3$ heterointerface

1.10.1 Phenomenology

In 2004 A. Ohtomo and H.Y. Hwang [1] from Bell Labs (USA) reported that the interface between LAO and STO in the (001) direction can be conducting, depending on the actual chemical composition of the interface. Two different stackings were prepared by Pulsed Laser Deposition (PLD) on (001) oriented STO substrates. An illustrative sketch of both configurations is shown in Fig. 1.18. In the first configuration, LAO is grown epitaxially

on a (001) oriented STO substrate, terminated by a TiO_2 layer. For the second configuration an additional monolayer of SrO is inserted before growing the LAO. These procedures result in a TiO_2/LaO and a SrO/AlO_2 stacking, respectively, at the interface.

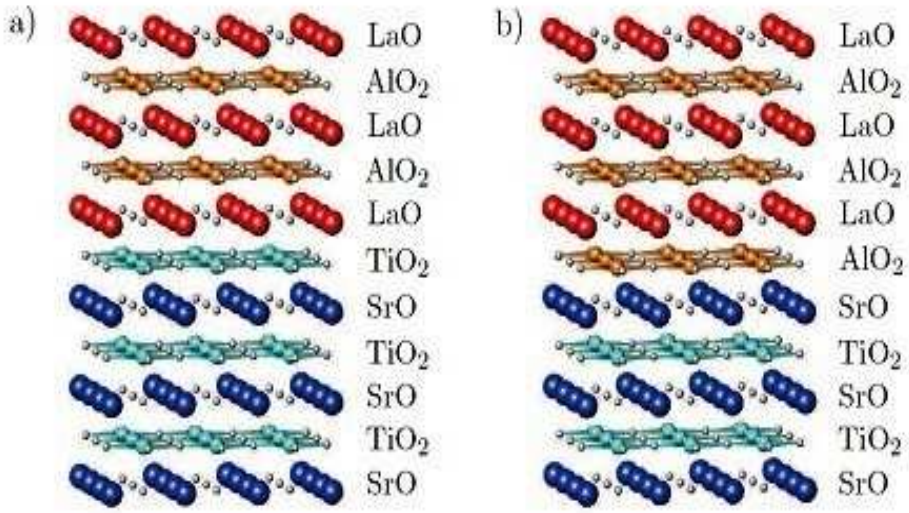

Figure 1.18: Illustration of the two possible stackings for atomically abrupt interfaces between LAO and STO in the (001) orientation. (a) n-type interface (TiO_2/LaO stacking) and (b) p-type interface (SrO/AlO_2 stacking)

The surprising result of electronic transport measurements of these samples was that one configuration (TiO_2/LaO stacking) was highly conducting at the interface, while the other configuration (SrO/AlO_2 stacking) was found to be insulating. This is definitely worth a deeper investigation for two reasons. Firstly, one stacking sequence results in a well conducting interface, although the sample is entirely composed of band insulators. Secondly, depending on the stacking sequence at the interface, the electronic properties of the heterostructure differ from conducting to insulating. It is remarkable that the insertion of one atomic layer of SrO during sample growth leads to such a tremendous difference.

1.10.2 Polar catastrophe theory

The so-called “polar catastrophe,” a sudden electronic reconstruction taking place to compensate for the interfacial ionic polar discontinuity, is currently considered as a likely factor to explain the surprising conductivity of the interface between the insulators LAO and STO. The LAO/STO heterointerface is special as here charge neutral layers and charged layers adjoin. From Fig. 1.19, clearly, this is an unfavorable situation because polarity is unfavorable.

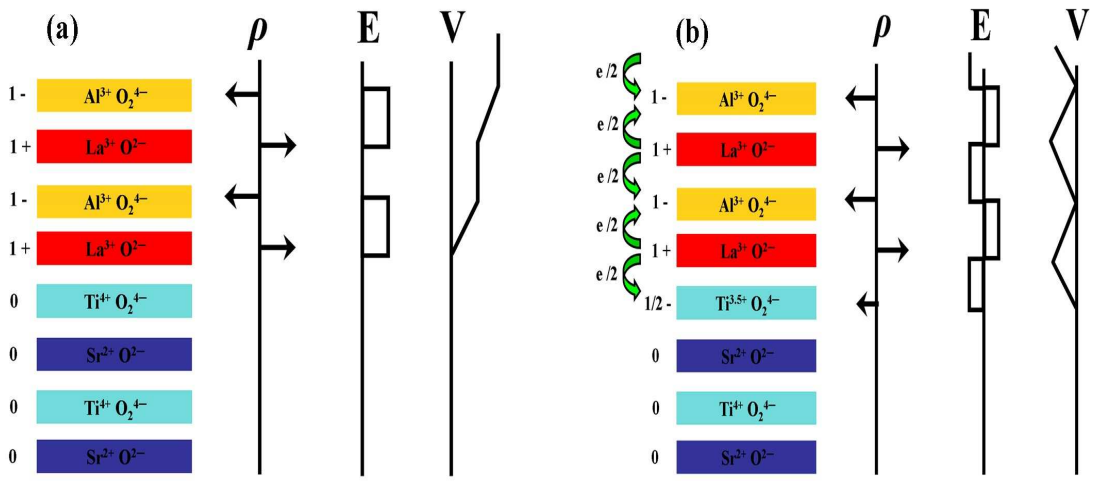

Figure 1.19: Illustration of the polar catastrophe occurring between LAO and STO. Here ρ is the net charge of the layers, which leads to the electric field E, that produces the electric potential V. (a) the unconstructed n-type interface (TiO_2/LaO stacking) leads to a diverging potential V due to the polarity discontinuity (b) if electrons are redistributed such that half an electron enters into the last TiO_2 plane the potential stays finite. Taken from [74].

The consequences of such sequencing were first discussed by G. A. Baraff et al. [75] and W. A. Harrison et al. [76] in the 1980s for semiconductor Ge/GaAs heterojunctions. Consider first the heterostructure with a TiO_2/LaO stacking sequence at the interface as shown in Fig. 1.19a. The charged sublayers produce an electric field E, which leads to an electric potential V that diverges with the thickness of the LAO film. For semiconductor heterostructures with charge neutral sheets followed by charged sheets it was shown that the system can avoid this so called polar catastrophe by redistributing the atoms at the interface, which causes roughening of the interface. An analogous argumentation explains why crystals with polar planes need to have atomic reconstructions at their surface. Conventional semiconductor ions have a fixed valence, so a spatial redistribution of ions, which leads to a roughening of the interface, is their only option to avoid the divergence of the electrostatic potential. But the complex oxides, like LAO and STO, have an additional option. The mixed valence states available allow for charge compensation by moving electrons, which happens if it is energetically favorable compared to a redistribution of ions. The effect of rearranging the electron distribution is shown in Fig. 1.19b. Briefly, one can construct the system from neutral atoms and then transfer half an electron from the LaO layers to those above and below. During this reconstruction the total structure remains charge neutral with Ti at the interface becomes $Ti^{3.5+}$. This redistribution eliminates the divergence of the electrostatic potential V. The resulting V oscillates around a finite value. In other words some insight into the possible sheet charge densities at a LAO/STO interface can be seen from the following considerations, which relate to an intrinsic doping mechanism. Since $SrTiO_3$ consists of

charge neutral SrO and TiO_2 layers, whereas the AlO_2^- and interface charge equal to half that of the last plane, if no other reconstructions take place. Indeed a neutralizing charge at the interface is required to avoid a polarization catastrophe that arises due to this net interface charge. If left uncompensated, the energy associated with this polarization grows indefinitely as the thickness of the LAO layer increases. Therefore, electrons have to be promoted to the conduction band of LAO at some point. The charge that is necessary to prevent this polarization catastrophe is equal to half an electron per unit cell, or $3.2\times10^{14}\,cm^{-2}$. Note that this estimate applies only for perfectly stoichiometric LAO and in this sense is an approximate upper limit in the intrinsic case; any defect may reduce this number or increase. In any event, clearly this line of reasoning cannot explain the very large charge densities observed. Indeed, this simple model provides a good explanation on how electronic reconstructions can lead to a metallic interface in the LAO/STO heterostructure. However it seems to be oversimplified, as, e.g., the insulating behavior of the p-type interface observed experimentally is not captured in this approach. Therefore, more sophisticated models and calculations are needed. To add few more words, during the past few years interfaces between different, in some cases even correlated systems have been theoretically studied, e.g. $LaTiO_3/SrTiO_3$ (LTO/STO) heterostructures [77, 78]. Materials that are governed by correlations offer of course a large potential for fundamental physics, due to their susceptibility to all kinds of perturbations. At the LAO/STO interface, the stacking of LaO on top of TiO_2 equals a unit cell of LTO, which is a correlated material. The presence of one unit cell of LTO at the interface might bring correlation effects into the transport properties of LAO/STO heterostructures. Finally in the bilayer configuration, however, as it is shown by Thiel at al. [79], there exists a critical thickness of $\geq$ 4 u.c. of LAO grown on TiO_2 terminated STO above which the 2D electron gas appears.

1.10.3 Extrinsic doping

Although the polar catastrophe scenario remains the main paradigm of interpretation of the properties of the LAO/STO system, yet, it is contradicted by some experimental and theoretical results. Other competing models have been proposed, based on the ease of extrinsic doping in STO. Infact, STO can be readily doped by either oxygen vacancies or rare earth substitution, both of which are possible (or even likely) at the LAO/STO interface.

It is important to note here that electronic reconstruction mechanism is not the only one contributing to novel properties of the interface, and that the deposition conditions, namely oxygen partial pressure during deposition plays an important role in determining the final state of the interface was shown by Brinkman [80].

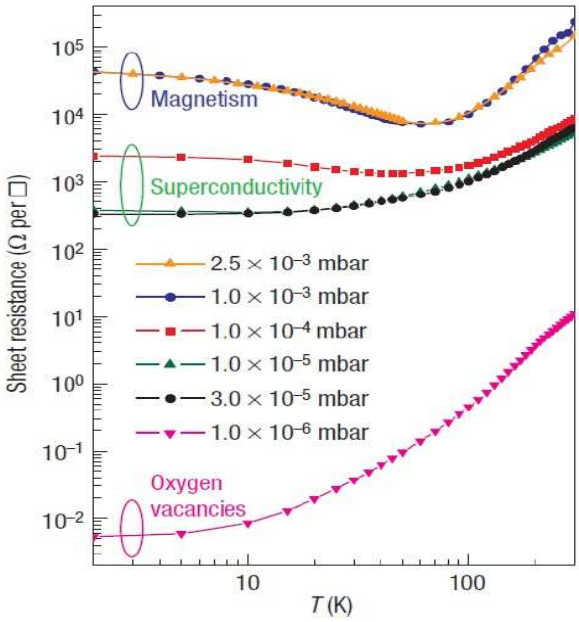

Figure 1.20: The role of the oxygen pressure used during the deposition on the final state of LAO/STO:TiO_2 (001) interface. Reproduced from [80]

The deposition oxygen partial pressure is strongly connected to the concentration of oxygen vacancies in STO, thus influencing electronic properties of the substrate and the grown system. According to ref. [80] there exist three regions, in view of the value of deposition oxygen pressure that leads to different electronic and magnetic properties for LAO/STO interface (Fig. 1.20):

- for the low deposition pressures when $P_{O_2} \leq 10^{-6}\, mbar$ the high conductivity is measured [1];
- for intermediate pressures $10^{-5}\, mbar \leq P_{O_2} \leq 10^{-4}\, mbar$ the superconductivity emerges [81, 82];
- for intermediate pressures $P_{O_2} \geq 10^{-3}\, mbar$ the insulating and magnetic behavior appears [80].

This data show that oxygen vacancies can not be ruled out when addressing the electronic properties of the interface, but they also do confirm the role of electronic reconstruction since the conducting state is always present, even at high oxygen partial pressure.

1.10.3.1 Oxygen vacancies

The high sheet conductivities and carrier densities can also be explained by an extrinsic doping mechanism, i.e. the charge carriers are generated in the synthesis process itself. The carrier densities reported in the first work [1] can not be explained by an electronic reconstruction. According to A. Kalabukhov et al. [83], one likely cause of charge carriers are oxygen vacancies in the STO substrate. Because of the relative stability of the +3 valence

state of the Ti ion, STO has a large oxygen ionic mobility and is stable even if the quantity of oxygen vacancies approaches 10% of the total oxygen. These vacancies can be the result of high energy particle bombardment during the PLD process (at low pressure and high temperature, oxygen vacancies are easily generated) used so far by all researchers in the field to make these heterostructures. At the same time vacancies that are created will be filled by oxygen coming from the target and from the background gas. Fig. 1.21 shows schematically, the flow of oxygen in and out of the substrate.

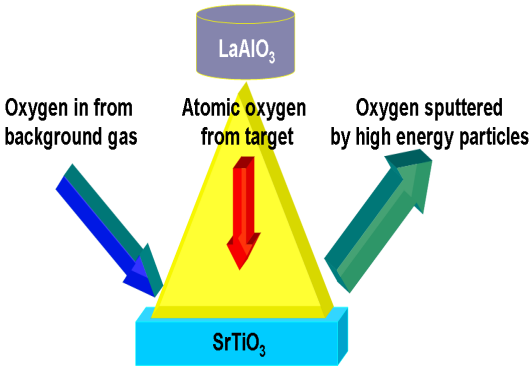

Figure 1.21: Illustration of the flow of oxygen in and out of the substrate.

In literature one can find several reports about oxygen vacancies. In a recent article, Yunzhong Chen et al. [84], reported that metallic interfaces can be realized in amorphous STO-based heterostructures by introducing oxygen vacancies near the STO substrate surface, suggesting that the redox reactions on the surface of SrTiO3 substrates play an important role. The significance of negative ions (O^-) for PLD oxide thin film growth is recently reported [85] for $La_{0.4}Ca_{0.6}MnO_3$ films grown in different background conditions on (001) STO where the best structural properties coincide with the largest amount of negative plasma species. The plume composition reveals a significant contribution of up to 24% of negative ions, most notably using a N_2O background. C. W. Schneider et al. [86], have demonstrated that the oxygen substrate contribution has to be taken into the overall oxygen balance when growing oxide thin films. They noted a substantial oxygen transfer between substrate and as-grown thin film, which indicates that the initially formed film is oxygen deficient and a chemical gradient is in favor of supplying oxygen via the substrate.

1.10.3.2 Lattice distortion

Since the unit cell of STO is slightly larger than that of LAO, one might expect a decrease of the out-of plane lattice constant for LAO films heteroepitaxially (i.e. pseudomorphically) grown on STO. In fact, a dilatation at the interface was observed by Maurice *et al*, using high resolution transmission electron microscopy (HRTEM) [87]. They argued that a Jahn–Teller like distortion is the reason for the elongation, which minimizes the electron energy: the two atomic sublayers LaO and TiO_2 across the interface form a unit cell of $LaTiO_3$, which has a larger lattice constant (by 0.065 Å for pseudocubic bulk unit cells). The d_{xz} and d_{yz} orbitals of the t_{2g} states are therefore lowered in energy compared to that for

the d_{xy} state. Implicit in this explanation is the trivalent nature of the titanium ion in this single LaTiO3 monolayer.

Vonk *et al* measured the initial structure of LAO on STO films for a deposition of less than one monolayer, using surface x-ray diffraction (SXRD) [88]. For a half occupied first monolayer of LAO, the displacements are qualitatively similar to those in the HRTEM results. A comprehensive SXRD study was performed by P. R. Willmott *et al.* [89], who studied a five-monolayer thick film. This study also confirmed the interfacial dilation. They explained the lattice deviations by simple ionic considerations of intermixed cations at the interface, described below.

1.10.3.3 Cationic intermixing

So far, we have considered the interface as abrupt and atomically perfect. The same chemical properties which make the perovskite structure so versatile, able to readily form solid solutions with different cations, are a liability in this case, because near the LAO/STO interface La and Sr cations can in principle intermix, doping the last STO layers with La^{+3} impurities. Although there are reports about the cation intermixing [90], recent measurements from our group [91] show that cation intermixing and oxygen vacancies are not the dominant cause of conductivity. As an example, the High-angle annular dark-field (HAADF) image shown in Fig. 1.22 was acquired using a NionUltraSTEM operating at 100 kV and resolves both cations and oxygen columns. This data attribute a minor role to oxygen vacancies and cation intermixing.

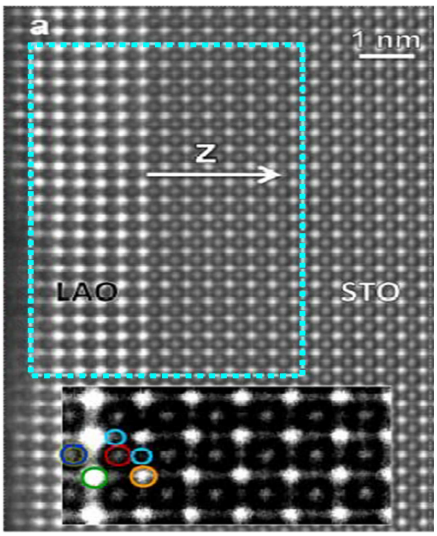

Figure 1.22: LAO/STO interface imaged by HAADF in a NionUltraSTEM operated at 100 kV. The inset is an enlarged portion of the image (raw data) with color coded circles indicating the position of each atomic column (red = Ti, blue = Al, yellow = Sr, green = La,cyan = O). The dashed region is the region used to calculate the atomic column positions. Taken from [91]

In this chapter, I have presented a contextual survey of the current experimental results and theoretical predictions obtained during the last years, concerning the Physics of transition metal oxides. In particular, an in depth review of the general characteristics of $Pr_{1-x}Ca_xMnO_3$ (PCMO) manganite compound and novel conducting interfaces of transition metal oxides (TMO) was described. The physics presented in this chapter provides the theoretical foundation necessary for understanding of the results presented in the remaining part of the thesis.

Chapter 2

Experimental Techniques

2.1 Introduction

A number of experimental techniques and characterization methods are used for the research work described in this thesis. TMO thin films can be characterized, using traditional solid state physics techniques, from the structural, electrical, magnetic and optical point of view. For most of the devices based on the epitaxial perovskite-type thin films and heterostructures, high-quality surfaces and distinct interfaces in between the constituent layers are usually prerequisite for good device performance. Therefore, the deposition of high quality TMO thin films and heterostructures and understanding the growth mechanism is very important. Epitaxial thin films characterized in this thesis work were grown by a special PVD technique called Pulsed Laser Deposition (PLD). Moreover, the growth can be monitored in real time by insitu Reflection High-Electron Energy Diffraction (RHEED), which makes it possible to examine the precise stack of the layers. The transport characterization of the thin films, after the fabrication process, was performed by using variable temperature four and two point methods in dark and under light irradiation. In this chapter, principles and descriptions of those experimental methods are given. First, I briefly describe the effect of strain in epitaxial TMO thin films. Next, I present the pulsed laser deposition technique and system used. Finally, electrical and optical characterization techniques are described.

2.2 The role of substrate

When manganites or other TMOs are prepared as an epitaxial film, the crystallographic structure can differ from that of the parent distorted bulk, often assuming a pseudo-cubic or a tetragonal structure. This is due to the biaxial stress imposed by the substrate that results in a strained film structure. This type of stress affects many physical properties of these TMO; hence the choice of the substrate is of primary importance. A substrate can have the following properties for the epitaxial growth: (i) it must be monocrystalline; (ii) crystallographic lattice match with the Mn compound; (iii) similar

thermal expansion coefficient; (iv) absence of chemical interactions with the material to be deposited; (v) surface quality; (vi) mechanical and chemical stability at the temperature and pressure conditions during the growth [92].

Oxide substrates with a square-planar surface orientation, as the (001) face of a cubic oxide crystal (see Fig. 2.1b), are ideal for films of compounds with cubic, pseudo-cubic and orthorhombic crystal structures. Other cuts may be also considered, for instance (110) is another face often used for deposition (Fig. 2.1b). Typically, the in-plane lattice spacing of the oxide film should closely match that of the substrate or exhibit a reasonably close near-coincidence site lattice match, such as by rotating 45^{o} with respect to the principal axes. The popular perovskite substrates used for the growth of manganites films, are $SrTiO_3$, $LaAlO_3$, and $NdGaO_3$ to name a few.

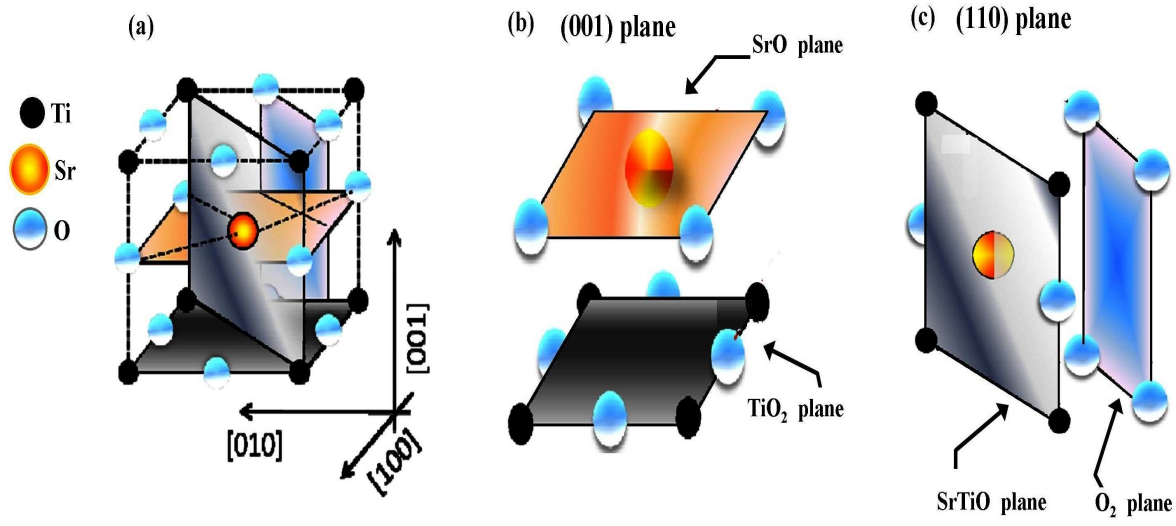

Figure 2.1: The crystal planes of STO (a) crystal lattice, (b) (001) plane with double termination and (c) (110) plane with double termination.

2.1.1 Strain effect in epitaxial oxide thin films

For the thin film deposition, a crucial role is played by the mismatch between film and substrate, inducing a strain on the growing film. Initially, a layer-by-layer growth takes place. Then, the thicker become the film, the higher is the elastic energy due to the strain. Beside this, the main difference should be between homoepitaxy and heteroepitaxy growth. In the first case, the substrate and deposited film compounds are the same and the substrate crystalline structure extends into the film during the growth. For the case of heteroepitaxy, the materials of film and substrate are different, with different lattice parameters. Such lattice

mismatch gives rise to a strain, tensile or compressive. The stress (strain) accommodated by a perovskite structure is mainly by using the internal degrees of freedom of the lattice, i.e. by rotation of MnO_6 (BO_6) octahedra, or small modifications of the Mn-O (B-O) bond lengths, leading to JT distortions. Since, an elastic energy increases with increase in the film thickness. When the thickness reaches a value, called critical thickness (d_C), the elastic energy stored in the structure is enough to create structural defects, or cracks. This d_C is related to the small *lattice mismatch* (δ):

$$\delta = \left(a_{sub} - a_{film}\right) / a_{sub} \qquad (2.1)$$

where a_{sub} and a_{film} are the in plane lattice parameters of substrate and film, respectively. The higher is the mismatch, the smallest is the critical thickness. Generally, the strain can be elastic, and a deformation of the in plane lattice parameter produces an out of plane deformation of the cell, too. When $\delta > 0$, it means that tensile strain on the deposited film is in plane while strain is compressed in out of plane axis. For $\delta < 0$, the strain is compressive, causing the lattice to be compressed in plane, but expanded out of plane. Finally, if $a_{sub} \approx a_{film}$ no strain is applied (see Fig. 2.2).

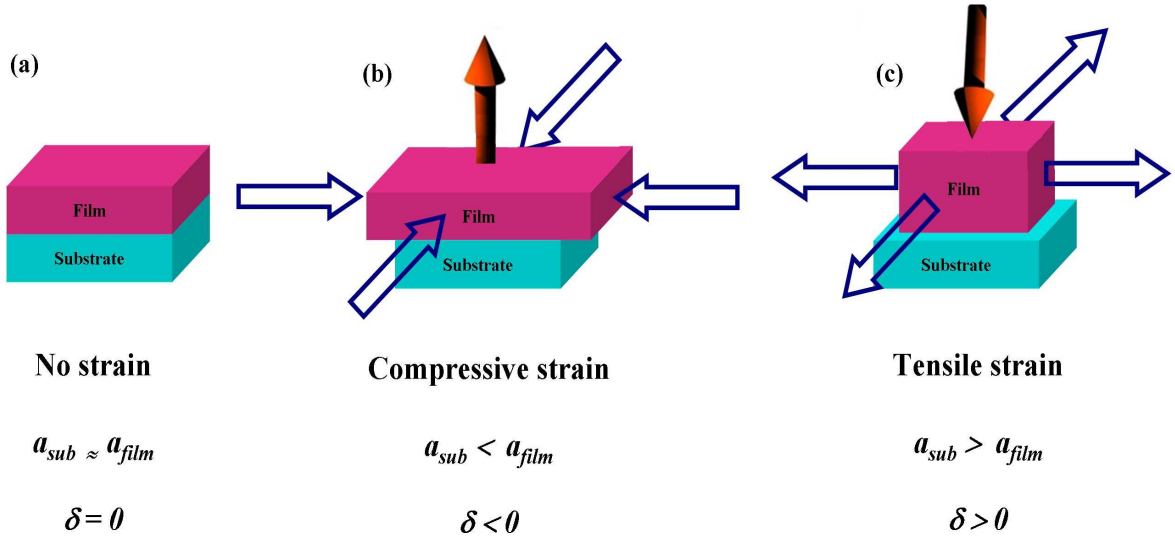

Figure 2.2: Effect of strain in thin films; (a) absent ($\delta = 0$), (b) compressive ($\delta < 0$), and (c) tensile ($\delta > 0$).

2.3 Growth technique

In order to achieve future technological devices based on manganite thin films or oxide heterostructures, the control over film fabrication and to understand their properties is of primary importance, since most technological applications require high quality crystalline

films and multilayers. Scientists have benefitted from different deposition techniques developed during the last years, and this resulted in the standardization of various methods, like sputtering, molecular beam epitaxy (MBE), metal–organic chemical vapour deposition (MOCVD), and pulsed laser deposition (PLD), to name a few. Although PLD has been used to make films since the 1960s, successful fabrication of a superconducting $YBa_2Cu_3O_7$ (YBCO) epitaxial film, giving a good critical current, during the years 1987-88, led to rapid development of this method [93, 94]. Since then, PLD has been extensively used to fabricate epitaxial films of superconducting, metallic, ferroelectric, ferromagnetic oxides and their multilayers. The basic principle of the laser ablation process is briefly described in the following section.

2.3.1 The Pulsed Laser Deposition (PLD) technique

Pulsed-laser deposition (PLD) has gained a great deal of attention in the past few years for its ease of use and success in depositing materials of complex stoichiometry. The basic concept of the laser ablation is the following [94]. A pulsed highly energetic laser beam, with a duration of tens of nanoseconds, hits a target of the desired material. If the laser energy density is sufficient for ablation of the source target, the material (highly ionized and energetic particles) evaporates, perpendicular to the target surface, forming a gas plasma with a characteristic shape that is called *plume* (see Fig. 2.3).

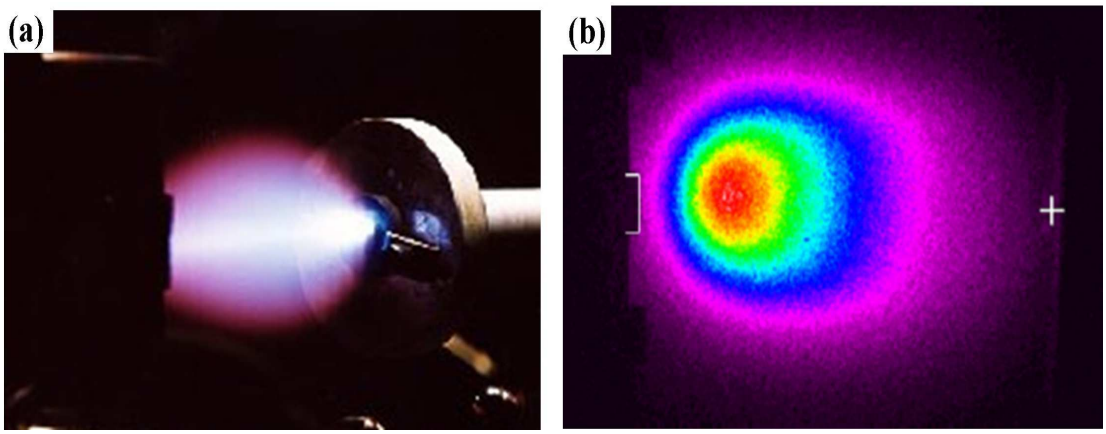

Figure 2.3: The plasma plume (a) photograph (b) expansion from the target (right) to the substrate (left). This image (b) is taken by the ICCD camera of the MODA system.

The plume consists of a mixture of atoms, molecules, electrons, ions and clusters. During its expansion, internal thermal and ionization energies are converted into the kinetic energy (several hundreds eV) of the ablated particles. The kinetic energy is then attenuated

due to multiple collisions occurring during expansion into the background gas. For oxides, the background gas is usually oxygen at a typical pressure in the range 0.01 - 0.5 mbar. Finally, the plume condenses on a heated substrate placed in front of the target, forming a thin film on it. Briefly, the thin film formation by PLD, can be divided in the following four stages.

1. Laser radiation interaction with the target
2. Dynamic of the ablation materials
3. Deposition of the ablated material on the substrate
4. Nucleation and growth of a thin film on the substrate surface

The physical quantities that are controlled are the fluence of the laser on the target, the background oxygen pressure, the distance between target and substrate and the temperature of the substrate. Both the temperature of the substrate and the oxygen partial pressure influence the size and the shape of the plume, and consequently the deposition rate, while the choice of the energy and the repetition rate of the laser determine the energy of the atoms and ions that impact the substrate [94, 95].

2.4 The experimental set-up

The performance and lifetime of oxide based electronic devices depend upon their purity, structural perfection, homogeneity, and the flatness and abruptness of the layer surfaces and interfaces. This indicates the importance of the control over the growth mode during the thin film deposition which determines the layer and surface perfection. Therefore, an atomically controlled fabrication process is needed for top performance in new applications. This can be accomplished by pulsed laser deposition assisted by reflection high-energy electron diffraction. Infact, the fast development in the performance of thin film based devices forces the characterization of the thin films, during and after the deposition, to be performed with the highest precision. After the relevant phenomenology and constituent materials have been described in the previous sections, now the experimental methods employed for fabrication, structural and transport characterization of the TMO samples will be presented. The results obtained will be discussed in the subsequent chapters in detail.

2.4.1 MODA system

The TMO thin films (like manganites, $Pr_{1-x}Ca_xMnO_3$) and interfaces, characterized in this thesis, were fabricated by a PLD technique, using RHEED-assisted laser ablation in a

complex experimental setup named MODA (Modular facility for Oxides Deposition and Analysis) complex system (figure 2.4) at the CNR-SPIN laboratory, Naples, Italy.

This facility is a system for pulsed laser deposition (PLD) of oxide thin films and for the *in situ* analysis of their properties. From figure 2.4, it is seen that several surface science techniques have been setup: *Reflection high-energy electrons diffraction*-RHEED, fast *Intensified Charge Couple Device* -ICCD camera, *Spot Profile Analysis-Low energy electrons diffraction-SPA-LEED, X-ray Photoemission Spectroscopy*-XPS, *Scanning Tunnel Microscopy-STM and Atomic Force Microscopy- AFM*. The ablation plasma is produced by focusing the output beam of a KrF excimer laser on stoichiometric targets.

This system mainly consists of two major parts: thin film growth chamber and the analysis chamber. More details about these two parts are presented elsewhere [96, 97]. Here, I briefly describe the growth chamber.

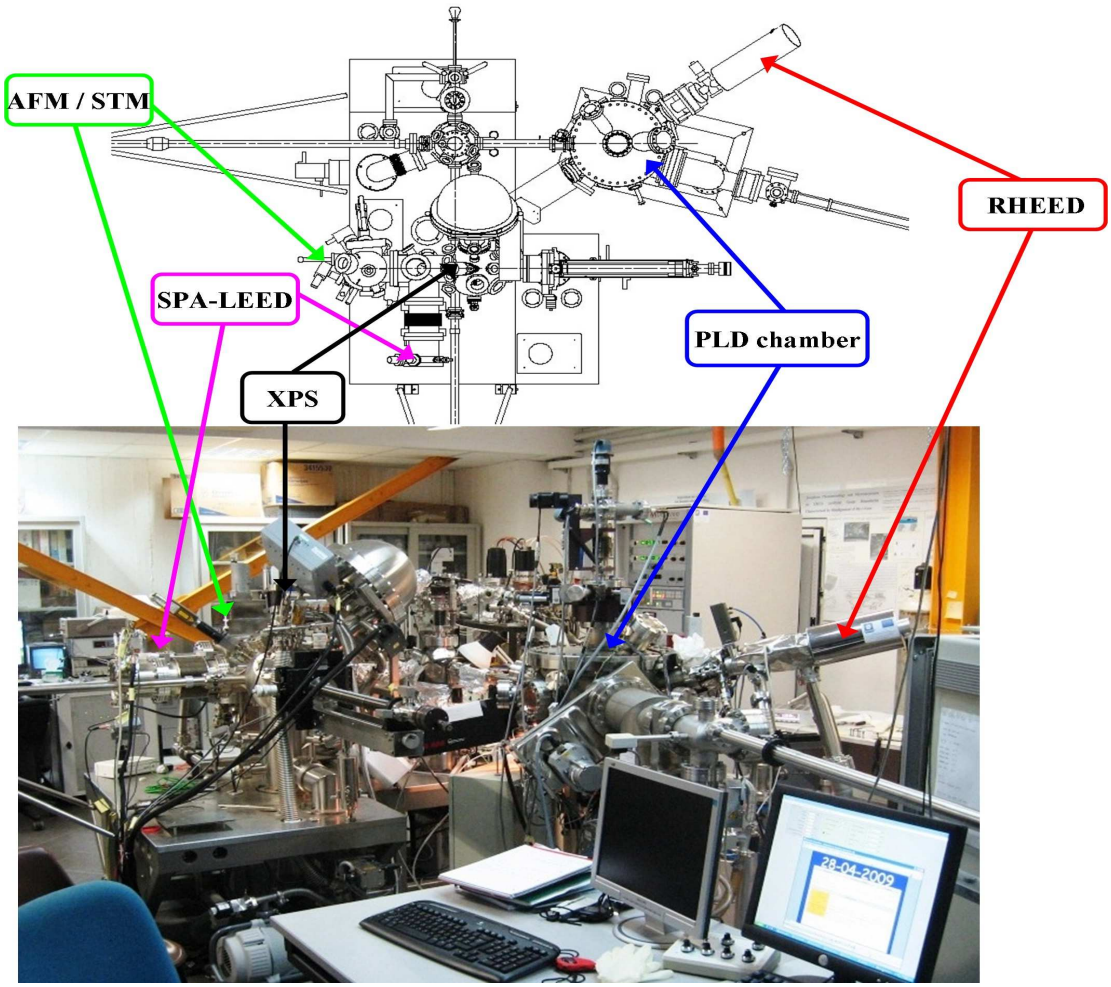

Figure 2.4: MODA facility in Naples, Italy, schematic top view (up) and photo (down).

2.4.1.1 The growth chamber

Thin film growth in MODA takes place in a vacuum chamber devoted to the pulsed laser deposition process (PLD). It is equipped with an excimer laser, a multistage rotating carousel on which it is possible to mount up to six different targets, a heater and a special High Pressure Reflection High Energy Electron Diffraction (HP-RHEED) set-up, allowing the in-situ growth monitoring also at high oxygen pressure (Fig. 2.5).

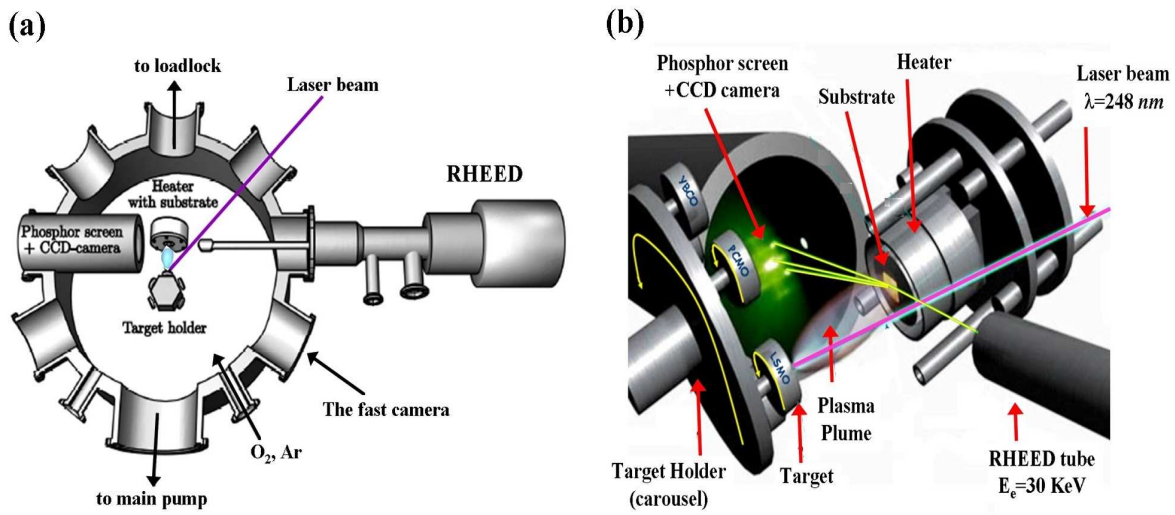

Figure 2.5: PLD growth chamber in MODA system; (a) sketch of growth chamber, and (b) internal zoom view, RHEED, plume and targets are clearly visible.

The base pressure in the chamber is in the range of 10^{-9} mbar. UHV conditions are maintained by means of mechanical and turbo-molecular pumps. It is isolated from the other part of the UHV system by valves and long channels that are used for the transfer rods but at the same time they introduce high vacuum resistance, making it possible to keep different UHV conditions in different parts of the MODA system. A separated load-lock chamber for the target introduction is also present, making it possible to introduce new targets without influencing UHV conditions (breaking the vacuum) in the growth chamber.

For the deposition, the substrate is glued on a sample holder (with silver paste) and introduced into the growth chamber. Then it is radiatively heated from the back using a heater based on wire made of a platinum alloy (or, alternatively, special alloys such as Kantal or Nicrofer are used). The deposition temperature is read by a thermocouple (calibrated by pyrometer) and controlled by means of an electronic feedback system. The maximum deposition temperature is 1000^{o} C. When growth substrate temperature is reached and the

geometrical position of the substrate regarding the target is set by means of step-motor positioning system, the deposition process starts. The motion of the heater, the pressure, the laser, the temperature, the loading and motion of the target carousel (selection of the targets) are fully software controlled.

After attaining growth substrate temperature, depositions are performed in a fully software controlled mode. The geometrical degrees of freedom of the substrate holder, equipped with five independent software controlled stepper motors (xyz-rotation stage, tilt angle θ and the azimuth angle ϕ), are able to change at any time, even during the experiments, the positioning of the substrate in the plume. When depositing oxide films, control of the oxygen pressure is of great importance. It influences the dynamics and shape of the plume (and also the transport properties of the grown films) but at the same time is of great importance for keeping the deposited films well oxygenated. The PLD of complex oxides is performed using 99.999% oxygen as a deposition gas.

The laser ablation is done by KrF excimer laser Coherent COMPEX 200 operating at λ = 248 *nm*, t_{pulse}= 25 *ns* full width half maximum, spectral width 1pm, laser energy per pulse 400-600 *mJ*, repetition rate 1-50 *Hz*. A mask is used to select the homogeneous central part of the laser beam. The mask is projected at an inclination of 45^{o} on the target by means of a focusing lens (the focal length is 50 *mm*). Moreover, each target was mounted on a rotating holder, to avoid drilling phenomena that may cause the ejection of big clusters from the target during ablation.

2.4.1.2 Reflection high-energy electrons diffraction (RHEED)

In the MODA growth chamber, deposition process is monitored in-situ by a high pressure Reflection High Energy Electron Diffraction “RHEED” (zoom view in Figure 2.5 (b)) that operates also in the regime of high dynamic oxygen pressure due to the differential pumping mechanism allowing the filament, that produces electrons, as well as accelerated electron optics, to be at the low base pressure while the deposition is done in dynamic O_2 pressure. RHEED allows to determine in-situ the growth mechanism and to monitor the evolution of the surface structure with sub-monolayer sensitivity [98, 99]. This technique uses elastic diffraction of electrons by surface atoms (there is no energy transfer from the electrons to the surface) with high kinetic energy (typically in the range of 5-50 keV) and low impact angle (typically less than 5) from the solid surface to provide information about the periodic rearrangement of the surface atoms. The reflected electrons than impinge on the phosphorous screen reveling a pattern that depends on the structure, morphology and

roughness of the sample surface. The pattern represents the intersection of the reciprocal lattice of the two dimensional surface layer (ideally a lattice of rods) and the equi-energetic sphere in *k space* (Ewald sphere).

With a RHEED experimental set-up, two types of measurement can be performed: the analysis of the *RHEED pattern spots intensity* variation (oscillation) during the film growth (Figure 2.6 (a)), and the study of the *RHEED pattern* of a well defined surface, before and after the deposition (Figure 2.6 (b) and (c)). As an example, a cross sectional view along the white line of RHEED pattern after 6uc deposition of NGO film is shown in figure 2.6 (c). The typical RHEED pattern tells that, in the case of a single domain crystalline, clean and atomically flat surface, the diffraction pattern results in sharp streaks lying on concentric circles (Laue circles). While in case of a three dimensional surface, the RHEED diffraction pattern is a rectangular pattern of spots. Beside the structural analysis of the planar surface symmetries, the intensity of specular spot (rod) depends on the film roughness making it possible to monitor the film growth in the layer by layer growth regime by observing the oscillation of the intensity. A single oscillation is completed when a complete atomic layer is deposited as represented in zoom view of figure 2.6 (a). The intensity of the specular spot decreases by increasing the number of layers, an indication of a progressive roughening of the surface that it is common in the epitaxial growth.

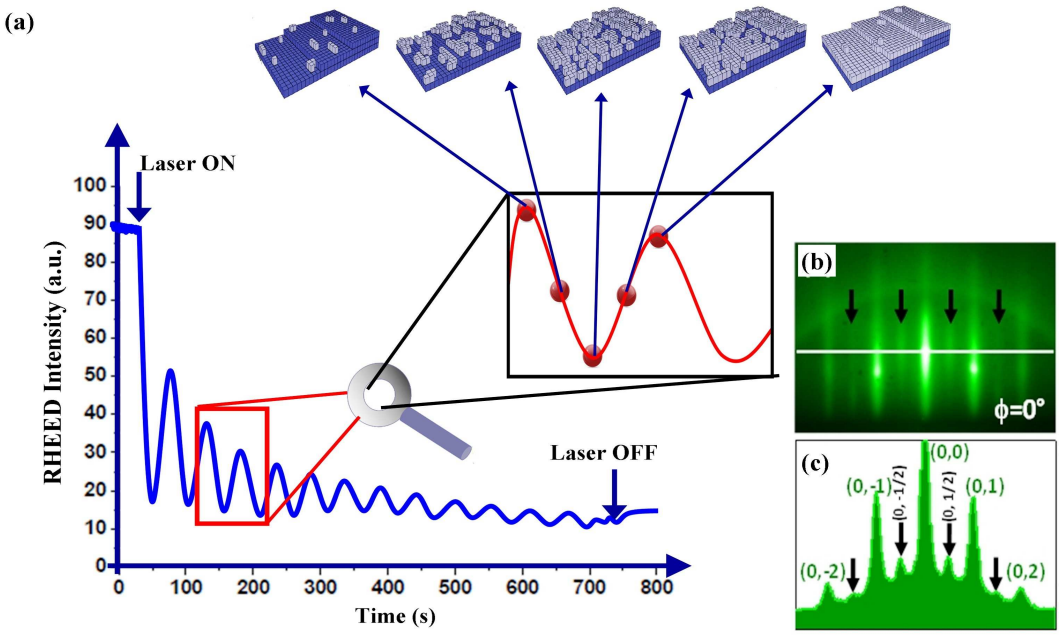

Figure 2.6: The RHEED oscillation of the specular beam during the growth; (b) RHEED pattern after 6uc deposition of NGO film; (c) cross section along the white line of Fig.2.6 (b).

As, the control of the film surfaces and interfaces is strongly related to in-situ monitoring of the film growth to get optimal properties for possible technological developments of the oxide based devices. Hence, the control of the interfaces at the micro and nano-scale is of enormous relevance, in order to achieve the best performances in such structures. Indeed, the higher degree of control has a cost in terms of easiness, because the RHEED-assisted PLD is far more complex than standard PLD.

2.4.2 Device characterization laboratory

A schematic view of the device characterization laboratory in Naples, Italy is shown in Fig. 2.7. It mainly consists of a Janis closed cycle refrigerator (CCR) system along with Keithley's standard instruments for sample biasing and voltage and current read out.

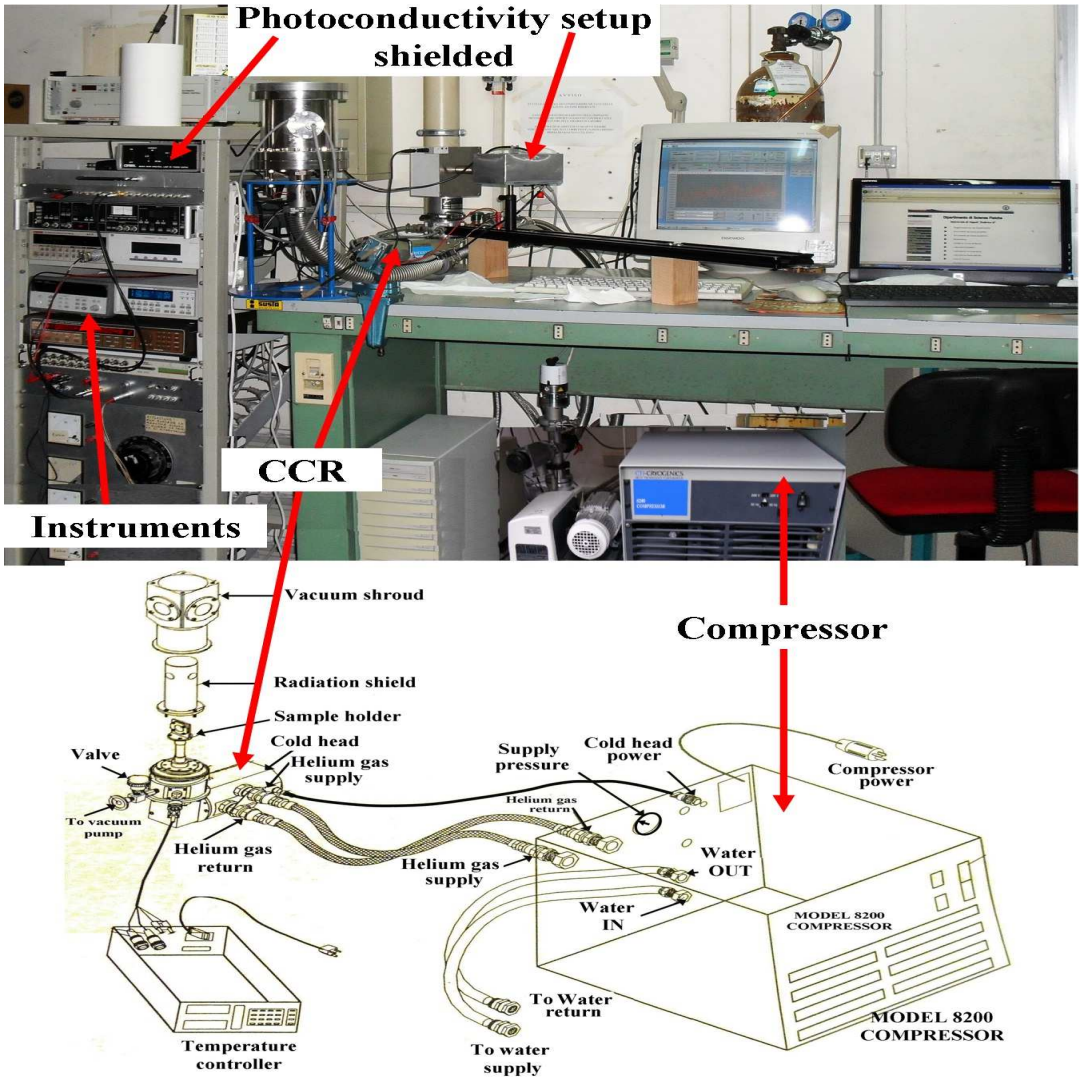

Figure 2.7: Device characterization lab. in Naples, Italy, photo (up) and top schematic view (down).

Besides this, during my PhD tenure, I was also involved in setting up of the following instruments which resulted in the up-gradation of the existing transport setup.

(a) an homemade magnetic field setup that can provide up to 15 mT field both in-plane and out of the plane geometry (Fig. 2.8a and b). This setup is suitable for performing a speedy check on some of the samples which are sensitive to the external magnetic field environment.

(b) another homemade unit is the setup for photoconductivity measurements, consisting of an Hg (A) lamp model 3660 by ORIEL instruments with lamp supply (20 *mA*), fully shielded to avoid any free exposure to the air/eyes (Fig. 2.8e and f).

A group photo of all the accessories that are part of the device characterization laboratory is shown in Fig. 2.8 below, along with an Agar sputter coater and an ultrasonic bonder.

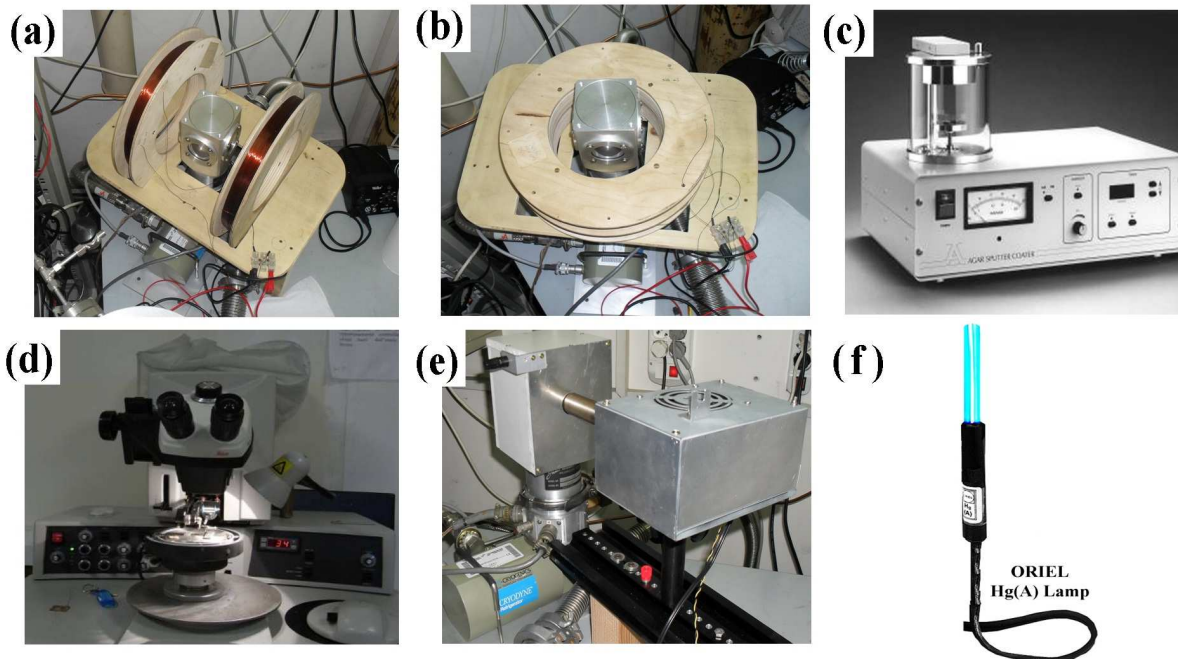

Figure 2.8: Other accessories in the device characterization laboratory, magnetic field setup (a) field in the sample plane (b) field out of the sample plane, (c) Agar sputter coater (d) an ultrasonic bonder (e) photoconductivity setup fully shielded, and (f) Lamp used in Fig. 2.8 (e)

2.4.2.1 Closed-cycle Refrigerator System (CCR)

The closed cycle refrigerator (CCR) system, combined with an automatic temperature controller, is a powerful tool for studying the properties of materials over a wide range of temperatures (with base temperature ~ 10 K). Temperature sensors are standard items in the CCR systems. There are commonly two types of standard sensors used (installed on the cold

finger): First, a silicon diode is the most common and used often for low temperature measurements (attached with our setup). The second, a platinum resistor is used for high temperature measurements. In a few cases thermocouples are also used, but they are exceptions. The temperature controller is another standard piece of the CCR system. We use the Lakeshore model 331 as a temperature controller with our measuring setup that can supply 1 ampere of heater output.

The CCR system, as the name implies, require no liquid helium or liquid nitrogen as a source of cooling. Instead, a closed loop of helium gas is compresses and expanded, based on the Gifford-McMahon (G-M) thermodynamic cycle (see Appendix 1). Furthermore, during the expansion phase of each cycle, heat is removed from the cold finger, on which the sample is mounted. A compressor is used to provide the high pressure helium gas needed for the cycle to the cold head. It can be either air cooled or water cooled. Flexible stainless steel gas lines deliver the compressed helium gas to the refrigerator, and return the low pressure gas to the compressor for recirculation. The refrigerator includes two cold stages, one for cooling the sample and one for cooling a radiation shield that surrounds the sample (see Fig. 2.7).

2.4.2.3 Setup for photoconductive measurements

Fig. 2.9 shows a schematic of a homemade photoconductivity setup used in this study. This set-up was developed for electrical and photoconductivity measurements (in both constant current and pulsed current regimes) in the temperature range from 10 to 300K.

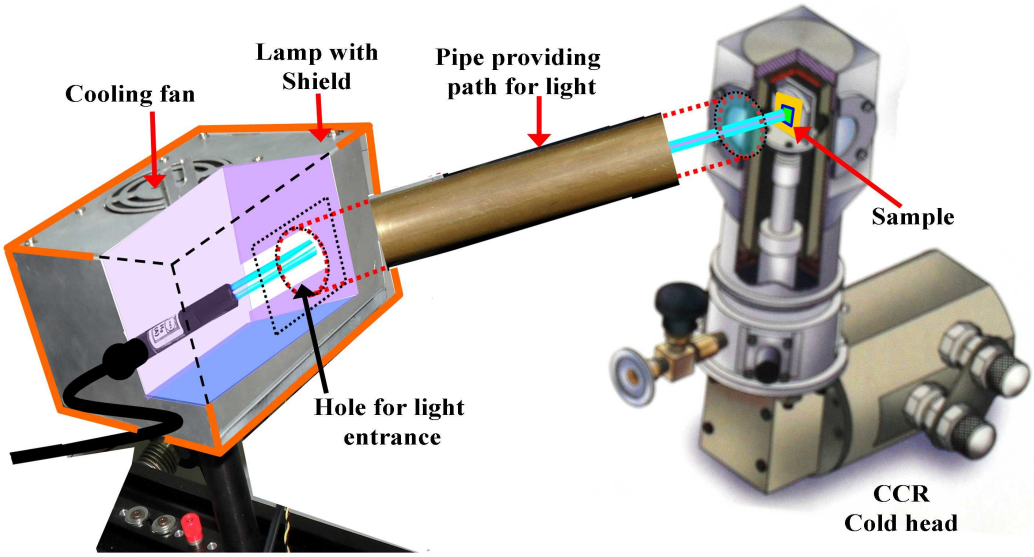

Figure 2.9: Schematic diagram of setup for photoconductivity measurements.

Our set-up for photoconductivity (PC) measurements consists of three main parts, each one of which can be modified depending on the experimental tasks to be performed. These are: optical part, detecting part (scheme of the electrical connection and sample biasing as described in Fig. 2.11) and cryogenic part (see Fig. 2.7), which include a sample holder and a cryogenic system for measurements in the temperature region from 10 to 300K. Here, the illuminating source consists of an Hg (A) lamp model 3660 (Fig. 2.8 (e) and (f)) with lamp supply (20 mA) by ORIEL instruments, fully shielded to avoid any free exposure to the air/eyes. The lamp supply is capable of providing dc and ac current to bias the lamp. There is a small fan mounted inside the protection shield box capable of removing the heat produced inside the box and serve as a cooling source for the Hg (A) lamp. When the lamp is turned ON, after few seconds, it fully illuminates the box internally, and the light emerges through a small hole made in the box. There is a small path (~ 6 inch copper pipe), that provides a passage for the light to reach the device under test (DUT), which is placed in the vertical position on the sample holder inside the CCR system.

2.5 Measurement techniques

This section briefly describes the experimental techniques used to characterize TMO thin films and heterostructures. Special care needs to be taken in case the sample is susceptible to photo induced carriers, which can be minimized by keeping the sample before and during the measurement in a dark environment.

2.5.1 Electrical contacts

There are numerous reported methods that claim to create ohmic contacts with the 2DEG: some that require complicated procedures and some that are very simple. I have attempted to create ohmic contacts by the following means: silver epoxied copper wires, thermally evaporated silver contact pads, and aluminum wire-bonding. The very first attempt to create contact pads was done using silver paint (paste) to connect fine gauge copper wires to the surface of the film. This procedure worked rarely for the insulating manganite thin films (e.g., PCMO), and worked once out of dozens of attempts for the interfaces to allow 2DEG's sheet resistance to be measured. Secondly, I deposited silver contact pads using an *AGAR* scientific sputter coater (Fig 2.8c). A contact shadow mask, manufactured by a laser machine, was used for this purpose that created four 0.1 mm diameter contact pads on the 5x5 mm sample. This method, promising from reported success, also worked very well for our insulating manganite (PCMO) thin films.

2.5.2 Wire-bonding: probing the buried interface

The electrical contacts were obtained by ultrasonic bonding of Al wires on silver stripes spaced 0.1 mm apart (for PCMO). The most tedious part of measuring the transport properties of the 2DEG between polar perovskites and STO is creating contact with the buried interface. Ultrasonic wire-bonding proved to be the most successful way to reproducibly make contact with the buried 2DEG. We use Kulicke & Soffa Industries Inc model 4523, manual aluminum wedge-wedge wire-bonder (Fig. 2.8d). This type of wire bonder operates by pressing a thin gauge wire onto a surface, then ultrasonically heating the wire, which creates the bond. The theory behind the wire-bonder's success is that the ultrasonic energy supplied to the wire-bonder's tip creates micro-cracks in the film and thus allows the melted aluminum to penetrate to the buried interface.

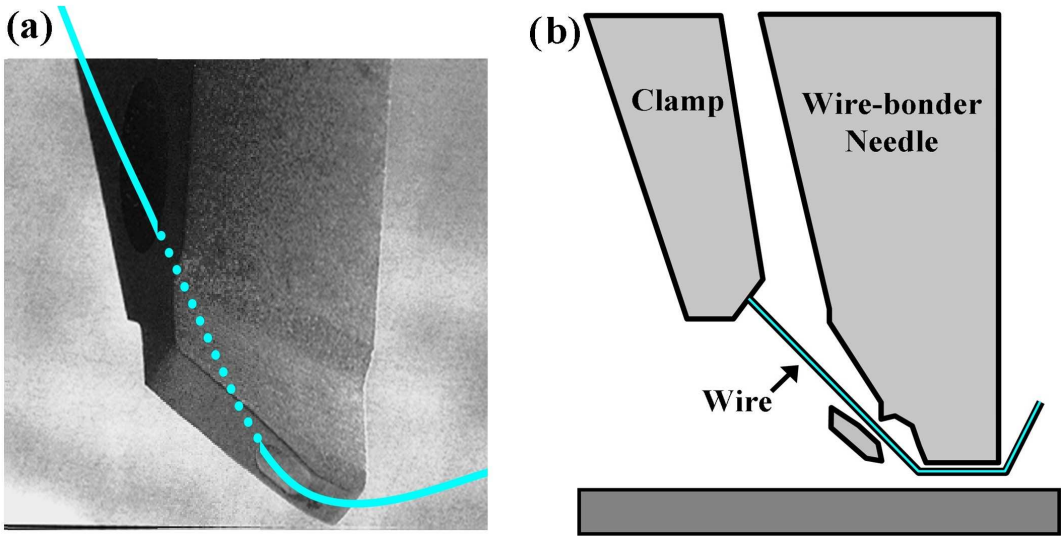

Figure 2.10: This is a side view of the wedge-wedge wire-bonder; (a) 3-d view of needle, and (b) schematic diagram

The downside to this method is that the operation of the wire-bonder requires a lot of practice. A schematic of the wire-bonder's tip is shown in Fig. 2.10, where the fine wire of Al or gold (diameter 25 μm) enters from the rear of the setup and is held in place via a pneumatic clamp. For the wire-bonding process, a home made sample holder with thin copper base that has a cavity size of 6 x 6 mm is used. This holder holds the substrate in this cavity, has 16 gold (as well as copper) contact pads specifically intended for wire-bonding, which makes the connections to the different probes very easy. For good thermal contact,

thermal grease is used to avoid the temperature gradient and different cooling rates between the copper block and the sample.

2.5.3 Electrical transport measurements

The transport measurements were carried out in standard two-probe and four-probe configurations with in-line geometry. The resistance vs. temperature R (T) was measured in the current-pulsed mode, by biasing the samples with an active current source (Keithley 238) and measuring the voltage drop with a nano-voltmeter (Keithley 182). The temperature measurement was done using a *Lakeshore* temperature controller model 331. The four-point method involves using four leads attached at different parts of the sample (Fig. 2.11a). Two external pads supply current (if Ag-pads are considered), while other two inner pads measure the voltage drop. Furthermore, in order to perform electrical transport, we employed the Van der Pauw four-point method. Taking into account the van der Pauw formula, the sheet resistance R_{Sheet} was calculated by Eq. 2.2;

$$R_{Sheet} = \frac{\pi R}{\ln 2} \qquad (2.2)$$

The highly resistive samples like PCMO require use of the two-point probe method to measure resistances down to a low temperature scale provided narrow contact pads are deposited on it, as shown in Fig. 2.11b below.

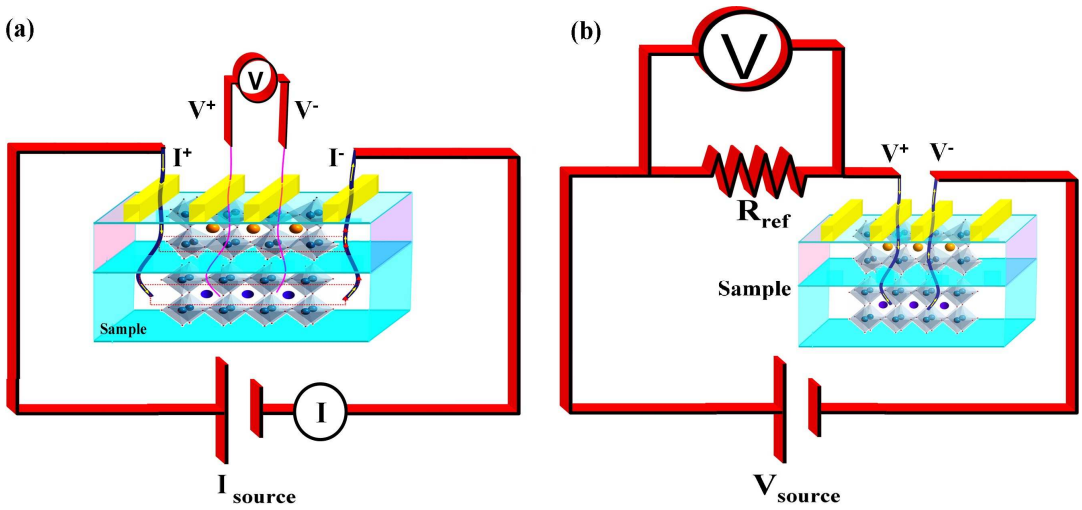

Figure 2.11: Measurement techniques with circuit diagrams; (a) four-point probe, and (b) two-point probe methods. The geometry of the silver contact pads on the sample is also shown schematically.

By using a 4-point configuration (as opposed to only 2 contacts), there should be no contribution to the measured resistance from the wire-silver pad interface, the so-called contact resistance. The measured resistance R was then converted into resistivity ρ values by using Eq. 2.3, where A is the cross-sectional area that the current flows through and l is the distance between the voltage contacts.

$$\rho = \frac{R\,A}{l} \qquad (2.3)$$

There is some degree of ambiguity as to the appropriate cross-sectional area to use in Eq. 2.3, as the value will depend on the precise path the current takes through the film. Throughout this work, it has been assumed that the current flows uniformly throughout the width of the film. The resistivity values obtained should be treated an upper bound, as the area the current travels through may be restricted, e.g. if there is phase separation. However, it should be noted that the main aim of the electrical transport measurements was to determine the temperature (if any) of a transition from an insulating state (defined as $d\rho/dT < 0$) to a metallic state (defined as $d\rho/dT > 0$). This can be done from resistance values alone, but the absolute resistivity values are included for comparison with other materials. In addition, it was possible to apply an external magnetic field of up to 12 mT while performing R (T) to perform a quick check on some of the suitable samples. Temperature dependent resistance measurements are recorded during the cool down as well as warm up. To add few more words, cooling down to 10 K was done over the course of at least 1 ½ hours, and warming up to room temperature was done over the course of 4-6 hours (fast warming is also possible when internal heater is turned ON). The slow warm up ensures that the temperature gradient between the copper block and the sample is minimized. The cooling, heating rate and the applied magnetic field were all computer controlled by a LabView™ code.

2.6 Experimental difficulties

There are many experimental difficulties encountered in this part of the experiment. First, creating good contact with the interfacial 2DEG using the wire-bonder is difficult to achieve. Wire-bonding is an extremely tedious process that requires precision and patience, and, most importantly, the ability to feed the fine gauge wire into the hole (shown in Fig. 2.10) at the back of the wire-bonder's needle tilted of 30°, when things go wrong. So one has to hold the wire tilted with the same orientation for insertion. Furthermore, once the contacts are made, sometimes the checking of two wire resistances (can be measured between wire-

bonds) by using a digital multimeter (DMM) give unpredictable results. One side of the sample show higher values of resistance than the other side. This is likely due to a high contact resistance between the wire-bonded lead and the 2DEG, and repeated (more bonds) wire-bonding can sometimes remedy the problem. Also, during the warm up path of a resistance measurement, turning the internal heater ON creates jumps in the sheet resistance data. Thus these measurements are simple in principle but can be tricky in practice.

Chapter 3

Transport properties of narrow band manganite thin films

3.1 Introduction

In this chapter I will discuss the transport properties of the epitaxial films of $Pr_{0.7}Ca_{0.3}MnO_3$ grown on (110) and (001) STO substrate. The main objectives behind this research work are, firstly, to see how far the transport properties of this complex compound (i.e., PCMO) can be qualitatively modified by the application of an external perturbation (e.g., biaxial stress imposed by the substrate or photon field). Another related issue regards the study of the transport mechanisms of thin $Pr_{0.7}Ca_{0.3}MnO_3$ films on (110) and (001) STO, and their comparison with the bulk ones and to assess whether the epitaxial strain brings PCMO_110 to a metallic or to an insulating FM single phase. Finally effect of UV light will be discussed.

3.2 Brief background

Transport and magnetic properties of PCMO show dramatic changes at temperatures around the combined ferromagnetic-paramagnetic and metal-insulator transitions. The ferromagnetic phase is usually explained by introducing the double-exchange mechanism, in which hopping of an outer shell electron from a Mn^{3+} to a Mn^{4+} site is favored by a parallel alignment of the core spins. Beside double-exchange, a strong interaction between electrons and lattice distortions plays a vital role in this compound. Furthermore, for the Mn^{3+} site, with three electrons in the energetically lower spin triplet state t_{2g} and the mobile electron in the higher doublet e_g, a Jahn–Teller distortion of the oxygen octahedron can lead to splitting of the doublet and the trapping of the charge carriers in a polaronic state influencing the transport properties in the high temperature phase. Additionally, small distortions of the unit cell have dramatic effect on PCMO, opening the perspective of tuning its transport (electronic) and magnetic properties by depositing epitaxial films on different substrates, i.e., under different biaxial stress conditions as shown in Fig. 3.1.

The substrates choice is based on the phenomenological observation that the unit cell deformation imposed by the biaxial stress for manganite films grown on (110) and on (001)

perovskitic substrates is quite different. The choice of the STO (110) substrate was dictated by different considerations. Firstly, both compressive and tensile growth of PCMO on a (001)-oriented cubic substrate would have resulted in tetragonal elongated or compressed PCMO, with stabilization of the AFM phase, in the guise of A type (or CE-type) and C-type structures, respectively [100].

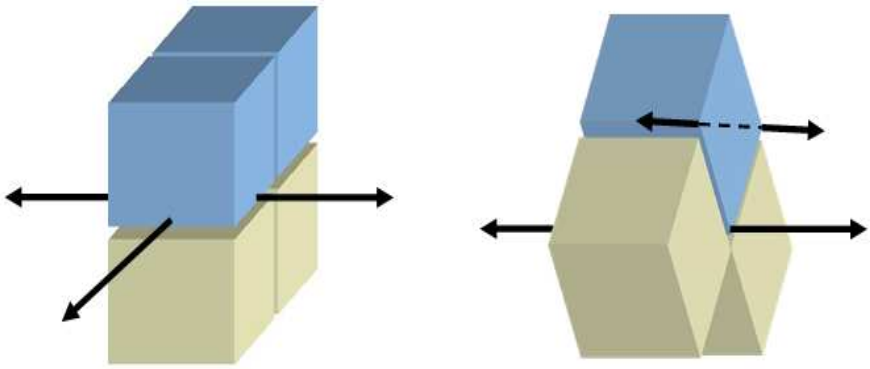

Figure 3.1: Sketch of the different biaxial tensile stress applied by (001) STO (on the left) and (110) STO (on the right) on a matched pseudocubic perovskite with lattice spacing shorter than a_s = 0.3095 nm.

At contrast, deposition on STO (110), while putting the *c* lattice parameter of the Pbmn cell under tensile strain [see e.g., Ref. 101], thus inhibiting the compression along the [001] orthorhombic direction necessary for the A-type or CE-type AFM structures to set in, at the same time retains the PCMO orthorhombic symmetry, which allows mixed occupancy of both $d(x^2\text{-}y^2)$ and $d(3z^2\text{-}r^2)$ e_g orbitals, a condition favorable to isotropic ferromagnetic superexchange. Secondly, if strain along [001] in PCMO is at least partially accommodated via bond angle modification, deposition on STO (110) will promote the opening of the Mn-O-Mn bond angle and, by consequence, the widening the e_g band at least along k_z, favoring DE.

3.3 Experimental

3.3.1 Materials

The samples chosen for this work are two sets of $Pr_{0.7}Ca_{0.3}MnO_3$ (PCMO) epitaxial films on the basis of their thickness (i) t~150 *nm*) and (ii) (t~10 *nm*), respectively, grown by pulsed laser deposition on (001) and (110) $SrTiO_3$ (STO) substrates. In the following, the two samples above will be respectively called PCMO_001 and PCMO_110. Bulk PCMO is orthorhombic, with lattice parameters $a = 0.5426\,nm$, $b = 0.5478\,nm$ and $c = 0.7679\,nm$. The

substrate lattice spacing, $a_s = 0.3905\ nm$, is matched to PCMO, being $c \approx 2a_s$ and $a \approx b \approx \sqrt{2}\ a_s$. This kind of pseudocubic orthorhombic film can be accommodated on STO in several ways [101, 102]. All the samples were fabricated in (MODA lab.) Naples, Italy.

3.3.2 Methods

The epitaxial $Pr_{0.7}Ca_{0.3}MnO_3$ films were deposited by pulsed laser deposition in the complex multichamber system. The films are grown in a 0.1 *mbar* oxygen atmosphere, at a rate of 2 unit cells per minute, by resorting to a Kr-F excimer laser (248 *nm*) that radiates a 2.4 mm^2 spot on the target with a fluence of $2J/cm^2$. The transport measurements were carried out in standard two-probe and four-probe configurations with in-line geometry. The R (T) was measured in the 4-probe mode (current-pulsed mode), by biasing the samples with an active current source and measuring the voltage drop with a nano-voltmeter. In addition 2-probe mode (constant voltage) was also employed. The electrical contacts were obtained by ultrasonic bonding of Al wires on silver stripes spaced 0.1 mm apart.

3.4 Electrical transport in narrow band manganite thin films

Narrow bandwidth manganites are, usually, insulating over the entire temperature range studied (e.g., see Fig.1.9). A list of samples characterized for this thesis work is shown in Table 3.1.

Table 3.1: A list of samples characterized for this thesis work consisting of several PCMO_110 and PCMO_001 samples.

Sample name	Thickness [nm]	$\rho_{(300K)}$ [Ω.m]
1). 06-104 : PCMO-001	10	5.3×10^{-3}
2). 07-102 : PCMO-001	50	26.2×10^{-3}
3). 08-017 : PCMO-001	11	17.7×10^{-3}
4). 09-088 : PCMO-001	10	1.6×10^{-3}
5). 09-110 : PCMO-110	35	2.9×10^{-3}
6). 09-111 : PCMO-110	35	4.5×10^{-3}
7). 10-018 : PCMO-001	150	11.3×10^{-3}
8). 10-020 : PCMO-110	150	24.8×10^{-3}
9). 10-022 : PCMO-001	150	8.9×10^{-3}
10). 10-061 : PCMO-001	10	2.6×10^{-3}
11). 10-066 : PCMO-110	10	62.9×10^{-3}

As shown in Fig. 3.2, the resistivity of PCMO reveals an activated semiconductor like character over the whole measured range (~ 400K - 90K) in dark and without any external perturbation. The dashed regions containing noisy behavior (Fig. 3.2a) and drop (bend) in resistivity (Fig. 3.2b) are not considered here but will be discussed in coming section.

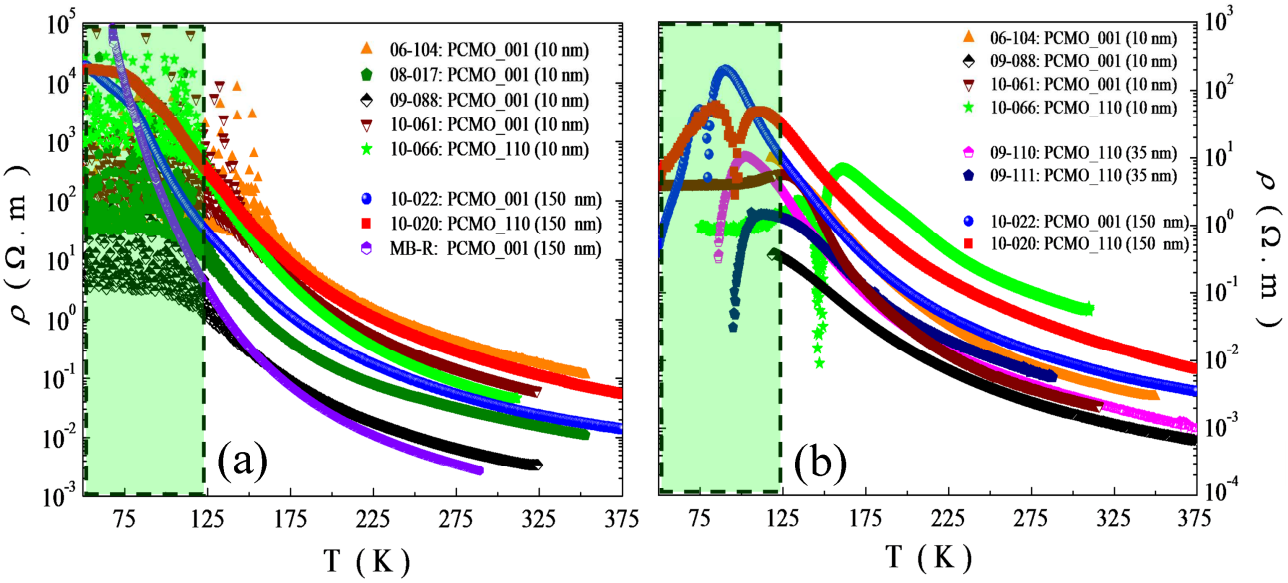

Figure 3.2: Temperature dependence of resistivity for several PCMO_110 and PCMO_001 samples (of different thickness), all showing insulating behavior; (a) 2-probe method and (b) 4-probe method. Dashed region is not included.

Infact, the above data (Fig. 3.2) was obtained in both 2-probe and 4-probe configurations, which show qualitatively similar insulating behavior in a quite broad range of temperature, but from here on I prefer to show data in this section with 2-probe method. Furthermore, Fig. 3.2 show data which consists of R (T)s of several samples of PCMO_110 and PCMO_001 also as a function of difference in thickness (Table 3.1). Before showing the main results, let us briefly describe the main models describing electric transport in manganites.

3.4.1 Thermally activated hopping/Arrhenius

In literature [103], one can find the generalized form of resistivity for activated-hopping conduction as,

$$\rho \propto \exp\left(\frac{T_O}{T}\right)^{1/n} \qquad (3.1)$$

Here, n=1 correspond to the Arrhenius mechanism, n=2 is hopping by coulomb interaction and n=4 for variable range hopping [104, 105]. Arrhenius mechanism is generally used to model activated behavior. I will be confirming the type of hopping involved in our samples by finding this value of n.

3.4.2 Mott variable range hopping (VRH)

Mott variable range hopping (VRH) theory describes the low temperature behavior of the resistivity in strongly disordered systems where states are localized. If the activation energies for hopping to neighbouring atoms are not the same, then it may be that hopping to a non-nearest neighbour has a smaller activation energy. This is particularly true at low temperatures [106]. This variable range hopping is potentially more complicated to describe quantitatively (for derivation refer to [107]). From Eq. 3.1, one can write the VRH formula as,

$$\rho = \rho_{\infty} \exp\left(\frac{T_O}{T}\right)^{1/4} \qquad (3.2)$$

where T_0 is a characteristic temperature. One drawback of this model is that the values of T_0 are often implausibly high, (e.g. in the range of ~ 10^8 K). Another drawback with VRH is that it was originally proposed for short distance hopping at low temperatures. Furthermore, the mechanism may depend on the type of sample (single crystal, polycrystalline, or thin film).

3.4.3 Thermally activated hopping of small polarons (TAP)

The resistivity formula for polaron hopping conduction can be written as,

$$\frac{\rho}{T^s} \propto \exp\left(\frac{E_a}{k_B T}\right) \qquad (3.3)$$

Here, s=1 correspond to adiabatic polarons and s=3/2 means non-adiabatic polaron conduction. Since small polarons exist in the paramagnetic phase, it seems natural to adopt a small polaron model to describe the resistivity. Also strong electron-phonon coupling in narrow band manganites gives rise to the formation of small polarons, and the resistivity is governed by the thermally activated hopping (TAP) of small polarons. From Eq. 3.3 we can write,

$$\rho = \rho_0 \, T \exp\left(E_a \big/ k_B T\right) \qquad (3.4)$$

Where the prefactor ρ_0 is only a weak function of the temperature and the activation energy E_a does not depends on T. The hopping energy E_a corresponds to half of the polaron formation energy, and k_B is the Boltzmann constant. The applicability of Eq. 3.4 is limited to temperatures greater than half of the Debye temperature Θ_D [108, 109];

$$T \geq \frac{1}{2}\Theta_D \approx 162 - 172K \qquad \text{(for PCMO)} \qquad (3.5)$$

Because of the incorporation of variable interplays among charge, spin and lattice, these compounds exhibit complex transport behaviour and offer an unusual research opportunity for condensed matter physics. Many experimental results have provided strong evidence to suggest the presence of small polarons in the paramagnetic phase. Although it is becoming generally recognized that the presence of small polarons plays a key role in the peculiar transport properties for mixed-valence manganites [110], the true nature and the exact transport process in the paramagnetic phase for mixed-valence manganites is attractive but still controversial.

3.5 Strange features in early transport measurements

Before describing the main results, let me make few comments on the transport properties of PCMO (also concerning dashed region in Fig. 3.2). For the very early measurements (year 2008-09) on this complex PCMO compound, it was frequently observed some strange features in the R (T) data consisting of jumps (around 200-250K) and noisy behavior followed by a drop (bend) in the resistance around 130-150K (depending upon thermal history or aging of the sample) as shown in Fig. 3.3. Quite interestingly, these features were appearing at the points where phase transitions are reported in the phase diagram for bulk PCMO i.e., charge ordering temperature T_{CO} and the Néel temperature or magnetic ordering temperature , T_N, as shown by dashed lines in Fig. 3.3. Indeed, based on our measurements alone, we were unable to make any specific comment about the origin of these features. Because, on the one side these features in the R (T) data were very fascinating, but on the other hand in literature reported resistivity data were quite clean and smooth (at least down to 150 K) making above scenario more puzzling for us (see e.g., Fig. 1.8).

Moreover, the noisy behavior in the R (T) curves just before and after the drop in resistance (between 100-150K) look similar to what reported for single crystals below 40K, that was interpreted as temporal fluctuations between low and high resistance states [6].

There are also reports about colossal dielectric response and multiferroic nature in charge-ordered rare earth manganites in the above temperature window [111, 112, 113].

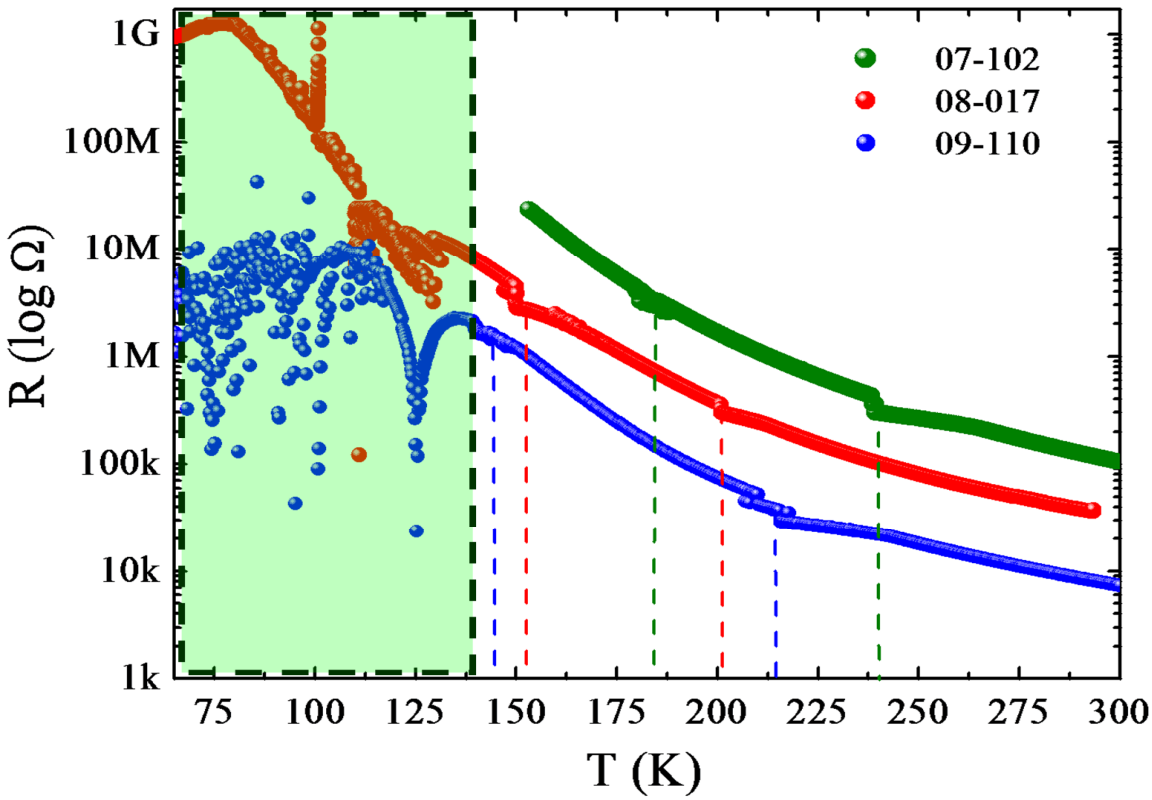

Figure 3.3: A set of early transport measurements (R vs. T) on several PCMO samples, showing jumps and noisy behavior.

A survey of the literature, however, made things more complex at that time. As an example see Fig. 3.4, for a quick comparison (with Fig. 3.3 or Fig. 3.6), which is taken from Refs. [114, 115], these authors reproduced this figure in several articles [114, 115], and reported that the ρ (T) s of the films with two different thicknesses are practically identical and show an obvious exponential behavior in the high-temperature region ($T > T_N$). However, in the low-temperature range ($T < T_N$), an abrupt change is observed in the temperature dependence of the resistivity, and that change can be interpreted as an appearance of the metallic phase. Moreover, they emphasized that, although the complete transition into the metallic phase is not seen, a forerunner of such a conversion is distinctly observed. After several measurements on PCMO samples, we found that this is a false FM transition (highlighted by dashed rectangle) and infact PCMO is seen insulating in R (T) measurements without any external field.

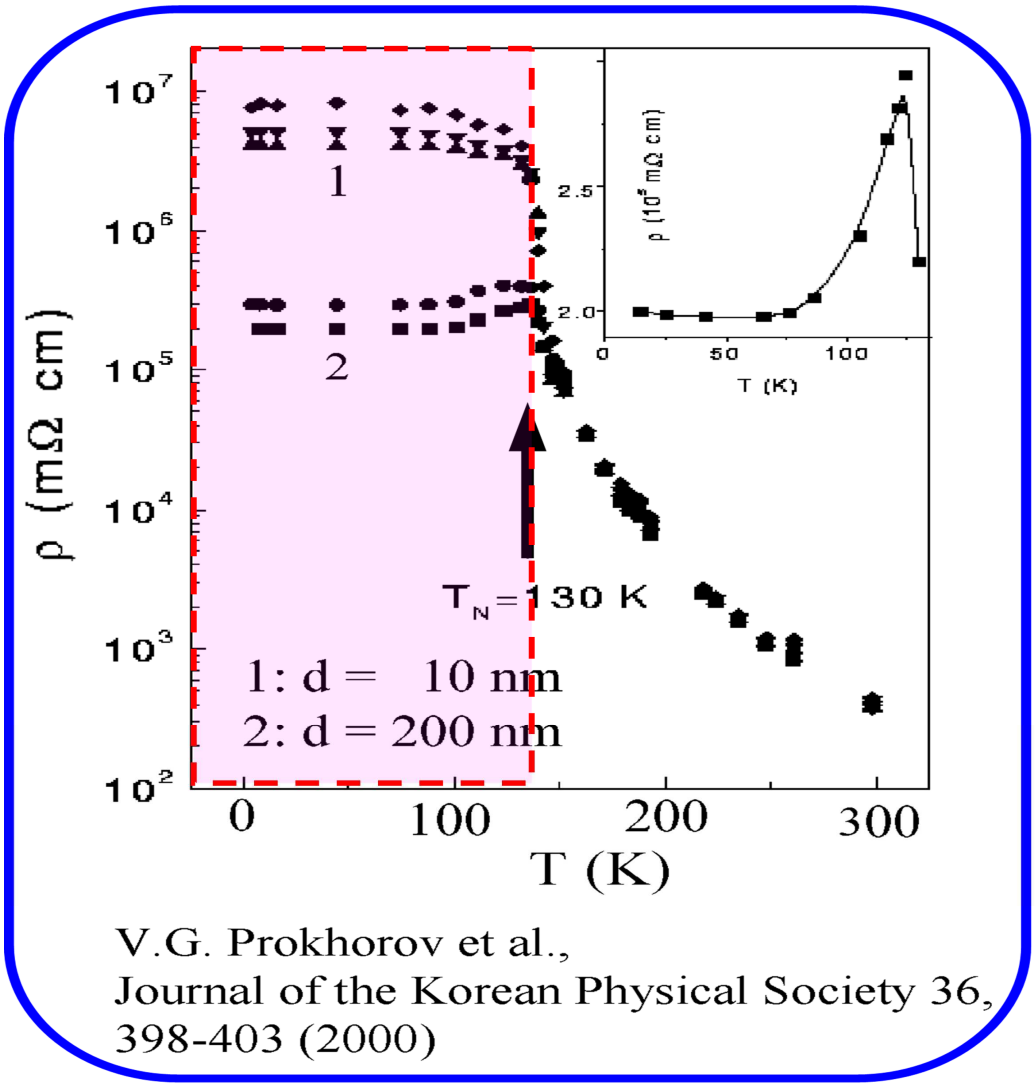

Figure 3.4: Temperature-variation of resistivity for PCMO films showing a drop in resistivity at 130K, the authors interpreted this drop (bending) in resistivity as an appearance of the metallic phase. Taken from [Refs. 114, 115].

After performing several tests (see appendix 2 for further details) in order to make a consensus that whether the system responds intrinsically or impedance is an issue, we decided to probe further the implications of our measurement procedure for the measured value of resistivity; the most important being the time delay between current application and voltage measurement.

3.5.1 Effect of time delay

In view of above context, we devised a test experiment hoping that if the system intrinsically has a temperature- and phase-transition-dependent response time feature, the

final result of the measurement might change with the delay. At the end of the day, indeed it does (see Fig. 3.5) (see Appendix 2).

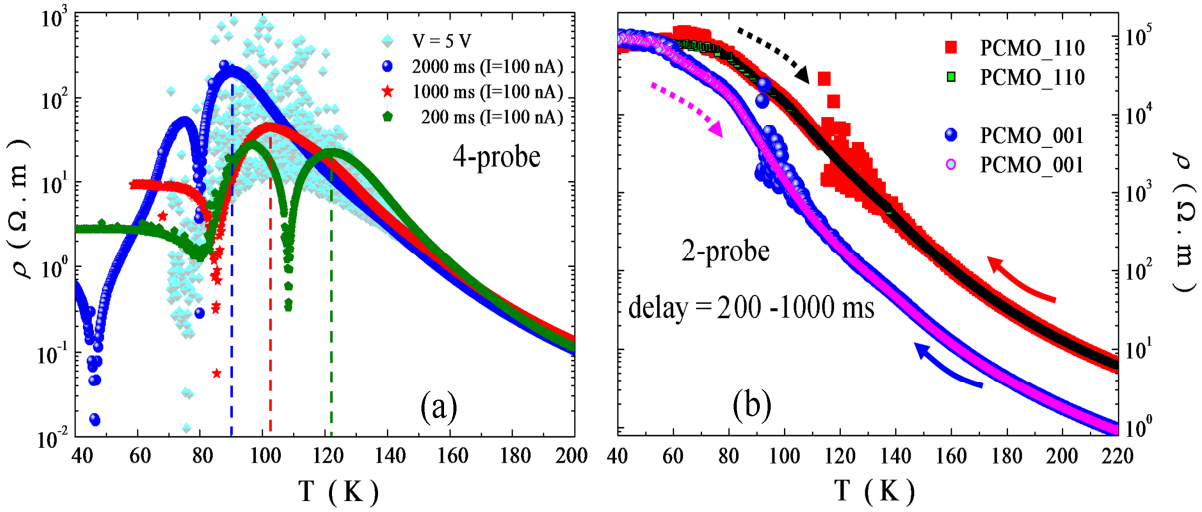

Figure 3.5: (a) Delay effect on the 4-probe resistivity of PCMO_001 (150 nm) thin film, and (b) comparison of delay effect on the 2-probe resistivity of PCMO_110 and PCMO_001 (150 nm) samples.

As an example, Fig. 3.5a shows 4-probe data for PCMO_001 (150 nm) sample. When we increased the delay between the application of current (in pulsed mode) and the voltage measurement to 0.2- 1s the features started to show suppression. This change was really remarkable; subsequent measurements performed on same sample (all other PCMO samples shown in Table 3.1 were also tested) demonstrated that the resistance was slowly smoothing with increase in delay time (e.g., at 6s, R(T) reached ~ 80K). The above experiment was a success as it has enabled us to go down in temperature window of the order of ~ 70K more (i.e., from 160K (before delay) - 90K (after delay)). In Fig. 3.5b another test experiment is shown which make a comparison of delay effect on the 2-probe resistivity of PCMO_110 and PCMO_001 (150 nm) samples. The following procedure was used for this short test experiment; the measurement was started with short delay time (200 ms) during cooling path (solid arrows) and after observing the start of noisy behavior the delay time was changed to loner value (1000 ms), interestingly measurement became smooth. The warming paths (broken arrows) were performed keeping the longer delay time, clearly, the noisy regimes were completely wiped out in this experiment.

In Fig. 3.6, a comparison of 2-probe and 4-probe resistivity data between PCMO_110 and PCMO_001 (both 150 nm) films, is shown (after delay modifications in measurements). Indeed, this data appear similar to what is reported in usual literature. These measurements

show qualitatively similar insulating behavior, with drop in resistance (4-probe), but there is no FM transition seen in contrast to dashed rectangular part shown in Fig. 3.4.

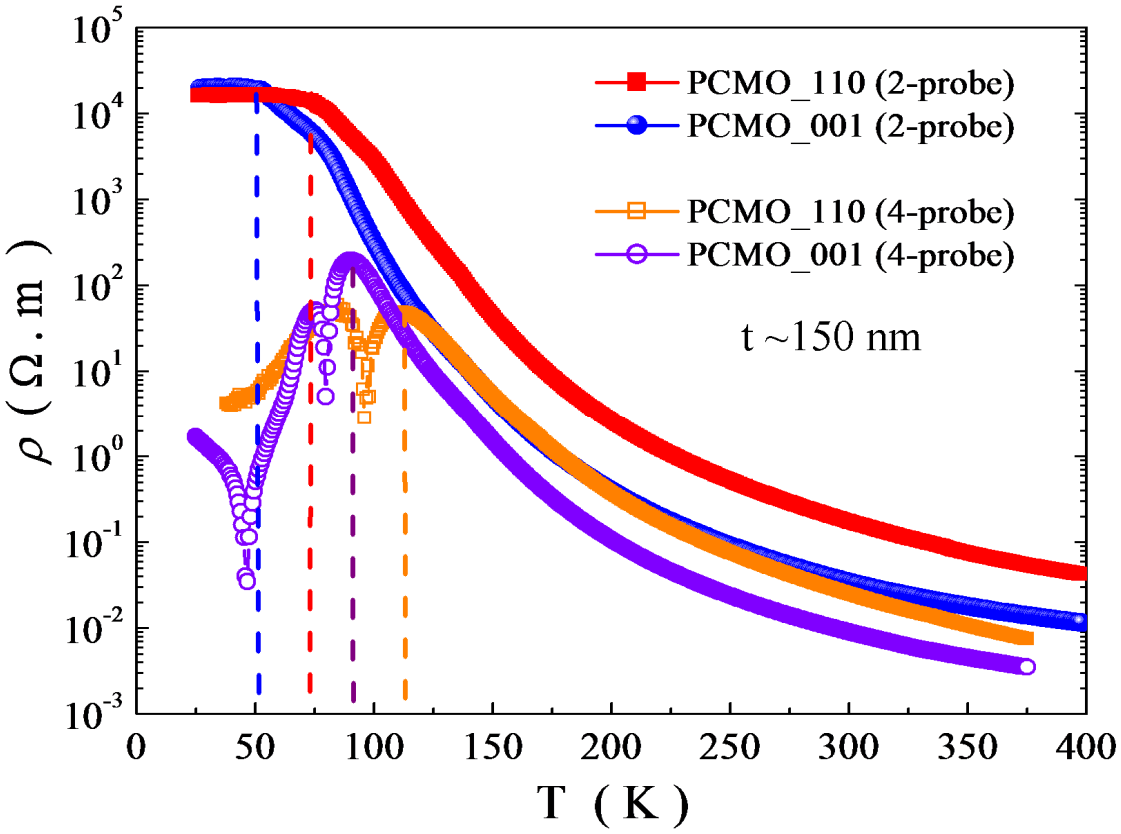

Figure 3.6: Comparison of 4-probe resistivity data between PCMO_110 and PCMO_001 (both 10 nm) thin films. Inset show 2-probe data for the same samples.

3.6 Results and discussion

As shown in Fig. 3.7a, the resistivity of PCMO reveals an activated semiconductor like character over the whole measured range (400K - 100K) for both samples. No evident feature is present at the expected charge ordering temperature as reported in bulk (T_{CO}= 230 *K*). Moreover, our experience on transport characterization and other studies in literature showed that [108], if the bias current is small (i.e., small electric field) then the two and four point measurement modes yield the same results for increasing and decreasing values of temperature.

In Fig. 3.7b, the logarithmic derivative of resistivity against T allows to highlight a change of slope due to charge ordering which is very feeble in Fig. 3.7a. The stress applied by the substrate, in principle, may set a difference between film and bulk properties.

However, in spite of the different structural details, PCMO_110 and PCMO_001 show a similar overall transport behavior.

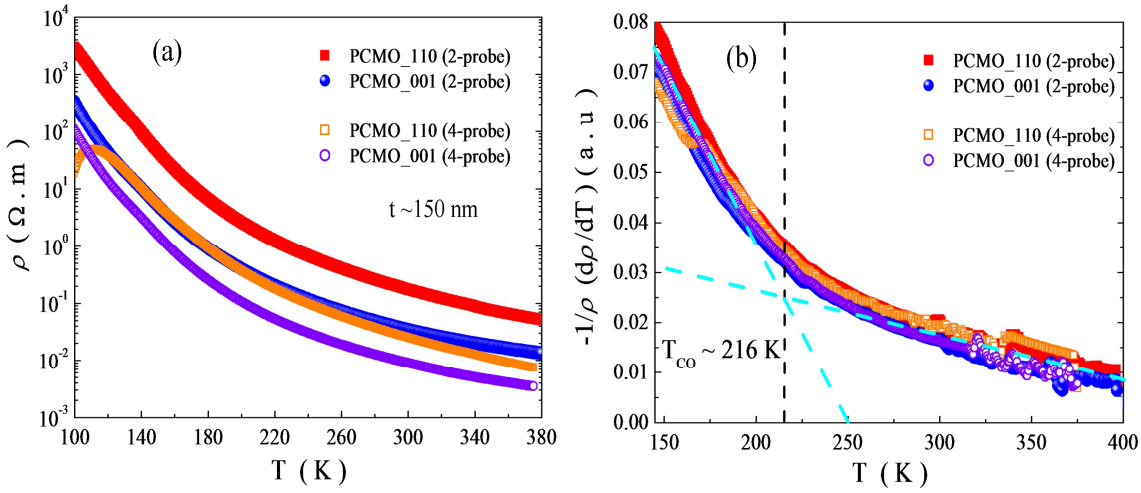

Figure 3.7: (a) Temperature dependence of resistivity for samples PCMO_110 and PCMO_001 showing insulating behavior with feeble traces of CO, (b) logarithmic derivative plot shows better signs of CO.

Additionally, in these samples the electric transport is characterized by an activated mechanism. Here the carriers are polarons, i.e., holes dressed by the interaction with the lattice, so that the activation mechanism enables the displacement of polarons from one site to the other. Meanwhile, the I-V characteristics show a slight nonlinearity (see Fig. 3.8).

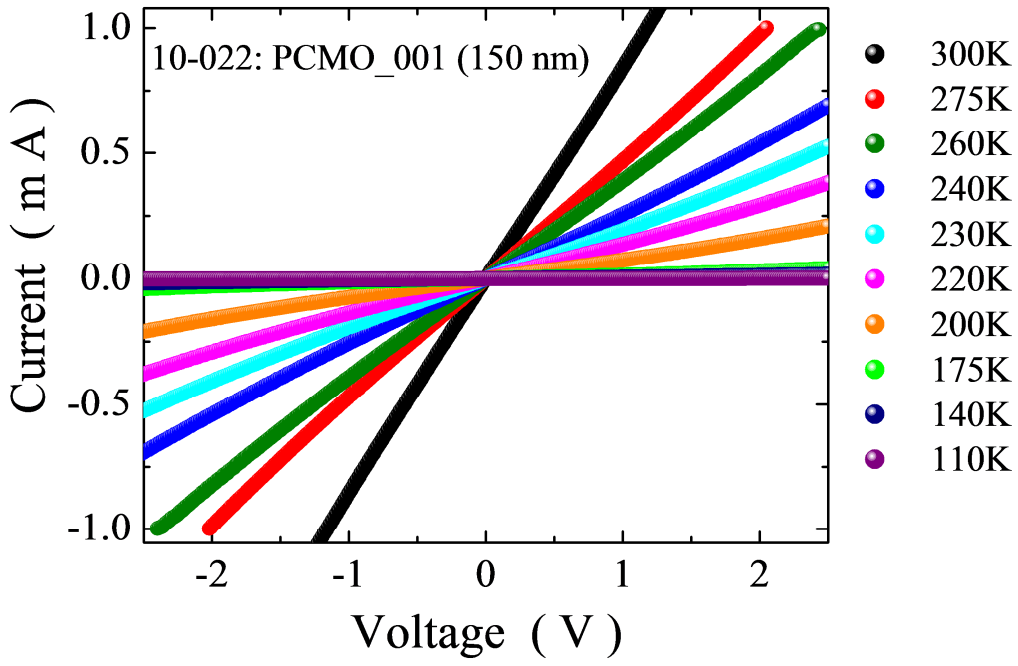

Figure 3.8: I vs. V curves for PCMO_001 (150 nm) sample at different temperatures.

Fig. 3.9 shows a plot of $\ln(\rho T^{-1})$ *versus* T^{-1} for the samples PCMO_110 and PCMO_001; in Fig. 3.9a data obtained by 2-probe and 4-probe methods is shown for a comparison. After analysing several samples (see Appendix 4) it was found that both configurations give qualitatively similar overall transport behavior as well as values of E_a. Therefore, I preferred to choose 2-probe data which is replotted in Fig. 3.9b. The dashed lines represent fits to Eq. 3.4, while vertical dashed lines are guide to the eyes showing fit-limit of the TAP model. These fits remarkably agree with the experimental data.

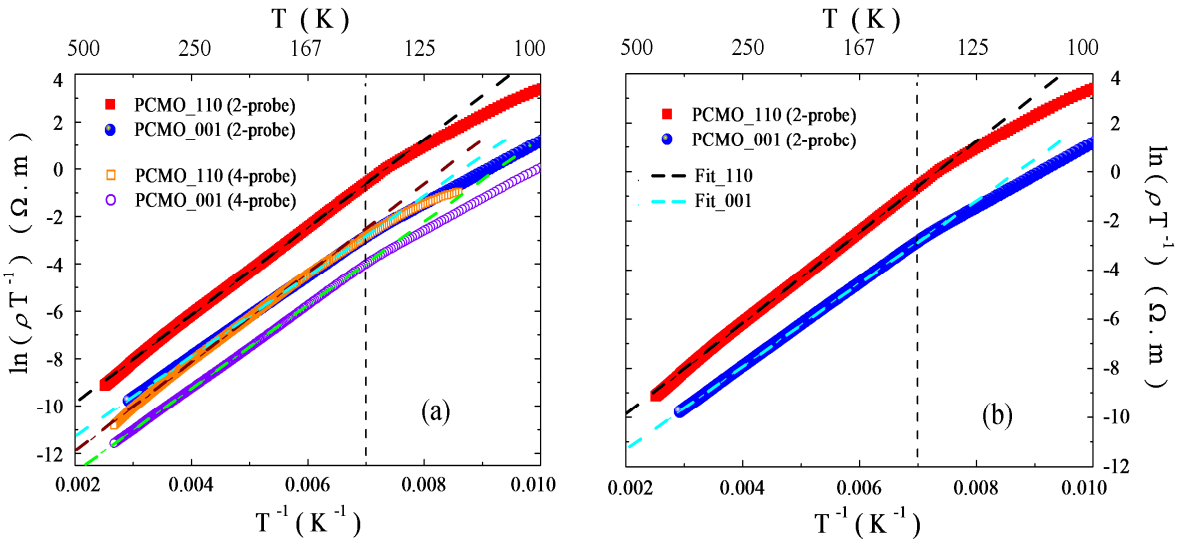

Figure 3.9: $\ln(\rho T^{-1})$ *Vs* T^{-1} for the samples PCMO_110 and PCMO_001, (a) data obtained by 2-probe and 4-probe methods, (b) same date replotted for 2-probe method. The dashed lines are the fitting to Eq. 3.4, while vertical dashed line is a guide to the eyes showing fit-limit of the TAP model down to 140K.

The E_a value obtained from the fitting of Eq. 3.4 for PCMO_110 sample was 161 meV, while for and PCMO_001 it was 147 meV, an overview is given in Table 3.2. These values are strongly in accordance with previous reports [108, 109].

Table 3.2: Ea values obtained by Eq. 3.4 and linear fitting (from slope) are shown for the two samples PCMO_110 and PCMO_001.

Sample name	Measurement mode	E_a [meV] (Eq. 3.4)	E_a [meV] (linear fit)
PCMO-110	2-probe	161	167
PCMO-110	4-probe	162	169
PCMO-001	2-probe	147	153
PCMO-001	4-probe	147	157

Let's now address the VRH model. According to reference [116], to identify the type of VRH conduction a usual practice is to plot $\ln(\rho T^{-1/2})$ *versus* $T^{-1/2}$ or $\ln(\rho)$ *versus* $T^{-1/4}$ to obtain a straight line. In Fig. 3.10, we plotted our data in the same way. However, from Fig. 3.10a and 3.10b it is clearly seen that the principal features are the same for both plots.

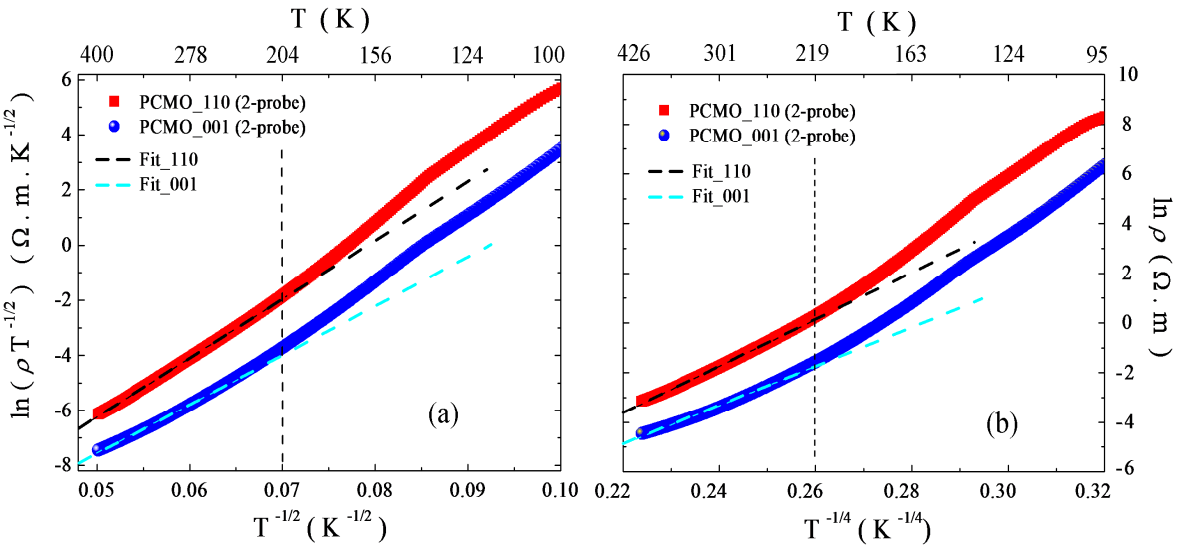

Figure 3.10: The resistivity data, for the two samples PCMO_110 and PCMO_001, versus (a) $T^{-1/2}$, and (b) $T^{-1/4}$. The dashed lines represent fits to a linear function, while vertical dashed line is a guide to the eyes showing fit-limit for VRH model down to ~ 210K from room temperature.

Furthermore, the fitting range is restricted to above 210K, clearly seen from the vertical dashed line that is a guide to the eyes. In this kind of situation an effective method for identification of the type of VRH hopping is to examine the local activation energy E_{loc} defined by,

$$E_{loc} = k_B \frac{d\ln(\rho)}{d(1/T)} \qquad (3.6)$$

Aheading a step forward, untill now Eq. 3.4 (TAP model) gave the best fitting as well as E_a values of our data on PCMO films as compared to other models like VRH and simple thermal activation model; I will take into account numerator of Eq. 3.6 and replace it by $\ln(\rho/T)$. Indeed, a similar formula can be found in Ref. [108] where the apparent activation energy Q deduced from the logarithmic derivative of the resistivity (i.e., Eq. 3.4) is used for the evaluation of narrow band manganite PCMO thin films. It is defined by,

$$Q = k_B \frac{d\ln(\rho/T)}{d(1/T)} \qquad (3.7)$$

Where K_B is the Boltzmann constant having value 8.6173×10^{-5} eV K^{-1}.

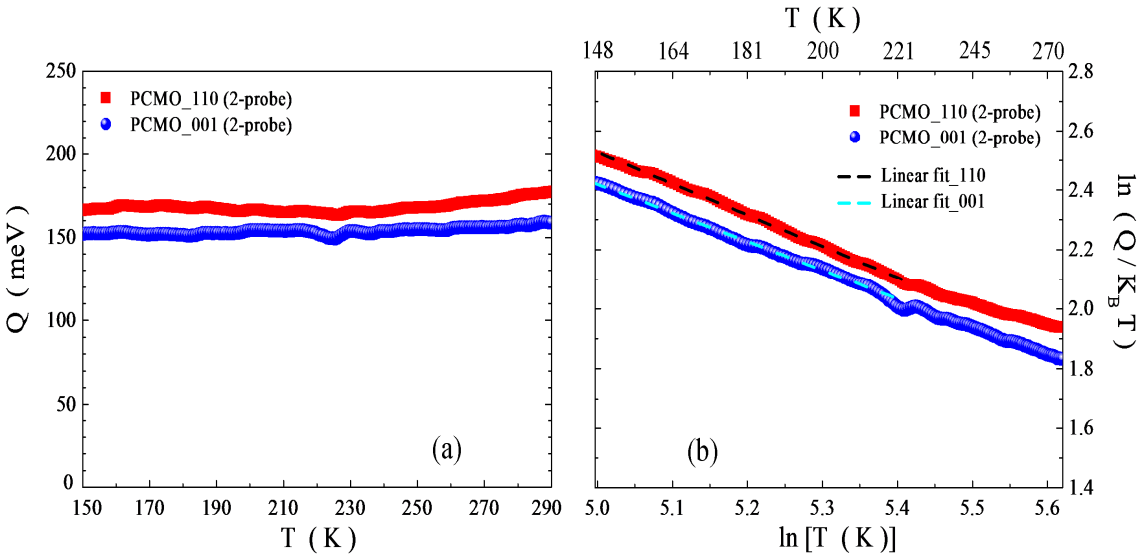

Figure 3.11: Temperature dependence of Q for the two samples PCMO_110 and PCMO_001, (a) calculated from Eq. 5, and (b) same date replotted in logarithmic form, shows a clear linear regime marked by dashed lines (linear fit) below T_{CO}, which correspond to the slope -1.

In Fig. 3.11a, I show the plot for Q against temperature. Recent studies on PCMO thin films [108] showed that, for small polaron hoping Q should equal the temperature-independent hopping energy E_a if the bias current is small. Interestingly, this is confirmed in our samples down to temperature of 150K (i.e. full valid range for hopping model, see Eq. 3.5) and the plot in Fig. 3.11a agrees very well with the E_a value obtained from fitting of Eq. 3.4 for PCMO_110 and PCMO_001 samples (i.e., 161meV and 147 meV respectively). Moreover, we do not see an anomaly in Q at the charge ordering (CO) temperature except feeble traces on PCMO_001 sample, this strengthens the TAP model. In order to get a further insight into the physical properties of PCMO, a further check regarding the type of hopping mechanism is the evaluation of a quantity ℓ defined in the references [103, 116] by,

$$\ell = \frac{\ln(Q/k_B T)}{\ln(T)} \qquad (3.8)$$

This ℓ is related to generalized form of activated-hopping in Eq. 3.1 by ℓ = - 1/n. The slope of the linear dependence of the $\ln(Q/K_B T)$ on ln (T) gives the value of ℓ. Indeed, this is

observed from Fig. 3.11b where the linear regime marked by dashed lines below CO temperature gives a slope of -1 for both characterized samples. Therefore, the data are clearly in favour of the TAP model in our PCMO thin films.

In summary for this section, the effect of substrate induced strains on the transport properties of PCMO films has been investigated. No evident feature is present at the expected charge ordering temperature as reported in bulk (T_{CO}= 230 *K*). In spite of the different structural details, PCMO_110 and PCMO_001 show a similar overall transport behavior and there is no FM metallic phase present in the R(T) data, the drop (bend) in resistance with 4-probes are false that can be removed by increase in delay time. Fits based on the VRH model were not satisfactory while TAP model fits nicely over a broad range of temperature from 400K to 150K. The observed experimental results suggest that, the thermally activated hopping (TAP) of small polarons model is more suitable for describing the temperature dependence of resistance for the PCMO thin films down to 150K than the VRH conductivity model.

3.6.1 Ferromagnetic insulating phase in PCMO

In this little sub-section, I will briefly discuss the epitaxial stabilization of the ferromagnetic phase and the concomitant suppression of the antiferromagnetic one in PCMO films grown on (110) STO, in contrast to the bulk-like features of samples grown onto (001) STO. In a very recent article by our group in Naples, Italy, A. Geddo Lehmann et al. [101], in an effort to acquire a homogeneous FM metallic state in PCMO, reported that it is indeed possible to destabilize the AFM component of PCMO and to stabilize a robust, nonbulklike and single phase ferromagnet, by growing pseudomorphic epitaxial films on a (110) cubic plane of the substrate STO.

3.6.1.1 Effect of biasing

Let us start with Fig. 3.12 taken from [Ref. 117], where the temperature variation of the resistance of a PCMO (x = 0.3) film deposited on Si (100) is shown for different values of the dc current. Here with increase in current the film showed an I–M transition in the low temperature range. The inset on left shows non-ohmic behavior in I–V curves, while right side inset shows a behavior similar to what we have observed in our thin films (see Fig. 3.6). Since the inset show data similar to our R(T) (i.e., drop in resistance), I decided to repeat this experiment, but again no metallic state was observed.

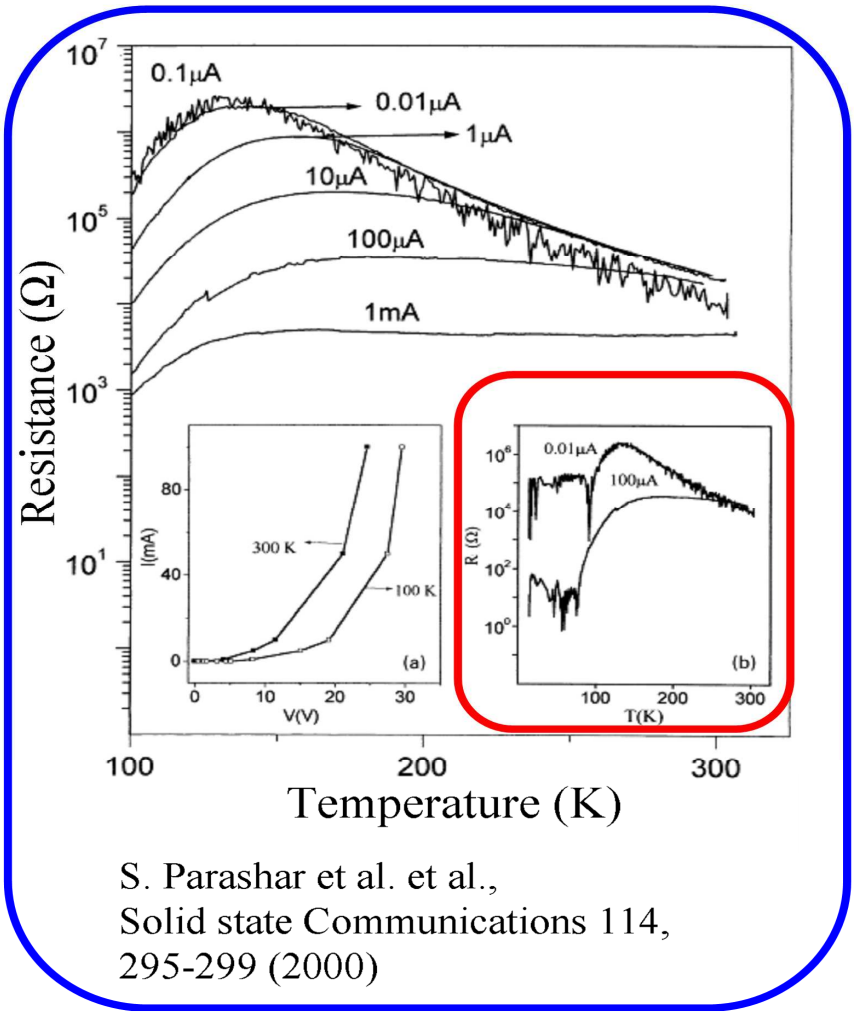

Figure 3.12: R (T) for PCMO sample showing a drop (bend) in resistance for different values of the current, inset shows similar behavior we observed. Taken from [Ref. 117].

In Fig. 3.13a, R (T) for different values of the current measured in 2-probe mode is shown for PCMO_110 sample. In Fig. 3.13b, ρ (T) for different values of current measured in 4-probe mode for another PCMO_110 sample is shown.

From Fig. 3.13, it appears that on increasing current I (or current density j), the charge localization process is weakened and progressively eliminated. As displayed in the R (T) curves at a temperature around 250 K, a slight difference in the resistance is seen already at low values of current (upto 1 μA) in PCMO_110 samples. The same current induced melting of the polarons, slightly below the charge ordering temperature, was reported in thick relaxed films of $Pr_{0.7}Ca_{0.3}MnO_3$ [108]. We observe, however, that in PCMO_110 (10 nm) the low resistance state is achieved under a very low current (current density) if compared with the one of thick sample or with the bulk.

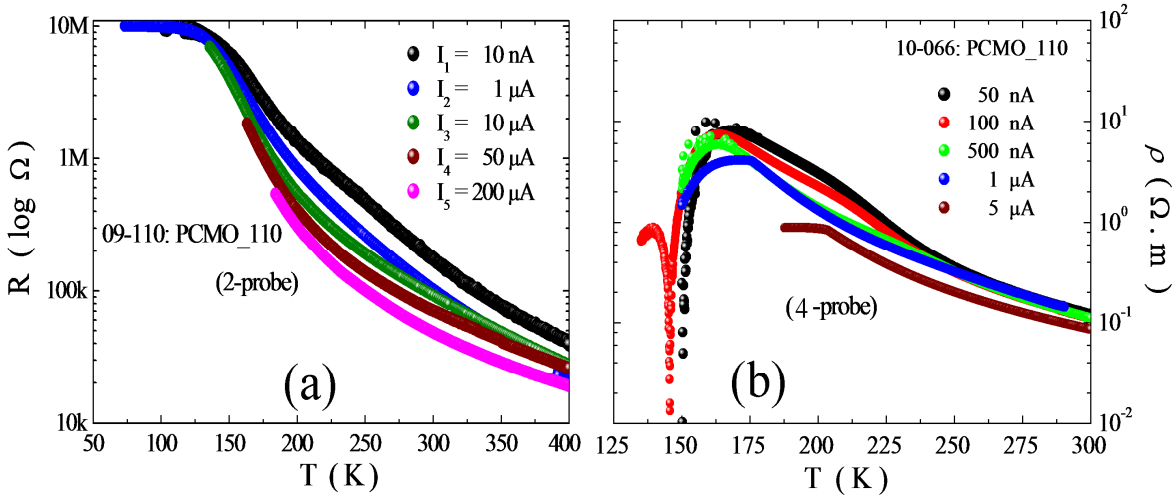

Figure 3.13: (a) R(T) for different values of the current measured in 2-probe mode, (b) Temperature-variation of resistivity for different values of current measured in 4-probe. Both films are on (110) STO substrate.

In Fig. 3.13, it appears that on increasing current I (or current density j), the charge localization process is weakened and progressively eliminated. As displayed in the R (T) curves at a temperature around 250 K, a slight difference in the resistance is seen already at low values of current (upto 1 µA) in PCMO_110 samples. The same current induced melting of the polarons, slightly below the charge ordering temperature, was reported in thick relaxed films of $Pr_{0.7}Ca_{0.3}MnO_3$ [108]. We observe, however, that in PCMO_110 (10 nm) the low resistance state is achieved under a very low current (current density) if compared with the one of thick sample or with the bulk (see Appendix 3).

In summary, we have shown that the robust, nonbulk like FM phase obtained by the pseudomorphic epitaxial deposition of PCMO on (110) STO (PCMO_110) under low electric field does not undergo a transition towards a metallic state. Therefore, as it happens in the bulk, the metallic DE phase remains hidden in PCMO_110 as well. We showed that, analogously to the bulk, the charge transport occurs in PCMO_110 through hopping of small polarons, the activation energy E_a of which depends on electric field and current density. We found that a low resistance state can be achieved slightly below T_{CO} under threshold values of electric current (current density) and electric field reduced with respect to the ones required in bulk massive samples or bulklike films. Our results suggest that the biaxial stress imposed by STO (110), though not sufficient to promote in PCMO a metallic ground state, however manages to weaken the electron-lattice interactions which compete in the bulk with double exchange.

3.7 Transport properties under light irradiation

In this section, I present the photoresponse of as-prepared hole-doped PCMO ultrathin films, emphasizing on photoresponse of PCMO_110 sample showing huge transient photoconductivity (TPC) and that the hidden insulator-metal transition is retrieved under light irradiation. The dependence of the photoconductivity on temperature, time and intensity will be described.

3.7.1 Background and motivation

As already stated, the peculiarity of the insulating state of PCMO is quite spectacular since it adjoins a hidden metallic state, characterized by enormous changes in resistivity, that can be reached by application of external stimuli (like, magnetic, electric, pressure, or radiation fields (x-rays or visible light)). Any of these perturbations drives the system to the conductive state, associated with the melting of the CO and OO state. Actually, light induced conductivity phenomena have attracted great interest after a report about photon exposure in the x-ray range on to a $Pr_{0.7}Ca_{0.3}MnO_3$ bulk crystal [9]. The effect was shown to be induced in the same compound also by infrared-to-visible photons. Miyano et al. [118], have reported an insulator to metal transition triggered by the photocarrier injection into the charge-ordered state of a thin slice of a $Pr_{0.7}Ca_{0.3}MnO_3$ single crystal. However in that case, the light excitation was a short pulse of 5 ns so no steady state or dc resistance was measured. Furthermore, most of the experiments were done in the IR range. Nonetheless, those findings triggered a variety of investigations on different manganites under various illumination conditions.

Recent reports by M. Rini et al. [119], demonstrated that resonant excitation of the Mn–O phonon vibration in $Pr_{0.7}Ca_{0.3}MnO_3$ single crystal drives the system on a femtosecond timescale into a metastable, nanosecond-lived, high conductivity phase at 30K. In another study, D. Polli and M. Rini et al. [120], reported femtosecond optical reflectivity measurements on $Pr_{0.7}Ca_{0.3}MnO_3$ single crystal at 77 K and 300K which resulted in a time dependent pathway towards metallic phase. A very recent article by H. Ichikawa et al. [10], about PLD grown epitaxial thin film of a charge and orbitally ordered $Nd_{0.5}Sr_{0.5}MnO_3$ (NSMO) on (011) STO (resembling our case of PCMO_110), reported the photoinduced change in the lattice structure using picosecond time-resolved X-ray diffraction emerging a ‘hidden insulating phase’ distinct from that found in the hitherto known phase diagram. The photoinduced state is structurally ordered, homogeneous, metastable and has crystallographic parameters different from any thermodynamically accessible state. Theoretically, systems

with competing degrees of freedom predict the formation of transient hidden phases that can be accessed by optical stimulation in the dynamical processes of photoinduced phase transitions (PIPTs) [12]. In this regard, strongly correlated TMO are promising in searching for PIPTs because they are likely to have hidden phases that are energetically almost degenerate but thermally inaccessible. Many studies have investigated PIPTs and related phenomena, including hidden phases. Furthermore, most of them used dynamic spectroscopic measurements to probe the local structural and electronic changes caused by transient states, and a complete picture in the form of R (T) is lacking in those reports.

Several types of phenomena and microscopic mechanisms are still under debate, however, until now there is no general understanding of the physical mechanisms which determine the photoresponse of manganites. In a more general framework, the present investigation may be considered as an attempt to add a tile to the wide mosaic of the physics of inhomogeneous states in manganites, the ground state of which is indeed, in a broad region of parameter space, a nanoscale mixture of phases, with unavoidable disorder at phase boundaries. In our view, $Pr_{0.7}Ca_{0.3}MnO_3$ shows up as a case study of the role of such disorders.

3.7.2 Experimental

3.7.2.1 Materials

In the following sections, we present the effect of light irradiation on the resistance of as-prepared hole-doped PCMO ultrathin films (10 nm thick) on (001) and (110) oriented $SrTiO_3$ substrates prepared by PLD. The main results presented here are obtained on, 10-066: PCMO_110 (10 nm) ultrathin sample. It is worth mentioning here that the PC experiments were performed also on other samples shown in Table 3.1. In addition, a test experiment was also carried out on different substrates (e.g., NGO, LAO, (001) STO and (110) STO) all having dimensions of 5 × 5 × 0.5 mm.

3.7.2.2 Methods

Briefly, the electrical resistance was measured in the temperature range of 300K to 10K in the standard four and two probe configurations. The light irradiation on the sample was provided by a standard mercury-argon Hg(A) lamp 6035 by Oriel Instruments, broadband spectrum (350 nm < λ < 700 nm), which illuminated the whole sample through an optical window of the closed cycle He-cryostat.

3.7.3 Results and discussion

In order to investigate the photoconductivity (PC) effect, the following procedure was adopted. The samples were carefully kept in dark, and a first transport characterization was performed. Then, they were exposed in a controlled and reproducible way to the UV radiation (by standard Hg (A) lamp) at 10K while performing a second run of measurements (cooling in dark and warming in UV radiation). Significant reduction of the resistance is only observed in the low temperature region, while high temperature region show no change under UV radiation. We stress that the effect of light irradiation is reversible.

In Fig. 3.14 temperature dependence of the sample resistance R (T) in dark and under illumination (maximum intensity) is compared for ultrathin PCMO_110 (10nm) sample, measured in the 2-probe mode (V = 5V). During cooling in dark, the resistance shows an insulating thermally activated behavior (no intrinsic I-M transition) down to 120K, and its transport properties are well described by TAP thermally activated hopping of small polarons model [109].

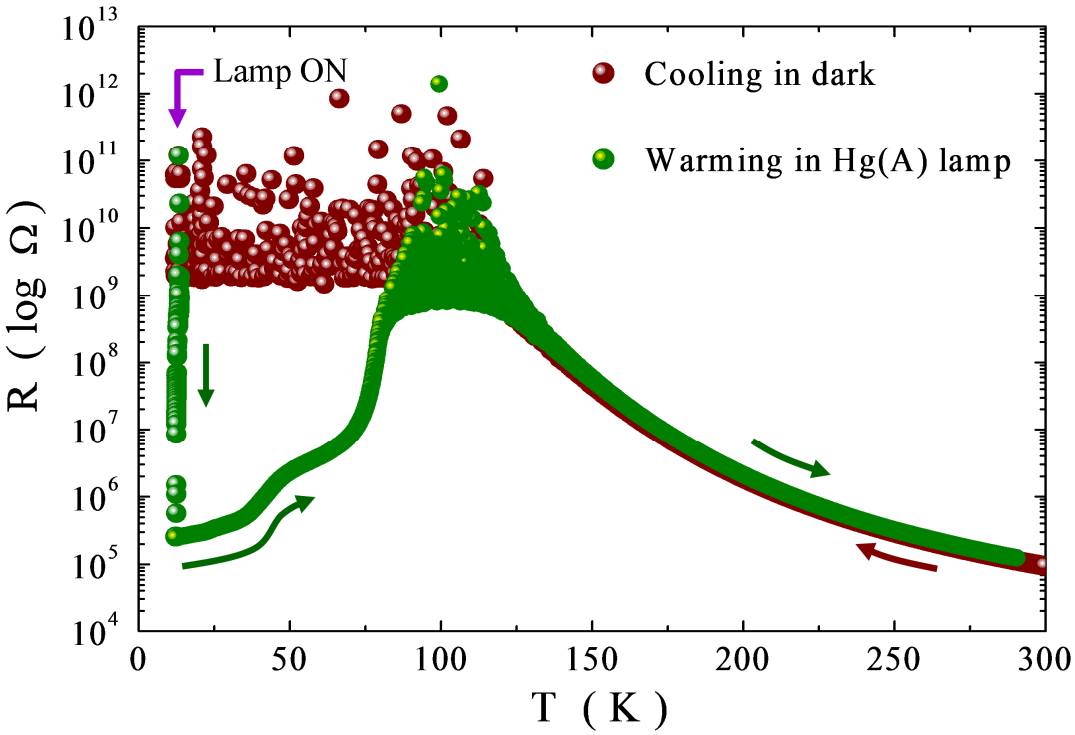

Figure 3.l4: Comparison of temperature dependence of the resistance in dark and under UV irradiation for PCMO_110 (10 nm) thin film. At 10K the sample was irradiated by UV radiation (standard Hg (A) lamp). The irradiation triggers ≈ 5 orders of magnitude drop in resistance as indicated by vertical arrow. The sample was then heated back to room temperature in photo-illumination. The resistance after illumination indicates a metallic regime between 10K and 100 K.

For T < 120 K, the sample resistance exceeds the input impedance of the nanovoltmeter (as shown by saturation of noisy behavior) the so called voltage limit (V-limit) of the measurement setup in use. At 10K, the sample was irradiated with Hg (A) lamp, and the resistance which was estimated at several hundreds of G ohms in darkness, falls down to several hundreds of K ohms under illumination. Hence, the sample resistance dropped by ≈ 7 orders of magnitude upon exposure to UV radiation. While the electrical state of the material after photo-irradiation is metallic as can be seen from the positive dR/dT of the resistance curve on warming the sample, the photo-induced metallic state is non persistent, i.e., after switching off the UV lamp resistance returns back to its original state. Exemplarily, the measurements were performed both in usual daylight and by covering the cryostat windows to achieve complete darkness inside the chamber where sample is placed. The resistance did not show any change in both cases, thus we strongly believe that daylight does not induce any nonpersistent photoconductivity in these narrowband manganite thin films.

Under illumination by an Hg (A) lamp, the resistivity does not change for T > 120K up to room temperature. Furthermore, in the invalid region i.e., 85K > T > 120K, the sample became extremely resistive that its exponential growth is truncated by the issue of V-limit. However, below 80 K, the resistivity decreases abruptly by several orders of magnitude showing a huge transient I-M transition which traces the same path during warming and cooling (it is reproducible).

Before moving further, I would like to stress here that D. Polli and M. Rini et al. [120], claimed a room temperature I to M transition under light irradiation, and described their findings in these words, “We now turn to the most provocative observation of our paper, that involving the dynamics of the phase change when initiated in the room-temperature phase. Above T_{CO} = 220 K, $Pr_{0.7}Ca_{0.3}MnO_3$ behaves as a small-polaron insulator with no longrange Jahn–Teller distortion. In this phase, no colossal negative magnetoresistive behaviour is observed. However, with photoexcitation we still observed the formation of a metallic state for approximately the same excitation fluence as that found at low temperatures. The observation of a photoinitiated metallic phase is quite remarkable, and it is indicative of the existence of a competing conducting phase all the way to room temperature. Presumably, colossal negative magnetoresistance does not occur because of the low energy scale of magnetic fields, whereas the ‘barrier’ between the two phases can be overcome with photo-excitation” [paragraph taken from Ref. 120].

In order to explore this metallic phase claimed in Ref. [120], I tried PIPT experiment on 07-102: PCMO_001 (50 nm) sample by selecting infra red (IR) and green wavelengths of

the pulsed laser (type: Q-switched (pulsed) Nd:YAG) with power~ 95 mJ/pulse at 1064 nm (IR) and 88 mJ/pulse pulse at 532 nm (green), having repetition rate of 0.1 Hz, respectively, from room temperature down to 150K, but we saw no sign of it. The outcome of this experiment resulted in no change in the resistance except very feeble traces of heating effects in this temperature window. Furthermore by performing above simple experiment with UV lamp it was possible to record resistance values at each and every temperature but still it was seen that the resistivity does not change for T > 120K up to room temperature. This confirms again that there is no I to M transition in this temperature range.

In order to further investigate the observed photoconductivity effect, as a function of the lamp intensity, R (T) data was acquired under UV exposure (during warming) with selected intensity values by using different bias currents from power supply of Hg (A) lamp. Fig. 3.15a shows a set of R (T) characteristics, obtained under UV lamp exposure at selected current bias values of 4 mA, 8 mA, 12 mA, 16 mA and 20 mA, respectively, which are linked to the intensity of the lamp.

For comparison, the R (T) curve without illumination (cooling in dark) has been replotted and the effect of photoillumination between 300K-10 K is shown in Fig. 3.15a. The resistance drops instantaneously upon exposure to lamp light. The drop is substantial, even the lowest intensity of the Lamp (4 mA), clearly, “turning on” the IMT. In addition, Fig. 3.15b shows that, this light induced transition has typical “peaks” (marked by arrows 1, 2 and 3) as already seen elsewhere [121] for other type of manganite (compound).

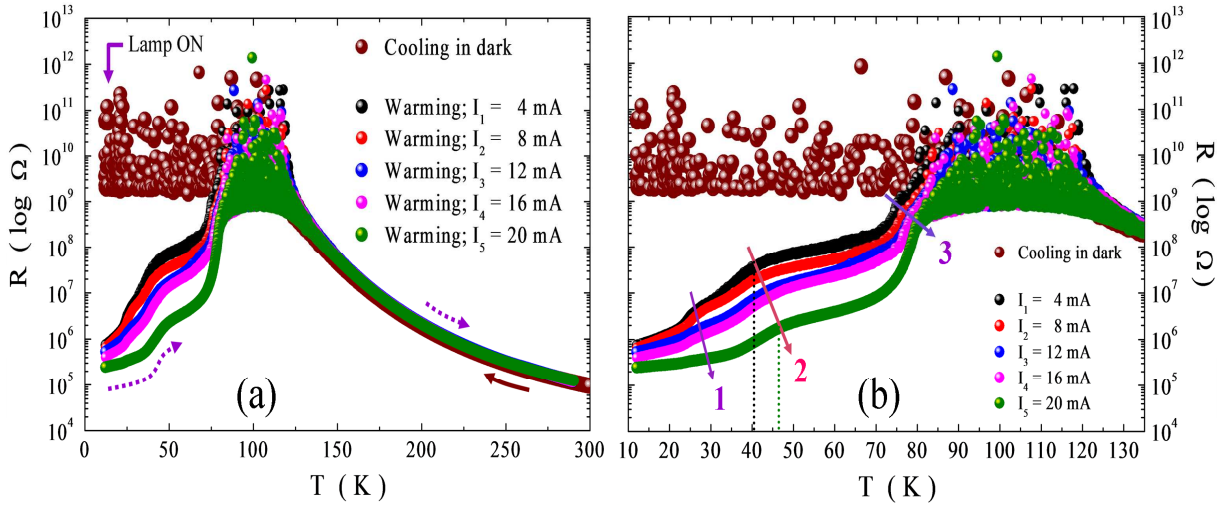

Figure 3.15: (a) Resistance versus temperature measured in darkness and under illumination with different lamp intensities for the PCMO_110 (10 nm) sample. (b) Low temperature zoom view of data shown in (a).

With increasing lamp intensity this effect becomes more pronounced in the sense that the effective peak temperatures shift towards right side (i.e., to higher temperature range). Starting from the left side of Fig. 3.15b, arrow-1 which specifies the location of first set of peaks shows a small increment in temperature from 25k to 29K, however the peaks seem to be suppressed as the intensity increased. Arrow-2 in the mid specifies the location of second set of peaks moving from 41K to 47K, that are pronounced as the intensity is increased, respectively. In addition, the photoinduced transient conductivity also shows a big increase in this temperature range. Finally, arrow-3 near to the V-limit shows a shift in temperature from 74K to 80K, with increasing intensity of the lamp.

In our view, the above behavior is attributed to the tensile strain imposed by (110) STO substrate in the film. We can not attribute this behaviour as an artefact due to the heating effects. To support our measurements, we emphasize the following reasons:

i) the I-M transition is induced by very low level (intensity) light irradiation,

ii) fixing the light intensity and decreasing the temperature results in a resistivity decrease, and

iii) resistivities almost equal to the room temperature resistivity can be obtained in this fashion.

Finally, above 120 K light has no effect on the resistivity, which rules out heating effects.

Fig. 3.16 shows the decrease of the resistance versus illumination time at 12K of the 10-066: PCMO_110 (10 nm) film. In this experiment the resistance was monitored as a function of time under isothermal conditions. The horizontal dashed line separates the figure in two parts; firstly, below this line measurements are fine and show typical temporal behavior of photoresistance. Secondly, the region above the dashed line is considered as invalid region (i.e., voltage limit in dark) because of immeasurable high resistance of the sample under investigation (additionally, compliance indicator of the electronic instruments show continuous blinking). Arrows indicates the switch ON and OFF moments of the Hg (A) lamp. The temporal behavior shows that, there is a sharp decrease of the resistance at the beginning of the illumination followed by a small decrease after a long time until a saturation value arises. The lamp turned ON between 0 - 300 s, and then again between 900 - 1200 s. This photoconductivity effect is non persistent since the resistance return back to original insulating state between 300 s and 900 s (~ long time). This TPC effect vanishes around $T \geq 120$ K.

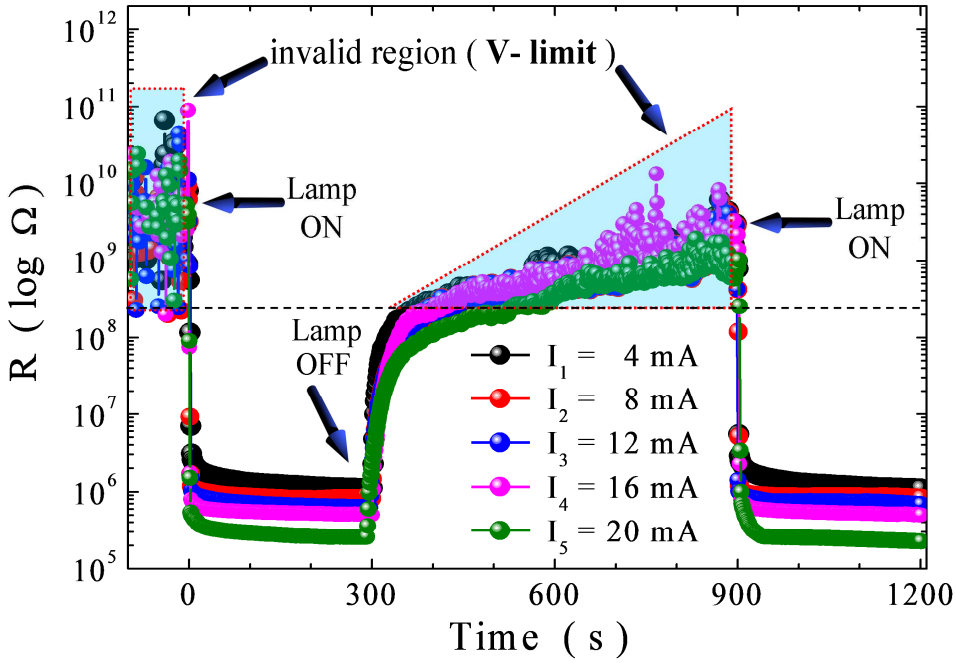

Figure 3.16: Resistance vs. time in dark and under light exposure for 10-066: PCMO_110 (10 nm) sample at 12K.

3.7.4 Substrate issue

An important issue concerning possible origin of the photoinduced resistance change is carrier injection from the substrate for films thinner than the absorption length of light. Thus not only the film but also the substrate is optically excited. Hence, the possible change in doping resulting from carrier injection from the substrate is an open point for most experiments on illuminated manganite films with a thickness of several 10 nm. To clarify possible origins of the photoconductivity the transport behaviour of bare STO substrates is also studied. The temperature-dependent resistance in dark and under illumination for a bare STO substrate subjected to temperature and vacuum conditions of growth is shown in Fig. 3.17, which was measured with the same photon flux and electrode configuration used for the film shown in Fig. 3.14. Moreover, from Fig. 3.17, it is seen that below 25K, STO resistance changes by only one order of magnitude while in this temperature range resistance of PCMO_110 sample falls down to several hundreds of K ohms under illumination (i.e., a drop by ≈ 5 orders of magnitude), which was estimated at several hundreds of G ohms in darkness. E. Beyreuther et al. have conducted a reference experiment on a bare substrate indicating that the photoconduction of bare $SrTiO_3$ is not similar to the observation for the thin-film sample [122].

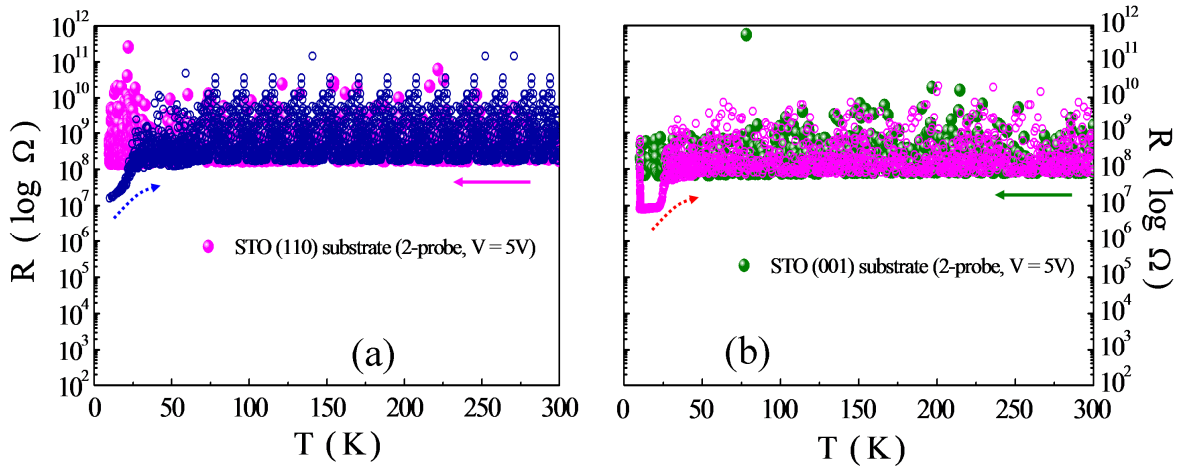

Figure 3.17: Temperature dependence of resistance measured in dark (solid arrows) and under illumination (dashed arrows) for, (a) STO (110) substrate and (b) STO (001) substrate. The measurements were done in 2-probe constant voltage (V= 5V) mode by resorting to ultrasonic bonding on silver (sputtered) contacts of 0.1 mm apart.

As a final comment, I present Fig. 3.18 which shows several PCMO_001 (10 nm) samples characterized under the same conditions as for PCMO_110 sample shown in Fig. 3.14. In spite of the fact that STO is the common substrate in each case, surprisingly all the samples on (001) STO have shown no PC effect. Therefore, it is hard to hypothesize that for PCMO_110 substrate is playing the crucial role, while for PCMO_001 does not. We believe that the biaxial tensile strain imposed by (110) orientation of the STO seems to play a role.

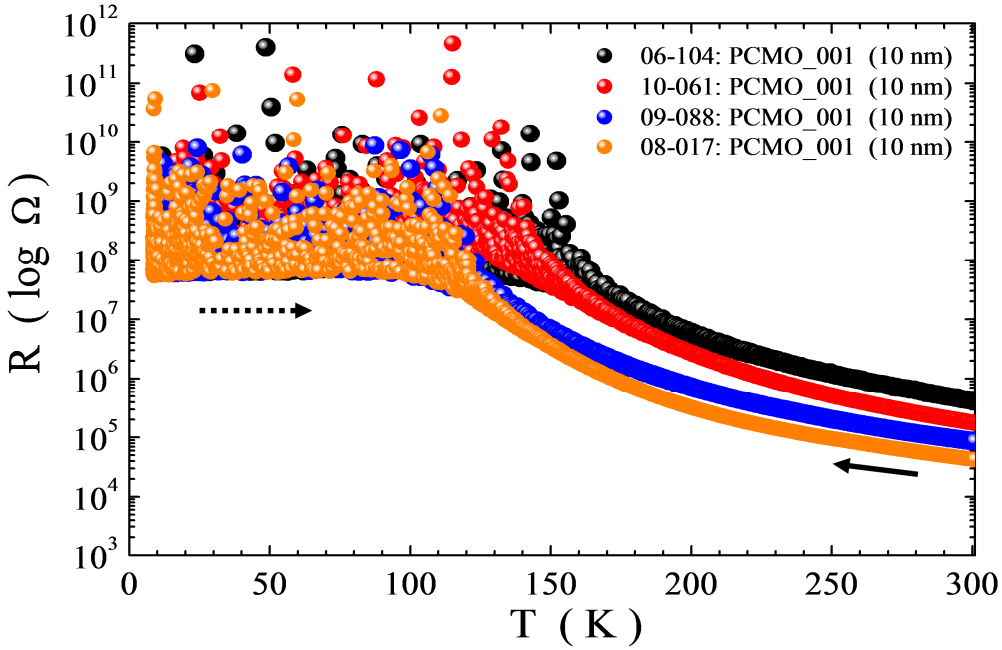

Figure 3.l8: R(T) data for several PCMO_001 samples in dark (solid arrow) and under illumination (dashed arrow), showing no signs of PC.

In summary, we have shown that UV light irradiation is an interesting tool which can change the doping of manganites with a gradual and reversible change of the carriers concentration using the same sample. Hence, irradiation is a good tool to explore the rich phase diagrams of manganites. UV Light may induce a transition to the hidden metallic phase in PCMO thin films which have no metallic state in the darkness. So, the manganite is rendered metallic by illumination but the effect is non persistent. Furthermore no PC effect is seen at room temperature. We showed that, while the ultrathin PCMO_110 (10-066: PCMO_110 (10 nm)) film is photoconductive and the insulator-metal transition which had been hidden in normal scenario is recovered under illumination, in contrast the PCMO_001 (10 nm) do not show this effect. This behavior cannot be associated to the bulk response of STO. We tested that an STO crystal remains insulating under identical irradiation conditions. This slightly opens up the possibility for the observation of a fascinating phenomenon, i.e., the photo- induction of ferromagnetic behavior by light, in FMI state of PCMO at low temperature. Our data show that it was possible to induce, only on samples grown on (110) oriented $SrTiO_3$ substrates, a colossal insulator to metal transition with a decrease of the low temperature resistance of about ten orders of magnitude. Our data clearly demonstrate that light affects the transport properties of PCMO only under the Curie temperature. Light allows therefore to undisclose the ferromagnetic metallic state, common to most manganites, but normally “hidden” in PCMO because of a competing ferromagnetic insulating state presumably related to charge and/or orbital ordering. The absence of any photoconductance effect above the Curie temperature of manganites shows that light effects should not be envisaged as simple photodoping but analysed in the framework of competing ground states in an intrinsically complex system. However, at present, the mechanism of the photo-induced metal-insulator transition is not clearly understood.

Chapter 4

Transport properties of transition metal oxide interfaces between oxide band insulators

4.1 Introduction

In this chapter the attention will be mainly concentrated on the comparison of the transport properties of high quality gallate-based and LAO/STO heterostructures, all hosting a two dimensional electron gas at the interface. The experimental results of transport characterization and the effects induced by UV light illumination will be discussed.

4.2 Polar catastrophe concept in polar/non-polar oxide interfaces

Untill now, a number of key features of this puzzling phenomenon have been well documented. Briefly, to name a few, LAO/STO heterostructures are conducting only if the interface shows a $(LaO)^{+}$ / $(TiO2)^{0}$ stacking provided the thickness of the LAO layer is at least 4 unit cells ($\geq$ 4 u.c), otherwise they are insulating. In addition, the charge carriers are found to be localized in an interfacial layer that is only few nanometers thick. The so-called "polar catastrophe" mechanism, a sudden *electronic reconstruction* taking place to compensate for the interfacial ionic polar discontinuity, is currently considered as a likely factor to explain this surprising interfacial conductivity between LAO/STO heterostructures. The wide band gap of LAO is considered as crucial in this approach, because it determines the capability of the polar film to transfer charges over the band gap of STO. Ideally, half an electron per areal unit cell is expected to be transferred at the TiO_2–LaO interface, partially filling the 3*d* Ti levels of the STO conduction band overlayer [123, 124].

4.2.1 New polar/non-polar oxide interfaces

The above approach seems to provide an appealing explanation for many important features has certainly some significance, but there are issues left unresolved [125] and, therefore, other mechanisms may contribute as well to the observed phenomenology. The

first scenario is envisaged to the creation of oxygen vacancies in the STO crystal (near the interface) used as substrate during pulsed laser deposition (PLD) [126, 127]. Actually, it is reported that the electrical transport properties of the heterostructure are affected both by oxygen pressure during PLD growth of the LAO overlayer (typically ~ 10^{-6}–10^{-3} mbar) [128, 129, 130, 131], and by the application of an oxygen postanneal [131]. Moreover, studies [e.g., see Ref. 129] demonstrated that at 10^{-6} mbar, a large number of dislocations and of oxygen vacancies are generated, which may be connected with the impact of high kinetic energy species with the substrate. Alternatively, this linked with the second possible scenario: if energetic La ions hit the STO surface, some cation intermixing (a substantial La substitution for Sr) may also take place, resulting in a chemical doping of the STO surface with potential effect on the 2DEG formation driving the insulating surface of the STO into a conductor [130, 132].

Aheading a step further, in this perspective, our group in Naples, Italy started the search of novel heterostructures based on different overlayers. On this basis, we identified $LaGaO_3$ (LGO) and $NdGaO_3$ (NGO) as two gallate based test materials both polar, wide band gap and pseudocubic perovskites respectively [133, 134]. Hence, the "internal" relaxation of the dipole field, by displacing electrons from negative to positive ions (i.e., from valence to conduction band), has a high energy cost. Actually, the electrostatic potential determines a band bending in STO. This is schematically represented in the Fig. 4.1 below.

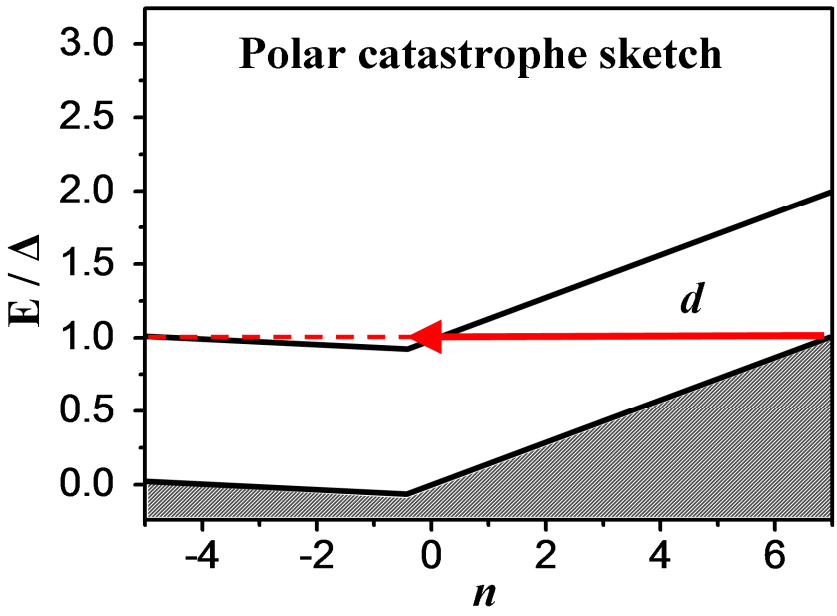

Figure 4.1: Polar catastrophe sketch

The dashed line delimits the VB of STO that is far from the interface. This energy level is equal to that of the free surface of LAO. The band bending determines a potential well at the interface. The band bending effect is related to the mechanism of charge injection, in the sense that the STO bands bend only after the critical thickness of LAO has been reached. Moreover, the depth and the width of the potential well are related to the value of the injected charge (σe) and so to the number of LAO layers.

4.3 Experimental

The samples chosen for this work are comprises of LAO, LGO and NGO films (12 unit cell thick) grown onto STO (001) substrates with TiO_2 plane termination, chemically treated in de-ionized water and buffered-HF [135]. A further comparison among all the structures is shown in Table 1 for clarification.

Table 4.1: A comparison of different characteristics observed among STO, LAO, LGO and NGO compunds [Tolerance factor *t*, taken from Ref. 136].

Characteristics	$SrTiO_3$ (STO)	$LaAlO_3$ (LAO)	$LaGaO_3$ (LGO)	$NdGaO_3$ (NGO)
Insulator type	band	band	band	band
Room temperature structure	cubic	pseudocubic	pseudocubic	pseudocubic
Room temperature space group	Pm $\bar{3}$ m	R3c	Pnmb	Pnmb
Pseudocubic lattice spacing, *a* [nm]	0.391	0.379	0.385	0.387
Energy gap [eV]	3.2	5.6	4.4	3.8
Dielectric constant, ε	277	23.5	25	20.2
r_A [nm]	0.118	0.103	0.103	0.098
r_B [nm]	0.061	0.054	0.062	0.062
r_O [nm]	0.140	0.140	0.140	0.140
t	0.908	0.886	0.851	0.833

All the samples used in this thesis work were fabricated in MODA laboratory, Naples, Italy. Fabrication parameters are same as described before. Briefly the substrate was positioned at a distance of about 30 mm from the target surface, and its temperature was fixed at 800 °C and different oxygen pressures within the 10^{-2}–10^{-4} mbar range were used (for recent studies see section 4.5.1). Furthermore, the samples were cooled to room temperature in the same oxygen pressure employed for the deposition. It is worth mentioning here that films of LAO on STO (001) presented regular RHEED oscillations typical of layer-by-layer growth and a final pattern reminiscent of a single crystal surface, whereas both LGO

and NGO films on STO (001) showed damped and less regular oscillations, and a streaky 2D pattern at the end of the growth (results not shown here) [133, 137]. The transport measurements were carried out by standard four-probe configuration (resembling van der Pauw) in standard Hall bar geometry, both in dark and under light irradiation. The sheet resistance vs. temperature (R_{sheet} (T)) was done in the current-pulsed mode, by biasing the samples with an active current source and the voltage across the sample was measured with a nano-voltmeter. The electrical contacts were obtained by resorting to ultrasonic bonding of Al wires on 5×5 mm samples. The benefit behind this technique is that the wire-bonding process itself cracks the surface and makes contact to the deeper layers. Further details on the growth mode, structure, electrical transport and optical properties of the above three types of structures– based interfaces are reported in the recent articles from our group in Naples, Italy [133, 134, 137, 138].

4.4 Results and discussion

4.4.1 Transport properties an overview

The oxides hetero-interface is usually elaborated by pulsed laser deposition (PLD) in an oxygen atmosphere, and it is generally considered that layer-by-layer growth and conductive interfaces occur only when the oxygen pressure is between 10^{-6} - 10^{-3} mbar. Unfortunately, such low pressures have two drawbacks. First, STO is doped by oxygen vacancies, which act as donors. Even though post annealing treatments decreases the amount of such vacancies in STO, doubts remain that the conductivity of the interface is due to local oxygen deficiency. Second, at low pressure the kinetic energy of cations in the ablation plume is higher. As stated in chapter 1, it was then argued that some cation intermixing at the interface may take place due to La subplantation. However, a recent study indicates that the relevance of such a mechanism is considerably reduced at an oxygen pressure of 5×10^{-2} mbar [139]. As a consequence, oxygen vacancies and interface disorder can be drastically reduced by an oxygen pressure increase during deposition.

Therefore, it is motivating to investigate if high quality, conducting oxide hetero-interfaces can be deposited at still higher oxygen pressure. Our group in Naples has recently shown that two-dimensional (2D) growth of LAO and LGO on STO can be achieved by PLD at 10^{-1} mbar [140]. Here, I report a novel result (first time reported) from our group [141] on conducting interfaces made up of 12 uc thick LGO/STO and LAO/STO samples grown at an oxygen pressure of $\approx10^{-1}$ mbar, and the results of R_{Sheet} (T) are shown in Fig. 4.2.

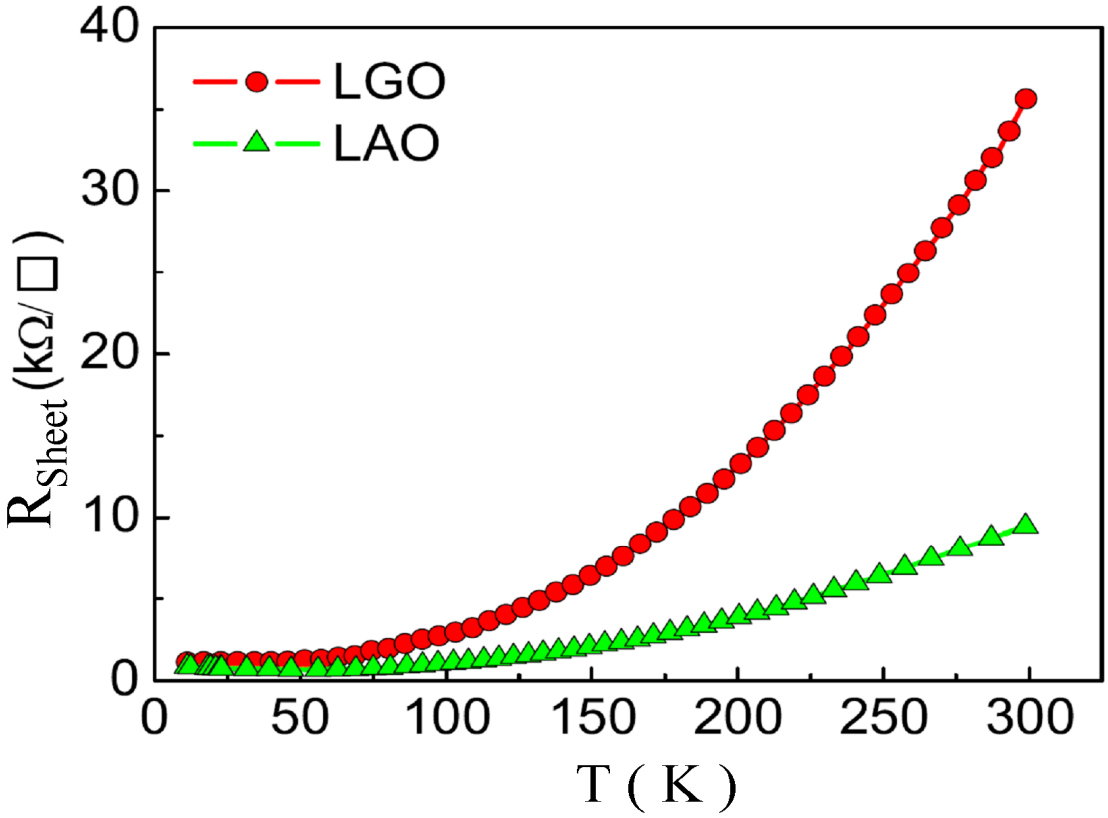

Figure 4.2: R_{Sheet} (T) of LGO/STO and LAO/STO interfaces grown at oxygen pressure of 10^{-1} mbar.

The samples exhibit a clear metallic conducting behaviour in both cases and the values of the resistance are similar to those obtained at low pressure (see Fig. 4.3). At such a high oxygen pressure, one can consider that the contributions of

(i) oxygen vacancies STO doping,

(ii) oxygen diffusion from STO to the growing film [142] and redox reactions on the surface of STO, recently suggested [143], are minor.

From now onwards, I will report my experimental results only on those samples which were prepared at oxygen pressure of 10^{-3} mbar.

4.4.2 Transport characterizations of buried interfaces

The motivation behind this experimental work was, indeed, to explore novel heterostructures based on different overlayers, and in this context two gallate based polar perovskites were chosen. First we created epitaxial films of both LGO and NGO on STO to reproduce the known behavior of these polar perovskites just like the case for LAO/STO. For the R_{sheet} (T) the samples were kept in dark for 24 h before the measurement, and a first transport characterization was performed. In Fig. 4.3, the transport measurements of R_{sheet} (T)

(in dark), of all the characterized interfaces are shown and they are compared with each other. The R_{sheet} (T) curves of NGO/STO and LGO/STO are qualitatively similar to that of LAO/STO. Room temperature resistance values are often in the range of 5-15 kΩ s for LAO/STO and LGO/STO samples with a thickness in the range 4–12 u.c, while NGO/STO generally shows sheet resistance slightly higher than LGO/STO. In all the three cases there is a clear metallic behavior in a wide range of temperature; a slight upturn (resistance minima) is sometimes observed at low temperature (Fig.4.2 and Fig. 4.3b). Moreover, LGO/STO is characterized by a lower residual resistivity among the others. Measurements verify that all the three structures have metallic interfaces.

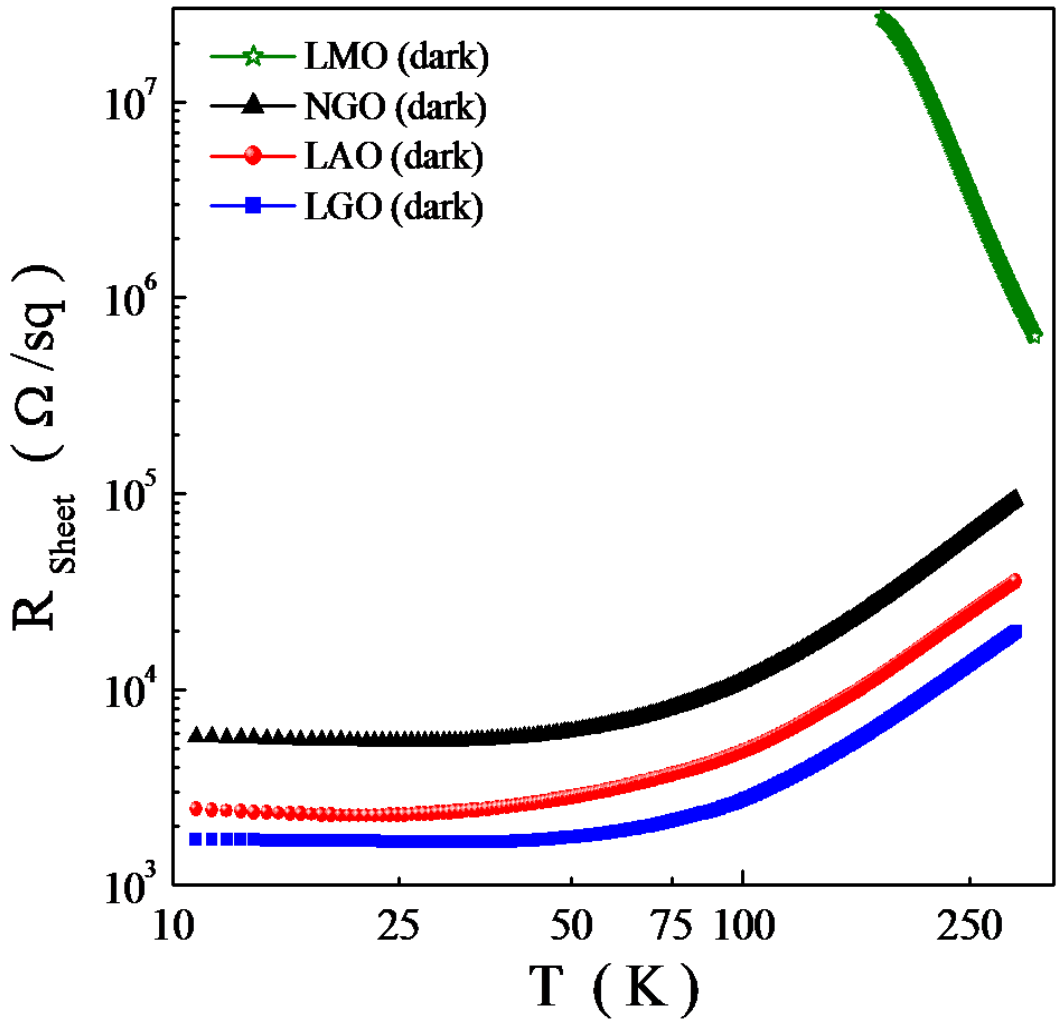

Figure 4.3: The sheet resistance vs temperature of 12 u.c. LAO, LGO, NGO and LMO based interfaces grown at the similar conditions on STO (001).

Before moving onto the other results, I would like to highlight the metallic nature of 2DEG in the framework of the present debate about the origin of interface conductivity in oxides. Therefore, I present and compare in Fig. 4.2, R_{sheet} (T) for a $LaMnO_3$ (LMO) sample (12 u.c. thick) grown over STO (001) with TiO_2 plane termination at the same deposition condition of NGO, LGO and LAO. This LMO sample showed an insulating behavior, with an immeasurable high resistance value below 170 K, which we attribute to the intrinsic resistivity of LMO. This result revealed, at least, that having a La-based, polar perovskite grown on Ti terminated STO is not a sufficient condition for the 2DEG formation.

4.4.3 Hysteretic effects

At this point, I would like to shed some light on an interesting hysteretic effect observed routinely in our heterostructures as described in Fig. 4.4.

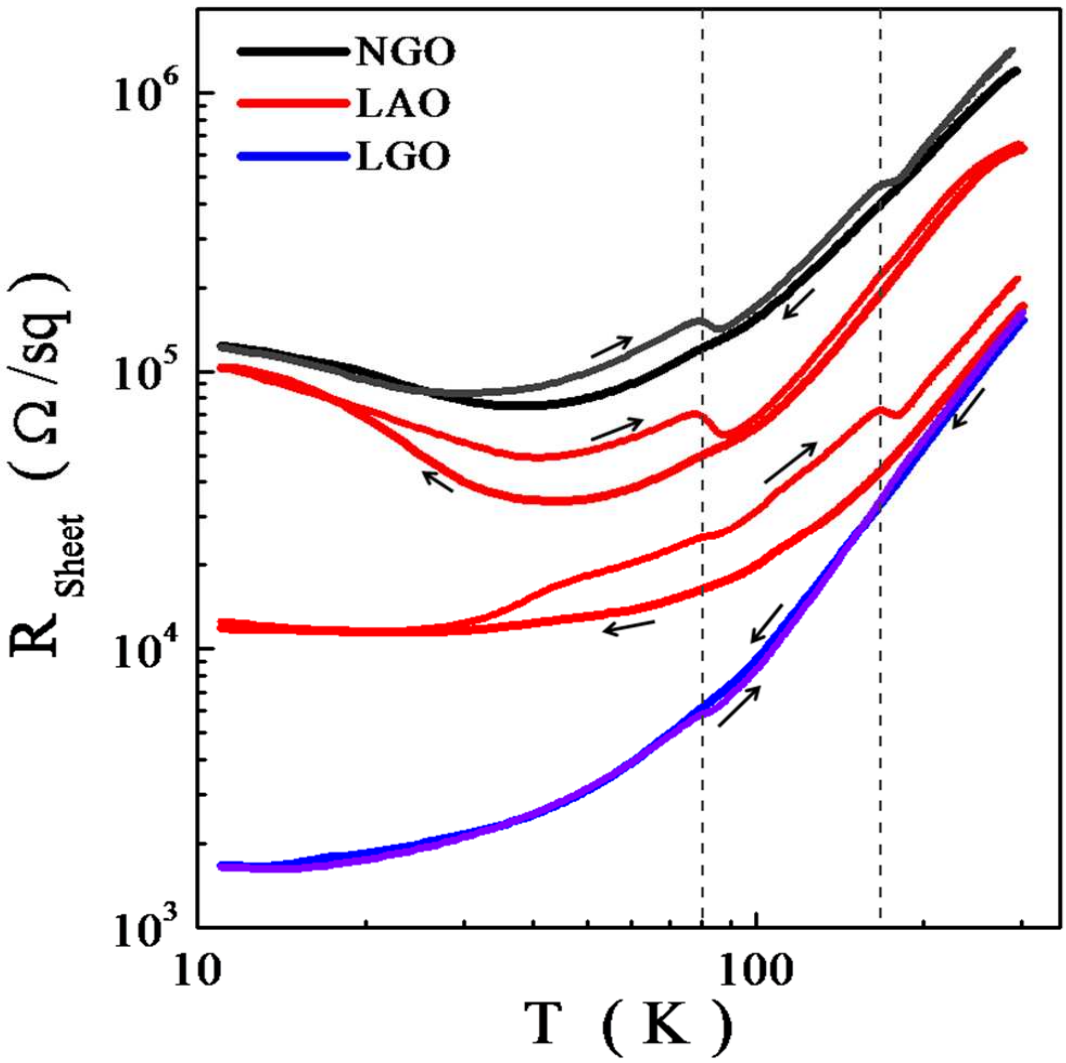

Figure 4.4: (a) Extra features show up in the R_{Sheet} (T) during warm up than during cool down. These peaks have been observed in multiple samples and always occur at the same temperatures.

Indeed, we observe pronounced hysteretic effects between cooling and warming in all three kinds of structures (irrespective of the thickness) whenever they have the upturns at low temperatures (resistance minima). In addition, it is usually accompanied by two peaks (maxima) but sometimes only one is realized at lower temperatures. These features consistently appear at the same temperature, but only during warm-up. As a function of polar layer thickness (with 4 u.c., and 20 u.c.) we observe the same qualitative behavior as for the case of 12 u.c. sample. Based on the characterization of dozens of samples (see Appendix 4), a clear correlation between increased RT samples resistance, increased step size and low temperature upturns is found.

A survey of the recent literature [144, 145] tells only minor details about these features appearing in the transport data. Interesting information is deduced from the reports of W. Siemons et al. [144, 145], who have seen these features in their samples with high sheet resistance (which they attribute to thickness and presumably to dielectric relaxations) and low carrier densities. Additionally, they are magnetic field dependent, and during warm-up stopping at the maximum of one of these features the resistance returns to the value measured during cooling over the course of hours. The peaks appear at 80K and 168K in our samples.

In order to better define the above temperatures and show they are all the same, I display in Figure 4.5 the hysteresis effect observed for a set of multiple samples along with their corresponding double derivative test (d^2R_{Sheet}/dT^2) to find point of inflection (inset shows the basic concept of this test). In Fig. 4.5a, two NGO samples are showing hysteretic effect and to find where exactly these curves start to bend I plotted the double derivative of same data in Fig. 4.5b. Similar behavior is also seen with multiple samples of LAO (Fig, 4.5c and d) and LGO (Fig, 4.5e and f). From this analysis, we observe two points of inflections, one around 82K and the other at 172K in all the three structures. Hence these values are the same as stated above, which confirms the uniqueness of these temperatures values.

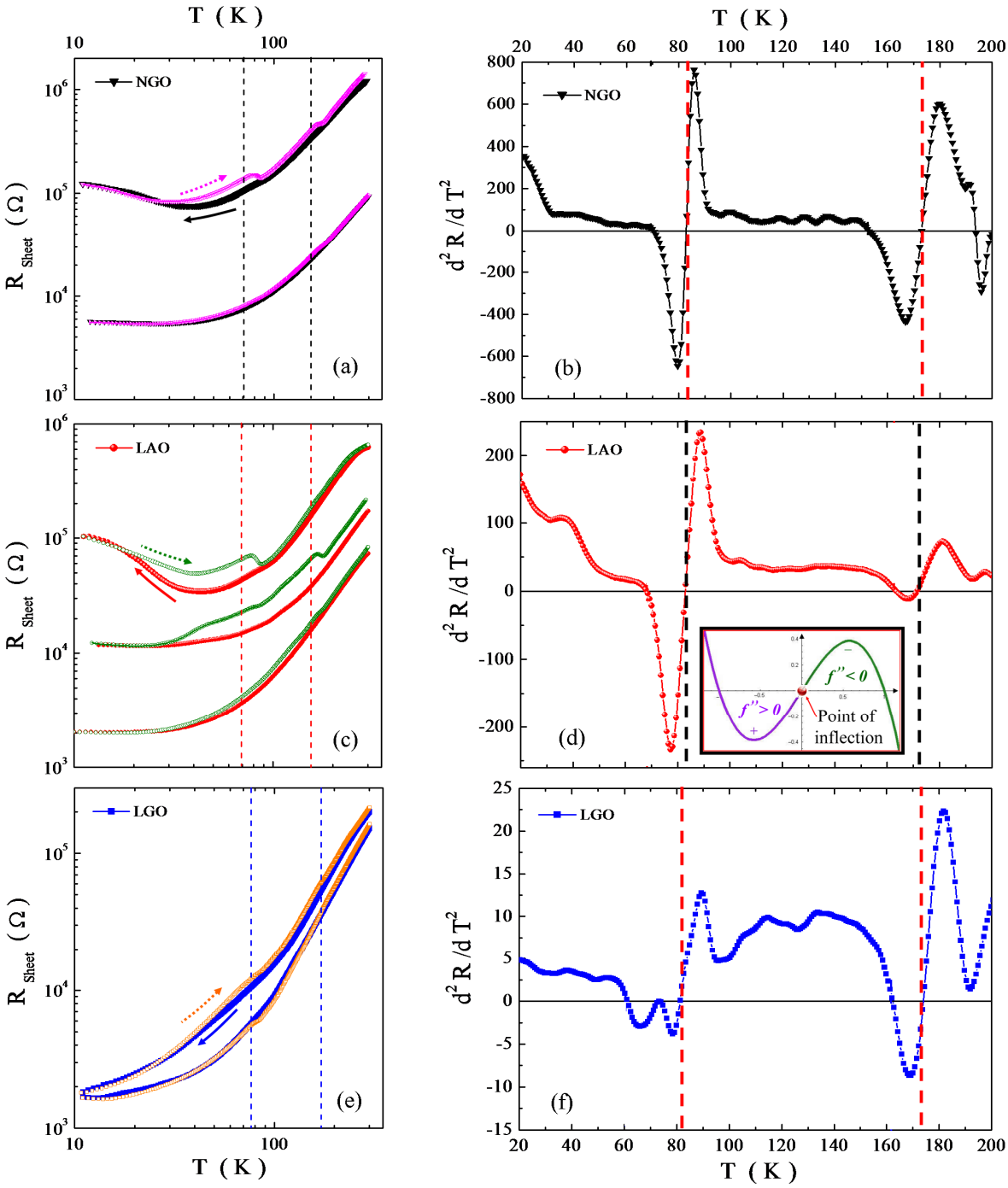

Figure 4.5: Hysteresis effect shown for multiple samples along with their corresponding double derivative test (d^2R_{Sheet}/dT^2) to find point of inflection in; ((a)-(b)) two NGO samples, ((c)-(d)) three LAO samples, and ((e)-(f)) two LGO samples.

4.5 Photoconductivity experiments

In order to further investigate the transport behavior in these structures, I have characterized them under light irradiation. In all three kinds of heterostructure significant decrease of the sheet resistance was observed even at room temperature. In this section, experimental results on transport properties of TMO interfaces characterized under light irradiation are shown and discussed.

4.5.1 Effect of UV irradiation

The following procedure was adopted to determine photoconductivity (PC) measurement in our samples. The samples were kept in dark for some days, and a first transport characterization was performed. During the second run of measurements the samples were exposed to the UV radiation, provided by a standard Hg (A) lamp. NGO is more subject to degradation (e.g., thermal cycling or aging) when compared with LAO or LGO, hence, high quality growth for NGO finds some difficulty. In view of our experience, this is due to a higher sensitivity to the substrate-surface perfection. As a consequence, NGO/STO with high R_{sheet} and semiconducting behaviour is occasionally obtained. A comparison between sheet resistances of these gallate-based interfaces in dark and under UV radiation with LAO/STO is shown in Fig. 4.6, where only cooling curves are displayed.

On the basis of my experience on transport characterization of these interfaces (see Appendix 4), I prefer to present experimental results in two sets of samples, (i) low R_{sheet} ($\leq 10^5$ Ω/sq at RT) samples as shown in Fig. 4.6a, and (ii) high R_{sheet} ($\geq 10^5$ Ω/sq at RT) samples as in Fig. 4.6b. The bold symbols represent measurements in dark, while open symbols stand for measurement under continuous UV illumination. By comparing set (i) and set (ii) in Fig. 4.6, I draw following findings. On average, NGO take up the highest R_{sheet} and LGO holds the lowest R_{sheet}, while LAO has intermediate R_{sheet} values. Additionally, Photoconductivity (PC) is more prominent in high R_{sheet} samples (Fig. 4.6b) than low R_{sheet} samples (Fig. 4.6a). Moreover, it is seen that a significant reduction of the resistance under light is observed in the low temperature region, where the increment of conductivity suppresses the resistance upturn (resistance minima). This strong temperature dependency of the PC is already a hint that the origin of the effect is not a simple increase in charge carriers but rather complex.

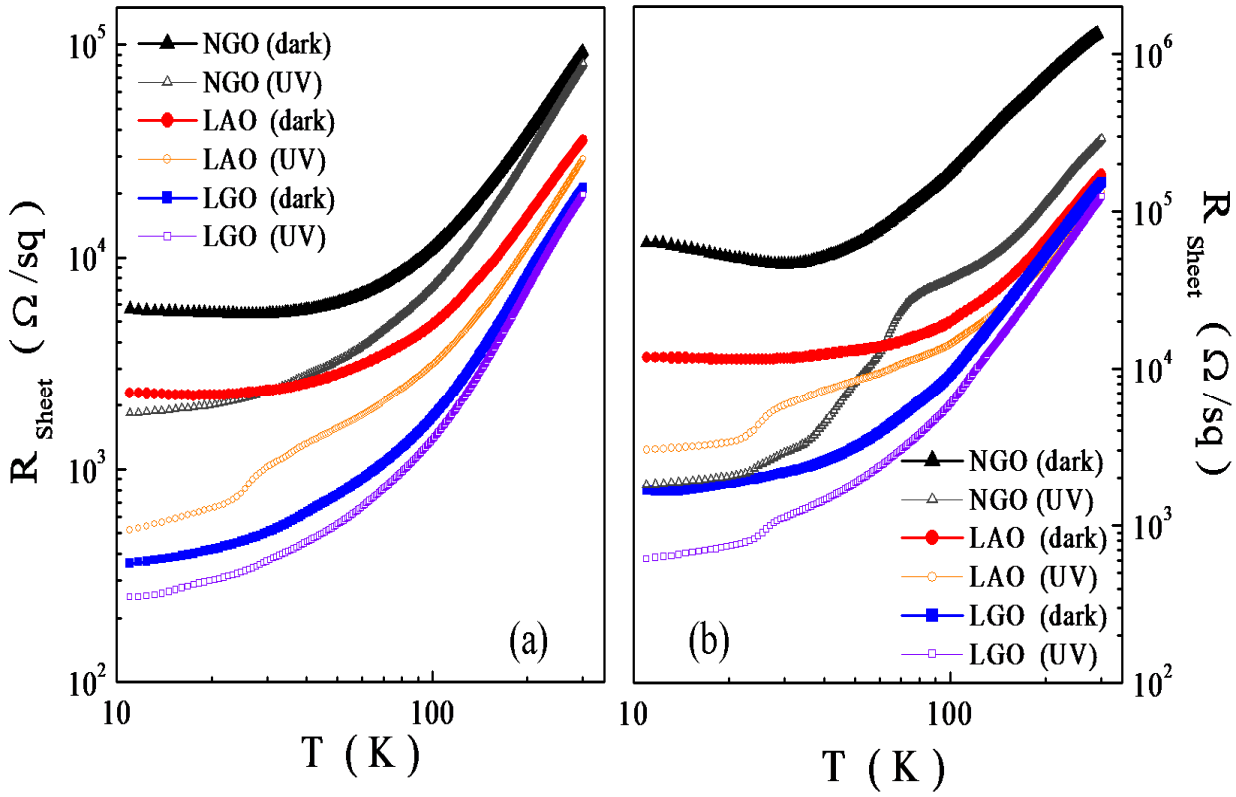

Figure 4.6: Sheet resistance vs temperature under UV irradiation of, (a) set (i) low resistance samples in dark NGO/STO (solid black triangle), LAO/STO (solid red circle) and LGO/STO (solid blue square), effect of UV irradiation is also clear (open symbols), (b) similar behavior with set (ii) higher resistance samples, which show bigger drop in resistance under light irradiation.

4.5.2 Time evolution of photo resistance

In order to further explore the properties of the PC effect in these heterostructure, I performed a study on the measurement of time dependence. PC is clearly observed at room temperature for all the three structures, however, it relies very much on the intrinsic nature of the sample's resistance. As stated before (see Fig. 4.6), the effect of UV irradiation is strong for highly resistive samples when compared with low resistive ones. In this view, a comparison of time dependence of photoresponse for gallate based interfaces is shown in Fig. 4.7a. For this part, two NGO/STO samples (S_1) and (S_2) both having different R_{Sheet} values were chosen, together with one LGO/STO sample (S_3) having low resistance value at room temperature (298K), respectively. The arrows show the ON and OFF moments for the UV irradiation. In addition, it can be seen that they all show clear long-term relaxations which are more elongated when the sample has higher resistance values.

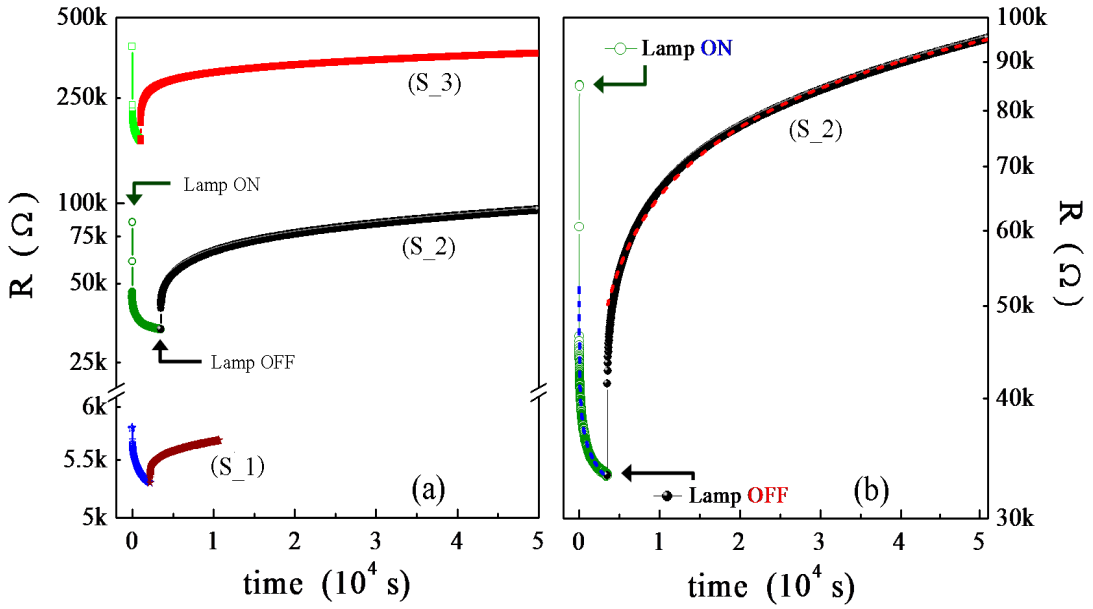

Figure 4.7: Comparison of; (a) time dependence of photoresponse for two NGO samples (S_1) and (S_2), and an LGO sample (S_3) having different resistances at 298K, (b) same data for (S_2), showing a stretched-exponential behavior, solid dots are the experimental data (dashed lines are fits of Eq. 4.1 and 4.2).

As clearly seen from Fig. 4.7a, the highest resistance sample (S_3) has not retained its initial resistive state (i.e., before UV irradiation) even after 5×10^4 seconds, while (S_1) has regained its initial state well before. Some highly insulating samples showed persistent photoconductivity (PPC) effect i.e., the sample has not retained its initial state after light exposure, where (dark exposure) time was on the scale of months. Let's stick to 'ordinary' photoresponse seen in conducting interfaces (as in Fig. 4.6), postponing a wider discussion of PPC to a separate section. In this context, I would like to add few more words on long-term relaxation, by taking data for NGO/STO sample (S_2) plotted in Fig. 4.7b. This does not follow a true exponential function; instead it can be better described by the stretched exponential relations of the form;

One can write for lamp ON,

$$R_{PC}(t) \propto \exp\left[-(t/\tau)^{\beta}\right] \qquad (4.1)$$

and for lamp OFF

$$R_{PC}(t) \propto \left(1-\exp\left[-(t/\tau)^{\beta}\right]\right) \qquad (4.2)$$

Where τ is time constant and β (usually < 1) is the stretching parameter whose fitting values were 0.22 and 0.43 respectively for Eqs. 4.1 and 4.2. Fits shown in Fig. 4.7b, verify that the data approximates a stretched exponential after an initial transient.

In addition to the above, a test experiment was performed on NGO sample, i.e., time evolution of photoresistances at different temperatures, keeping the time interval fixed. As shown in Fig. 4.8.

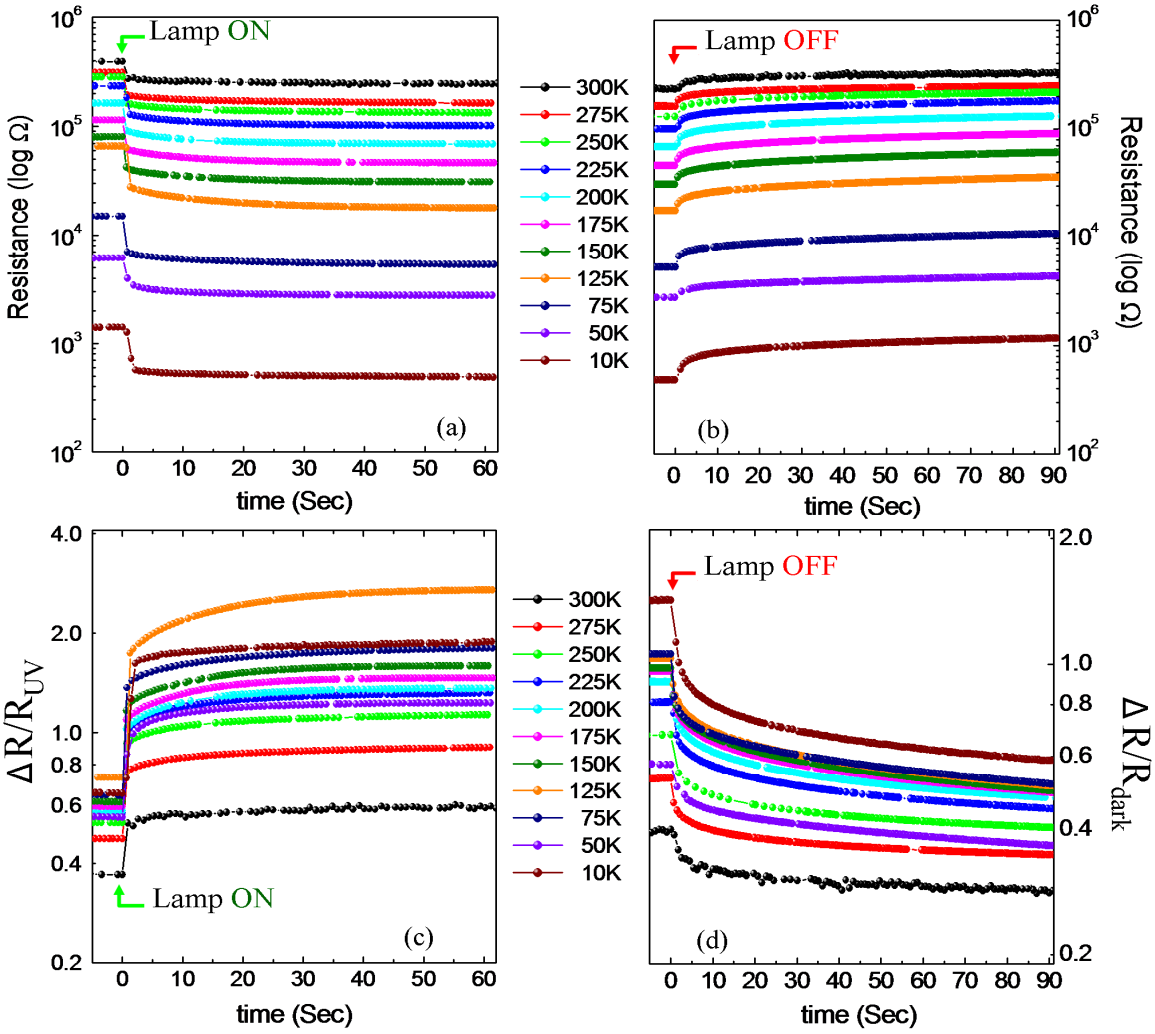

Figure 4.8: Time evolution, for NGO sample at various temperatures, of (a) photoresistance decay (Lamp ON) and (b) photoresistance recovery (Lamp OFF). (c) Same data re-plotted as ΔR/R in light (Lamp ON), extra feature is seen at 125K (orange curve) and (d) in dark (Lamp OFF).

In Fig. 4.8, time evolution of photoresistance decay in light (Fig. 4.8 a) and photoresistance recovery in dark (Fig. 4.8 b) is shown. The arrows at t = 0, shows the ON and OFF moments for lamp. Actually, with the closed cycle refrigerator (CCR) setup it is quite difficult to obtained time evolution data for longer time intervals as the temperature

changes quickly. Therefore, this data was obtained for upto 90 s, during warming path when the measurement is relatively slower than cooling path. In Fig. 4.8 (c, d), same data is re-plotted in the form of $\Delta R/R_{UV}$ and $\Delta R/R_{dark}$ respectively. Overall, photoresistance decay shows feeble traces of increase photo response with variable temperature, that are better seen with $\Delta R/R$, for example an extra increase is seen at 125K (orange curve). In Fig. 4.9, percentage change in $\Delta R/R$ (%) vs. T of the above data (Fig. 4.8) is shown for both in dark and UV irradiation (for fixed time). It is seen that $\Delta R/R$ (%) increases with decrease in temperature, interestingly, abrupt changes are seen in the vicinity of STO's 110K and 55K phase transitions (in this case 125K and 50K). The other comment is that the carriers' recombination process does not seem to be thermally assisted since the time constant seems to be independent on temperature.

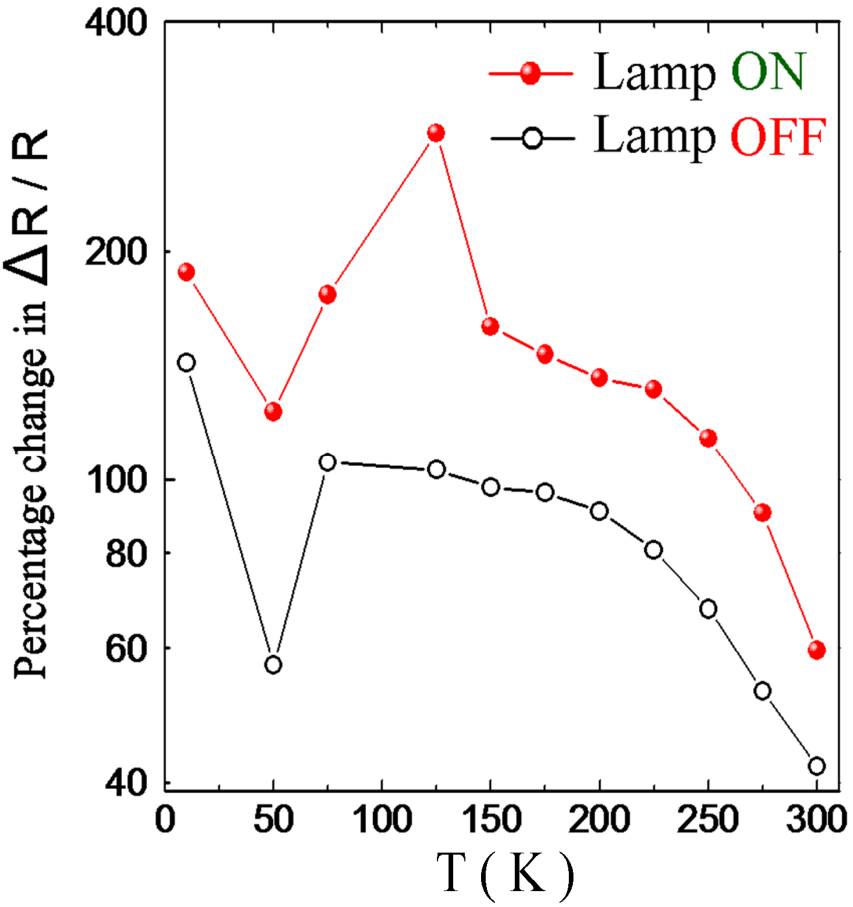

Figure 4.9: Percentage change in $\Delta R/R$ (%) vs. T of NGO sample, bottom curve (black open circle) is in dark, while top (red solid sphere) is irradiation with UV lamp.

4.5.3 Effect of different wavelengths

Indeed, this photoconductive behavior cannot be associated to the bulk response of STO, we tested that a STO crystal remains insulating under identical irradiation conditions (see Fig. 3.17). In Fig. 4.10, R_{Sheet} (T) of a NGO/STO sample named N1 irradiated by light of different wavelengths is shown.

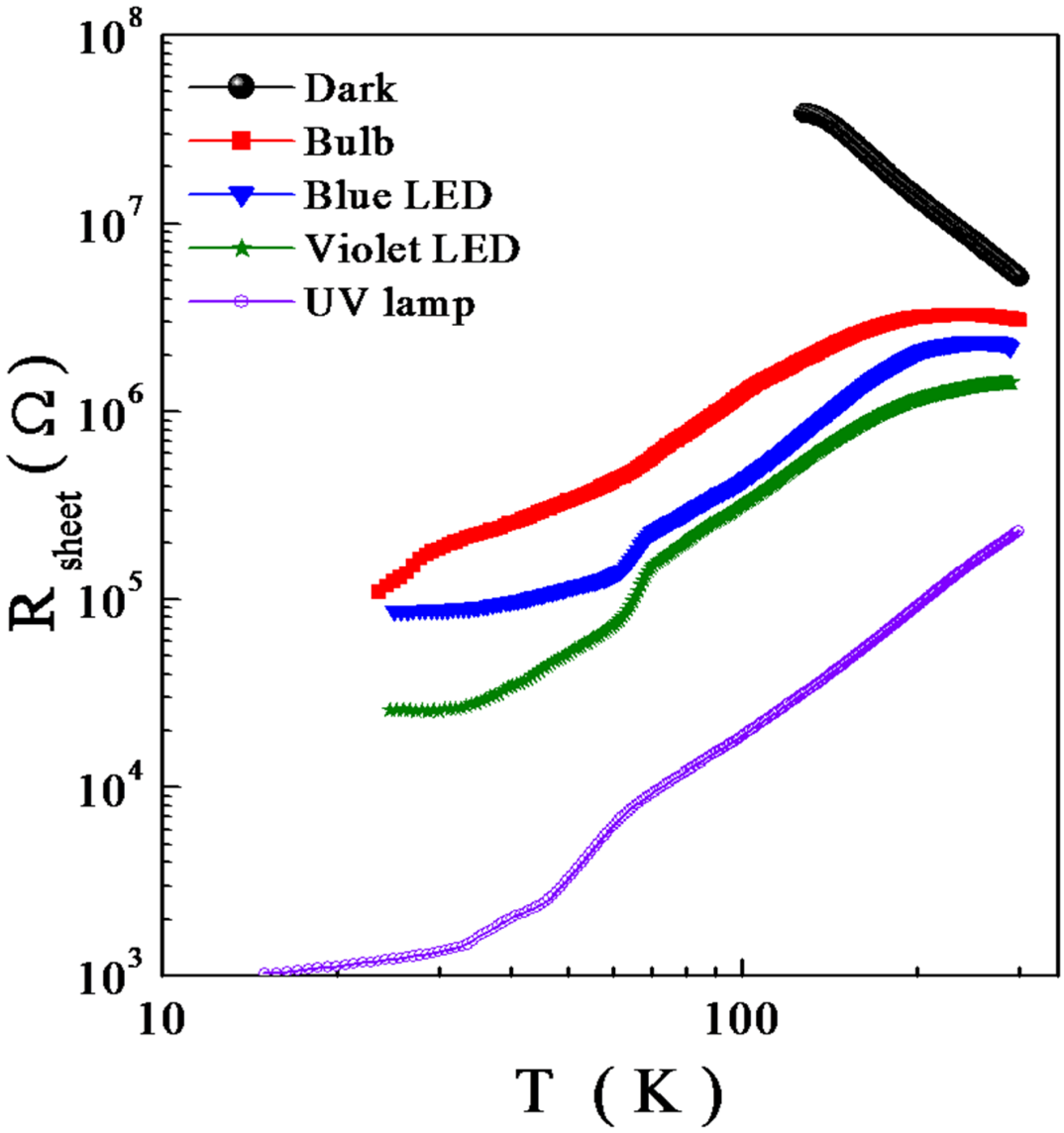

Figure 4.10: R_{Sheet} (T) of sample N1 at various wavelengths (sources of light), bottom curve (violet) is irradiation with UV lamp; from bottom to top, measurements are performed with increasing wavelength sources.

The sample measured in dark (solid black circle) showed semiconducting/insulating behavior down to 100K, where the sheet resistance becomes immeasurably high. When

illuminated by an ordinary bulb (bold red square)), the sample showed an insulator-metal transition with a metallic character under 200K. When a blue LED was used (blue solid triangle) the sample showed a further decrease in R_{Sheet} and an increase in the transition temperature (> 200K). Aheading a step further, a violet LED was used (solid green star) for exposure, which showed even stronger effect in decreasing R_{Sheet} and pushing the insulator-metal transition further in the higher temperature range (~ 250K). It is worth mentioning here that, after exposure to the respective light sources, every time the sample was kept in the darkness (24 hrs) and during this course of time sample was able to retrieve its initial state in dark (i.e., top solid black circle) or sometimes even a higher value (e.g., see Fig. 4.11a). Infact, all above measurements performed in the visible range of the spectrum (ordinary white light to violet) show nonpersistent (or reversible) insulator-metal transition with a strong dependence on wavelength (and intensity). Finally, I would like to make a short comment on the bottom curve (open violet circle) which was irradiated with UV (provided by standard Hg (A) lamp), the sample turned to metallic at room temperature (i.e., the slope of R_{Sheet} (T) was positive at any temperature). This change was irreversible (more details on such PC effect are described in next section 4.6).

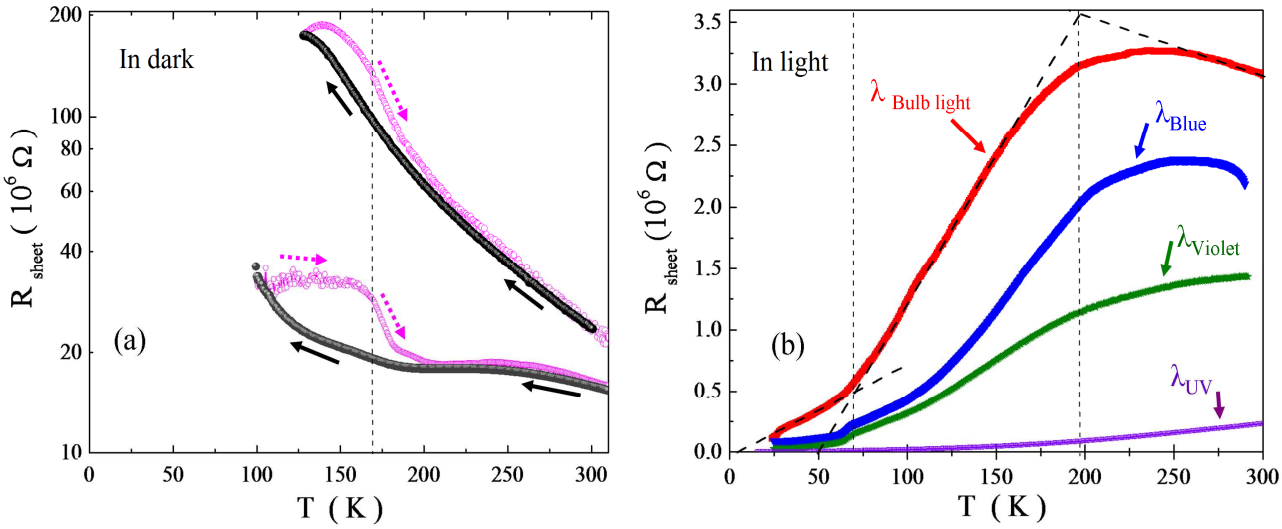

Figure 4.11: (a) R_{Sheet} (T) of sample N1 showing insulating behavior and hysteresis effect in dark, (b) same data shown in Fig. 4.10 plotted in linear mode to see the phase transition (insulator to metal) under light exposure.

In Fig. 4.11a, the cooling and warming paths for the NGO sample (N1) in dark showing insulating behavior (up to the voltage limit of the setup) are described. A hysteresis effect during warming is seen again in this case, the peak is at the same temperature (~ 180K) as mentioned before in the section 4.4.3. In Fig. 4.11b, same data plotted in linear mode to point

up the insulator-metal behavior under light also as a function of decreasing wavelength or increase in photon energy.

These results show that photon energy even less than the STO band gap energy (3.2 eV) was able to induce a change in resistance and then finally a metallic behavior. This suggests that there might be possibility of some traps states. In addition, the electrostatic potential determines a band bending in STO. The band bending determines a potential well at the interface. In the presence of a potential well at the interface, the process of PC can be triggered, since an electron can be promoted to the conductive band by light, and afterwards it goes to the interface, so moving away from the gap (supposed to be fixed); or PC can be triggered as well because the gap is annihilated by an electron injected from LAO. Here, we did not discuss in detail the presence of photoconductance effects for photons well below the direct STO gap. This might be a hint for charge transfer from the valence band of the polar material. Also the possible interpretation of PPC as due to excitons excite across the interface should be discussed in this context.

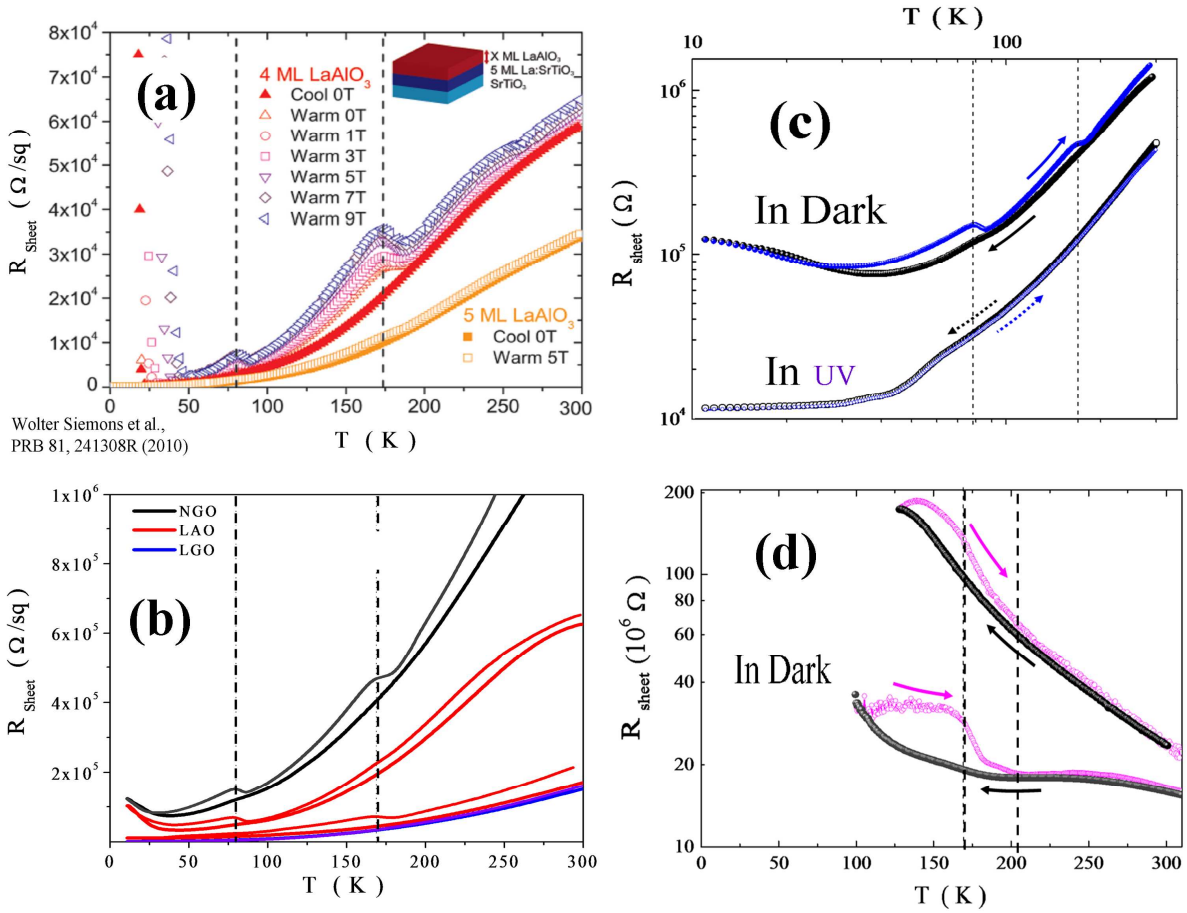

Figure 4.12: Data comparison; (a) Hysteretic effect in R_{Sheet} vs. T on warming, effect of magnetic field is also shown [145], (b) Our data showing peaks exactly at the same values, (c) hysteretic effect in our data is smoothens by UV irradiation, (d) insulating NGO sample N1 showing hysteresis in darkness.

Fig. 4.12 shows an overview of our data in comparison with recent studies by others on these oxide interfaces [145]. On the left hand side (top) an interesting hysteretic effect in oxide interfaces is shown in (a), taken from Ref. [145], together with a comparison of our data displayed in (b) to (d). As seen from Fig. 4.12a, these peaks (maxima) in hysteresis show magnetic field dependence, i.e., increasing the magnetic field (e.g., upto 9T) tend to increase the peaks and consequently the resistance, while in our case the photon filed smoothes them completely as in Fig. 4.12c. Dashed lines are guide to the eyes pointing out that these peaks appear always at the same temperatures. The peaks (maxima) in R_{Sheet} besides the low temperature upturn could be possibly due to structural changes in the Polar/STO interface during cooling and warming; perovskites often experience small transitions from cubic symmetry due to rotation and tilts of oxygen octahedra. In a recent study by Bark et al. [146] concluded that the charge transfer can be influenced by the lattice mismatch in LAO/STO. Moreover, it was shown that the LAO/STO system is conducting if the STO is under tensile strain but the carrier density is decreased exponentially by very slight compressive strain (induced by preparing LAO/STO interface on different substrates). A very recent paper by W.M. Lü et al. [147], clearly demonstrated a metal-insulator transition at a depleted LAO/STO interface, making an evidence for charge transfer induced by STO phase transitions. In view of their argument [147], the difference of the charge transfer at the interface is originating from the lattice mismatch strain at the LAO/STO interface. Actually, at room temperature there is likely to be a significant strain at the LAO/STO interface, as, STO is cubic while LAO is orthorhombic. At 110 K, STO undergoes a cubic to tetragonal phase transition while LAO remains unchanged. The c/a ratio of STO changes from 1 to 1.00056 during the phase transition [148]. This results in a reduced lattice mismatch between the overlayer LAO (polar) and STO substrate. Based on the above mismatch large charge transfer into the channel is predicted. On the other hand at the 55K phase transition the STO undergoes tetragonal to rhombohedral phase transition of reduced symmetry which may enhance the strain at the interface between LAO/STO (with c/a ratio is now 1.0004) which will increase the mismatch between the overlayer LAO and the STO substrate. This represents an increase of the lattice mismatch of 0.01% which will reduce the charge transfer to the interface, accounting for the metal to insulator transition (e.g., see Fig 4.11b).

In the end, I conclude this section by saying that there are recent reports about the complexity and phase separations in oxide interfaces which are tightly linked to the external perturbations like, magnetic field, light or biaxial stress imposed by the substrate. In this

section, I tried to show that there might be a possibility (just like manganites) that STO-based conductive interfaces exhibit phase competition between metallic and insulating phase at critical doping levels. Curiously there are recent reports [4] claiming about possible magnetism in the insulating phase of STO-based interfaces. Our experiments show that light can switch the system to metallic phase, with long recovery times. I link the hysteresis peaks appearing in the dark and smoothening by light to the phase transitions of STO and to the possibility of electronic phase separation scenario [4]. These results were reproducible in dark and under light irradiation.

4.6 Persistent photoconductance: the case of highly resistive samples

As mentioned before, when compared to LAO, NGO is more subject to degradation (as due to thermal cycling or aging). Achieving a high quality growth for NGO also seems less easy. On the basis of our experience, this is due to a higher sensitivity to the substrate-surface perfection. As a result, NGO/STO with high sheet resistance and non-metallic behaviour is occasionally obtained. The effect of UV irradiation on R_{Sheet} (T) of such kind of two NGO samples (that we call N1 and N2 respectively) is shown in Fig. 4.13.

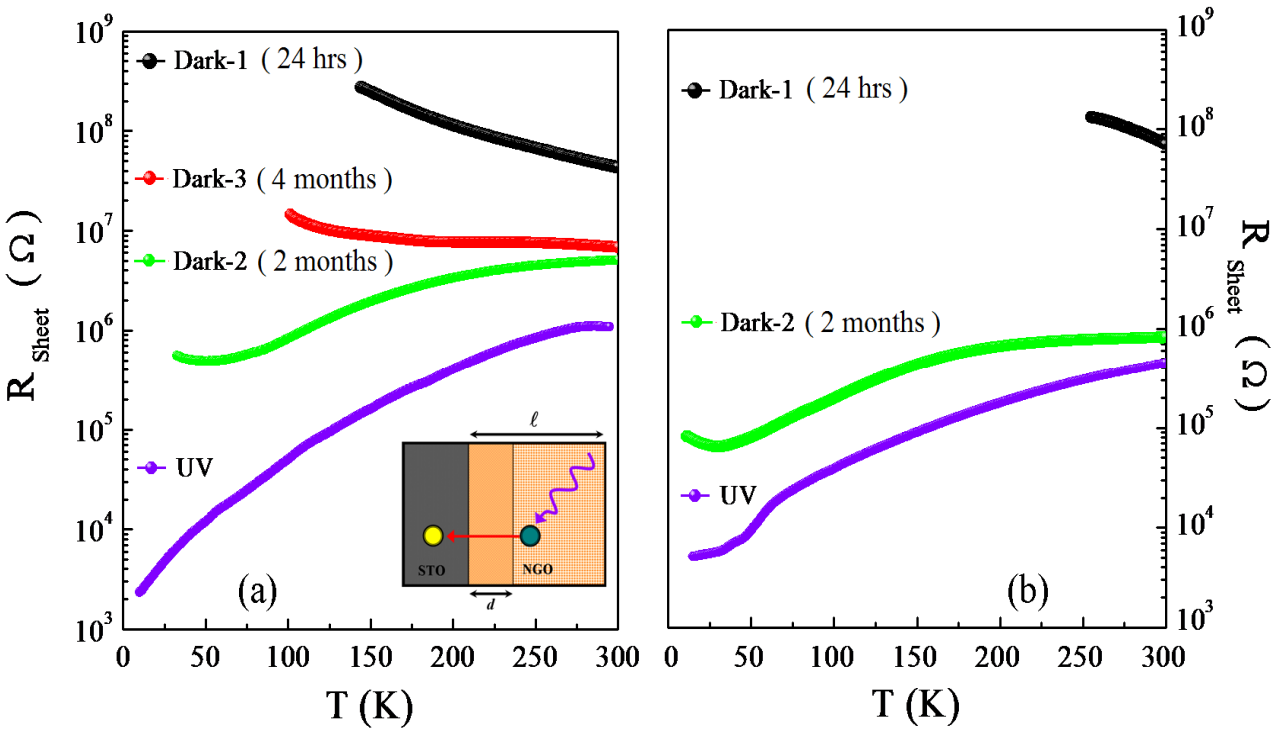

Figure 4.13: (a) R_{Sheet} (T) of sample N1 at various delay times after light exposure, bottom curve (violet) is for as-irradiated sample; from bottom to top, measurements are performed after increasing exposure to dark; (b) similar behavior seen with another sample N2.

In Fig. 4.13a, R_{Sheet} (T) of sample N1 at various delay times after light exposure is shown, bottom curve (in violet) is for as-irradiated sample; from bottom to the top, measurements are performed after increasing exposure to dark. Under exposure to UV radiation (in this case, provided by a standard Hg (A) lamp), the sample turned to metallic (i.e., the slope of R_{Sheet} (T) was positive at any temperature). This change was irreversible; subsequent measurements performed in dark demonstrated that the resistance was slowly increasing with time (on the scale of days). After several months (Dark-3 (4 months), (in red)), however, the room temperature resistance was still at least ≈ 3 (or 4) times smaller than the as-made sample (Dark-1 (in black)). This behavior shown by sample N1 was reproduced with another NGO sample N2 as described in Fig. 4.13b. Here, delay time after light exposure was two months (Dark-2 (in green)).

4.6.1 Discussion

Here we describe a model for log time response. In association to Fig. 4.14, similar permanent photoconductivity (PPC) is frequently observed in semiconducting heterostructures (see ref. [149], and references quoted therein). Among them, of particular interest for the present work is the case of structures that host a 2DEG (such as AlGaN/GaN). PPC is there determined by the transfer of photo-excited electrons from the deep level donors of the charge reservoir to the conduction band of the other side of the junction.

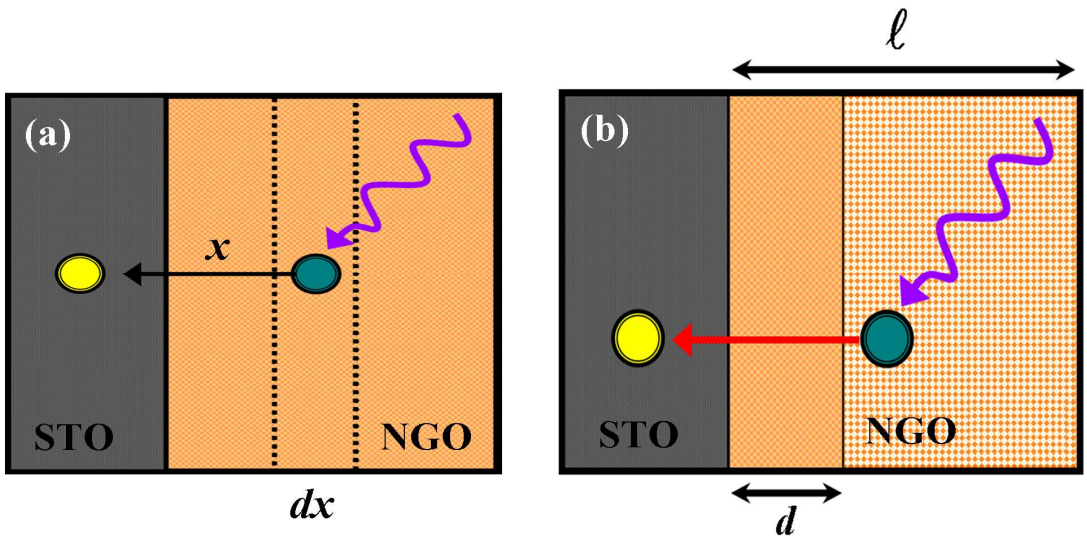

Figure 4.14: Model for log time response**;** (a) long-living electron-hole pair generation by photon is possible only if electron is injected into STO, (b) charge transfer process from a slab of non-negligible thickness ℓ and potential barrier *d*.

A photon can create a long-living electron-hole pair only if the electron is injected in STO, while the hole remains trapped in NGO (or polar layer). This process implies that free electrons are injected into STO through a tunnelling barrier. The number of photo-induced carriers that have been injected at time t, coming from a slab with thickness *dx* at distance x (as in Fig. 4.14a), is:

$$dn = \mathrm{N}\left(1 - e^{-\frac{t}{\tau(x)}}\right)dx \qquad (4.3)$$

where $\tau(x) = \tau_0 e^{\frac{x}{a}}$ is the tunnelling time through distance *x*, between states with characteristic length scale *a*; *Ndx* is the total number of trapes that are created in the slab. These values depend on the light intensity and it is regulated by the local processes of recombination.

As stated before, for semiconducting structures hosting a 2DEG, their PPC is determined by the transfer of photo-excited electrons from the deep level donors of the charge reservoir to the conduction band of the other side of the junction. Thus, recombination is then prevented by the potential barrier that separates the two slabs. In other terms, the observation of PPC is a signature of the charge transfer at distance, across a potential barrier of width *d*, from a slab with non-negligible thickness ℓ (see inset of Fig. 4.13 or Fig. 4.11b). The total number of injected carriers is:

$$n = \int_0^{\ell} \mathrm{N}\left(1 - e^{-\frac{t}{\tau(x)}}\right)dx \qquad (4.4)$$

where ℓ is the effective NGO thickness that is involved in the process. After trivial calculation, we get:

$$\frac{n}{N\,a} = \int_{\tau_0 \exp\left(\frac{d}{a}\right)}^{\tau_0 \exp\left(\frac{\ell}{a}\right)} \frac{1 - e^{-\frac{t}{\tau(x)}}}{\tau}\,d\tau \qquad (4.5)$$

$$\frac{n}{N\,a} \approx \int_{\tau_0 \exp\left(\frac{d}{a}\right)}^{\tau_0 \exp\left(\frac{\ell}{a}\right)} \frac{\left(1-\theta\left(t-\tau\right)\right)}{\tau}\, d\tau \qquad (4.6)$$

$$\frac{n}{N\,a} \approx \begin{cases} 0 & t < \tau_0 \exp\left(\frac{d}{a}\right) \\ \ln\left(\frac{t}{\tau_0}\right) - \frac{d}{a} & \tau_0 \exp\left(\frac{d}{a}\right) < t < \tau_0 \exp\left(\frac{\ell}{a}\right) \\ \frac{\ell}{a} & \tau_0 \exp\left(\frac{d}{a}\right) < t \end{cases} \qquad (4.7)$$

Under this circumstance, theory foresees that both the onset and the decay of PPC follow a logarithmic law [150]. A logarithmic dependence is also observed in the case of NGO/STO, as demonstrated in Fig. 4.15 (a) and (b).

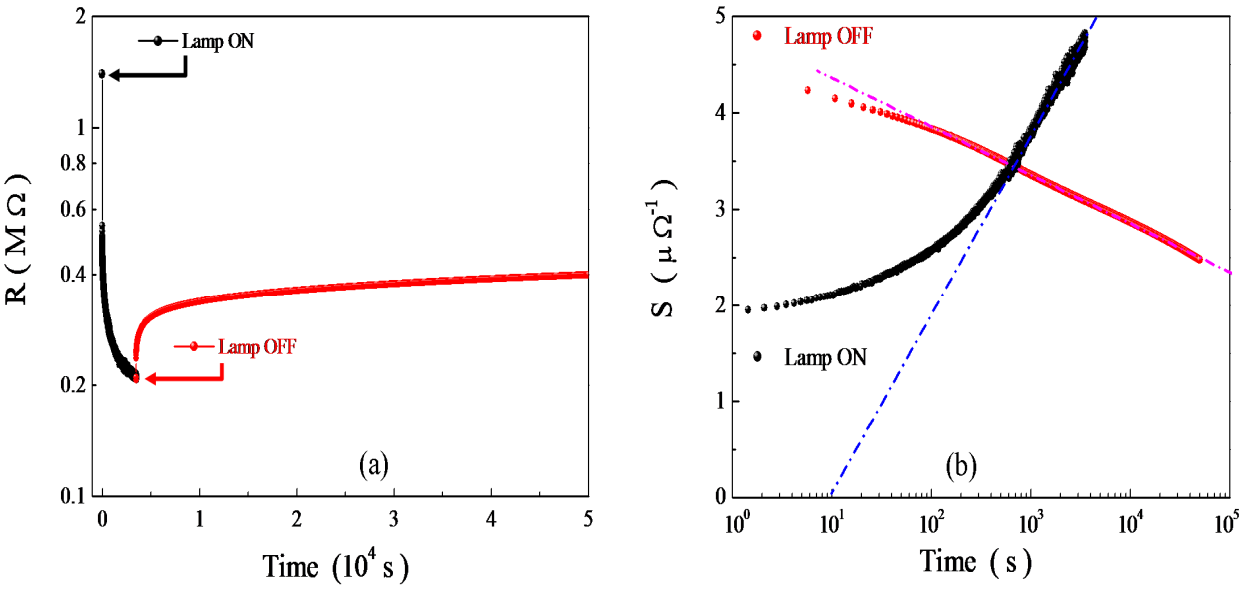

Figure 4.15: (a) time dependence of photoresponse, arrows indicate the on and off moments of lamp; (b) same data replotted in log-linear scale.

Indeed, this behavior cannot be associated to the bulk response of STO. Indeed, we tested that a STO crystal remains insulating under identical irradiation conditions (see Fig. 3.17). Furthermore, the relaxation of STO after UV irradiation has been thoroughly

investigated, demonstrating a complex dynamics but excluding logarithmic decays [151, 152, 153]. By extrapolating the plots, it is possible to determine two characteristic times $t_1 \approx 10$s and $t_2 \approx 10^4$s, that describe respectively the delay after which the log behavior starts, and the saturation time. Within the standard models of PPC [150],

$$t_1 \approx \tau_o \exp\left(\frac{d}{a}\right) \tag{4.8}$$

and

$$t_2 \approx \tau_o \exp\left(\frac{\ell + d}{a}\right) \tag{4.9}$$

where a is the length scale of the electronic orbitals (i.e., of the order of the Bohr radius) and τ_0 is a characteristic time of formation/ annihilation of an electron-hole pair; $\tau_0 \approx 1$ ns for both STO (a value that we consider typical for perovskites) [150], and for GaAs [154]. By the data, we get $d \approx 6$ unit cells and $\ell \approx 2$ unit cells. That is, a slab with thickness of the order of 2 u.c. of NGO is involved in the process of injection. Assuming $\tau_0 \approx 10^{-9}\, s$ (as for GaAs) we get that the minimum distance where carriers are injected from is $d \approx 25\, a$, that is of the order of $d \approx 6$ u.c. of NGO.

Finally, we add a few comments on PPC. First, we notice that PPC also appears in insulating LAO/STO and LGO/STO (e.g., samples prepared at high oxygen pressure, as in ref. [155]). Thus, it may be regarded as the typical photoresponse of insulating polar interfaces. In the PPC, electrons are effectively promoted to the conduction band by light, determining a sensitive variation of conductance. This is different from the "ordinary" photoresponse, as illustrated, e.g., by Fig. 4.6 and Fig. 4.7. According to the described analysis of data, the injection seems to regard electrons that are formerly far away from the interface. Under this respect, PPC may have some connection with the electric field effect: when a negative gate voltage is applied to an insulating (i.e. 3 u.c. thick) polar layer, electrons are injected at the interface [154,156]. In this case, the injection is determined by light.

In summary, we probed the transport properties and the effects induced by UV light irradiation on highly epitaxial $NdGaO_3/SrTiO_3$, $LaGaO_3/SrTiO_3$ and $LaAlO_3/SrTiO_3$ heterostructures. The metallic nature was confirmed by electric transport measurements even at 10^{-1}mbar which is a novel result from our group in Naples. We demonstrated the

conducting nature of 2DEG formation at the interface in above structures is related to the intrinsic electronic reconstruction scenario, and their transport properties qualitatively similar to those of $LaAlO_3/SrTiO_3$. This also shows that neither Al nor La plays any crucial role in the underlying mechanism. Additionally, these results show a possibility of charge transfer to the q2DEG layer is influenced by the interface strain, which accounts for the reduced charge transfer to the polar/non polar interface. Interestingly, some major photoconductance effects were found also for photon energies well below the STO gap, strongly suggesting a situation in which the photoinduced long lived excitons have the hole in the polar layers and electrons in STO. Furthermore, all the three types of structure characterized under UV irradiation show strong intrinsic tendency of photoconductivity. Under suitable conditions, the effect in $NdGaO_3$/STO (polar/non polar) may be permanent. Last but not the least, our procedures and techniques were capable of reproducing the known results to a high degree of accuracy. Finally, I would like to comment for possible future directions, measurements on these interfaces both in magnetic filed (upto several Tesla) together with UV light switched ON will be interesting.

Summary and conclusions

A number of systems based on the transition metals Mn and Ti were analyzed in the course of this work by means of variable temperature resistance measurements, also as a function of light irradiation and of an applied magnetic field. The research activity was especially dedicated to two quite outstanding cases of transition metal oxide based systems, i.e.:

a) $Pr_{1-x}Ca_xMnO_3$ (PCMO), a narrow band manganite showing an insulating behaviour across it's whole phase diagram;

b) polar-non polar oxide interfaces, where the formation of a high mobility 2-dimensional electron gas (2DEG) in $SrTiO_3$ is triggered by the deposition of a polar overlayer. In particular, I demonstrated the 2DEG formation within the novel $NdGaO_3/SrTiO_3$ heterostructure, aside to the celebrated $LaAlO_3/SrTiO_3$ heterostructure and to the more recent $LaGaO_3/SrTiO_3$.

Recent literature discussed in this work shows that not only narrow band manganites but also polar-non polar conductive interfaces exhibit phase competition between metallic and insulating phases at critical doping levels. Curiously, magnetism if found in the metallic phase of manganites and – as recently suggested - in the insulating phase of STO-based interfaces. Our research was therefore addressed to a better understanding of the nature of transport in the unperturbed samples and then of the light-induced effects.

Summary of experimental results

In chapter 3, the effect of the substrate induced strain on the transport properties of PCMO films has been investigated. No evident feature is present at the expected charge ordering temperature as reported in bulk (T_{CO}= 230 *K*). In spite of the different structural details, PCMO_110 and PCMO_001 show a similar overall transport behavior and there is no FM metallic phase evident from the analysis of the R (T) data. The drop (bend) in resistance with 4-probe data are indicative of false transition (FM) that can be get rid of by increase in delay time. The observed experimental results suggest that, the thermally activated hopping (TAP) of small polarons model is more suitable for describing the temperature dependence of

resistance for the PCMO thin films down to 150K than the VRH conductivity model. It was shown that the robust, nonbulk like FM phase obtained by the epitaxial deposition of PCMO on (110) STO (PCMO_110) under low electric field does not undergo a transition towards a metallic state. Therefore, as it happens in the bulk and PCMO_001 films, the metallic DE phase remains hidden in PCMO_110 films as well. Finally, we have shown that UV light irradiation is an interesting tool which can change the doping of manganites with a gradual and reversible change of the carriers concentration using the same sample. UV Light has induced a transition to the hidden metallic phase in PCMO thin films which have no metallic state in the darkness. So, the manganite is rendered metallic by illumination but the effect is non persistent. Furthermore no PC effect is seen at room temperature as claimed by others. We showed that, while the ultrathin PCMO_110 (10-066: PCMO_110 (10 nm)) film is photoconductive and the insulator-metal transition (FM) which had been hidden in normal scenario is recovered under illumination, in contrast the PCMO_001 (10 nm) do not show this effect. This behavior cannot be associated to the bulk response of STO. We tested that an STO crystal remains insulating under identical irradiation conditions. This slightly opens up the possibility for the observation of a fascinating phenomenon, i.e., the photo- induction of ferromagnetic behavior by light, in FMI state of PCMO at low temperature. By changing the doping with light, probably we pass from the FM insulating to the FM metallic phase supporting the scenario of phase coexistence (phase separation) in complex oxides.

In chapter 4, the attention was mainly concentrated on comparison of transport properties between high quality $NdGaO_3/SrTiO_3$, $LaGaO_3/SrTiO_3$ and $LaAlO_3/SrTiO_3$ heterostructures, all hosting a two dimensional electron gas at the interface. I have investigated the transport properties and the effects induced by UV light irradiation on these heterostructures and confirmed their metallic nature by electric transport measurements. A novel result in the form of conducting nature of these interfaces is obtained at 10^{-1} mbar. I showed the conducting nature of 2DEG formation at the interface in above structures (grown at 10^{-3} mbar) and their transport properties qualitatively similar to those of $LaAlO_3/SrTiO_3$. In addition, I purposed on the basis of transport data that the interface strain between STO and LAO or between gallate based films and STO to be responsible for modulating the charge transfer from top polar layer to STO. Finally, all the three types of structure characterized under UV irradiation show strong intrinsic tendency of photoconductivity. Under suitable conditions, the effect in $NdGaO_3$/STO (Polar-non polar interfaces) is permanent. Regarding effect of UV irradiation, it was shown that photoconductivity (PC) is more prominent in high R_{sheet} samples than low

R_{sheet} samples. Moreover, significant reduction of the resistance under light is observed in the low temperature region, where the increment of conductivity suppresses the resistance upturn (resistance minima). The fits of the low temperature region upturn (by a formula usually used for magnetic impurities) were suggestive that there might be a hidden magnetic phase (which is insulating, in contrast to the case of manganites). The strong temperature dependency of the PC is already a hint that the origin of the effect is not a simple increase in charge carriers but rather complex and possibly a phase separation scenario also in these complex oxide interfaces. The transport data was analysed and discussed in context of an interesting hysteresis effect seen in the R (T) data showing peaks during warming path. These peaks are magnetic and photon field dependent but with opposite effects i.e., increasing the magnetic fields tend to increase the peaks and consequently the resistance, while in our case the peaks decrease with increase in photon field (i.e., by modifying wavelength or intensity) and vanished under UV, we did not discuss in detail the presence of photoconductance effects for photons well below the direct STO gap. This might be a hint for charge transfer from the valence band of the polar material. Also the possible interpretation of PPC as due to excitons excite across the interface should be taken into account in this context. In addition, a possible robust coupling between the structural phase transitions of STO and the transport properties of the q2DEG in polar/non polar oxide heterostructures was described, which gives evidence for charge transfer variations from the polar layer to the polar/non polar interface. The results were reproducible and so were the phase transitions and hysteretic effects on the transport properties. Finally, all the three types of structure characterized under UV irradiation show strong intrinsic tendency of photoconductivity. The photoinduced conductance in formerly insulating $NdGaO_3$/STO (polar/non-polar interfaces) was found to be persistent on the timescale of months.

Conclusions

In conclusion, the transport properties of epitaxial thin films of two different transition metal oxide based correlated systems were analysed by resorting to variable temperature resistance measurements in dark and under UV light.

Thin films of the narrow band manganite PCMO showed an insulating behaviour at all temperatures, that we attribute to thermally activated hopping of small polarons, in spite of the strong strain-induced magnetism previously found on samples grown on (110) oriented $SrTiO_3$ substrates. Our data show that it was possible to induce, only on samples grown on

(110) oriented $SrTiO_3$ substrates, a colossal insulator to metal transition with a decrease of the low temperature resistance of about ten orders of magnitude. Our data clearly demonstrate that light affects the transport properties of PCMO only under the Curie temperature. Light allows therefore to undisclose the ferromagnetic metallic state, common to most manganites, but normally "hidden" in PCMO because of a competing ferromagnetic insulating state presumably related to charge and/or orbital ordering. The case of epitaxial polar-non polar heterostructures is even more complex, since our analysis on previously metallic or insulating samples showed a remarkable sample-to-sample dependence. Persistent photoconductivity was found with decay times that increased for the most highly resistive samples up to values of the order of months or more. Interestingly, some major photoconductance effects were found also for photon energies well below the $SrTiO_3$ gap. We argue in our discussion that such data strongly suggest a scenario in which the photoinduced long-lived excitons have the hole in the polar layers and electrons in $SrTiO_3$.
In both cases, our experiments show that light can switch the system to the metallic phase, with recovery times that differ by orders of magnitude in the two systems.

The absence of any photoconductance effect above the Curie temperature of manganites shows that light effects should not be envisaged as simple photodoping but analysed in the framework of competing ground states in an intrinsically complex system. Understanding in detail the nature of the photoconductance effect in previously conducting or insulating STO-based interfaces, a still relatively unexplored field of research, would require more extensive efforts to master the complex phenomenology and the sample-to-sample dependence.

A1: Appendix 1

A1.1 Gifford-McMahon (G-M) thermodynamic cycle

The (G-M) thermodynamic cycle scheme used by the CCR setup has helium gas as the refrigerant. The gas compressor (operating near room temperature) and the cryogenic expansion cylinder (cold head) are thermally linked by a regenerator or thermal storage device. The gas is driven through the 4-step cycle shown in figure A1.1.

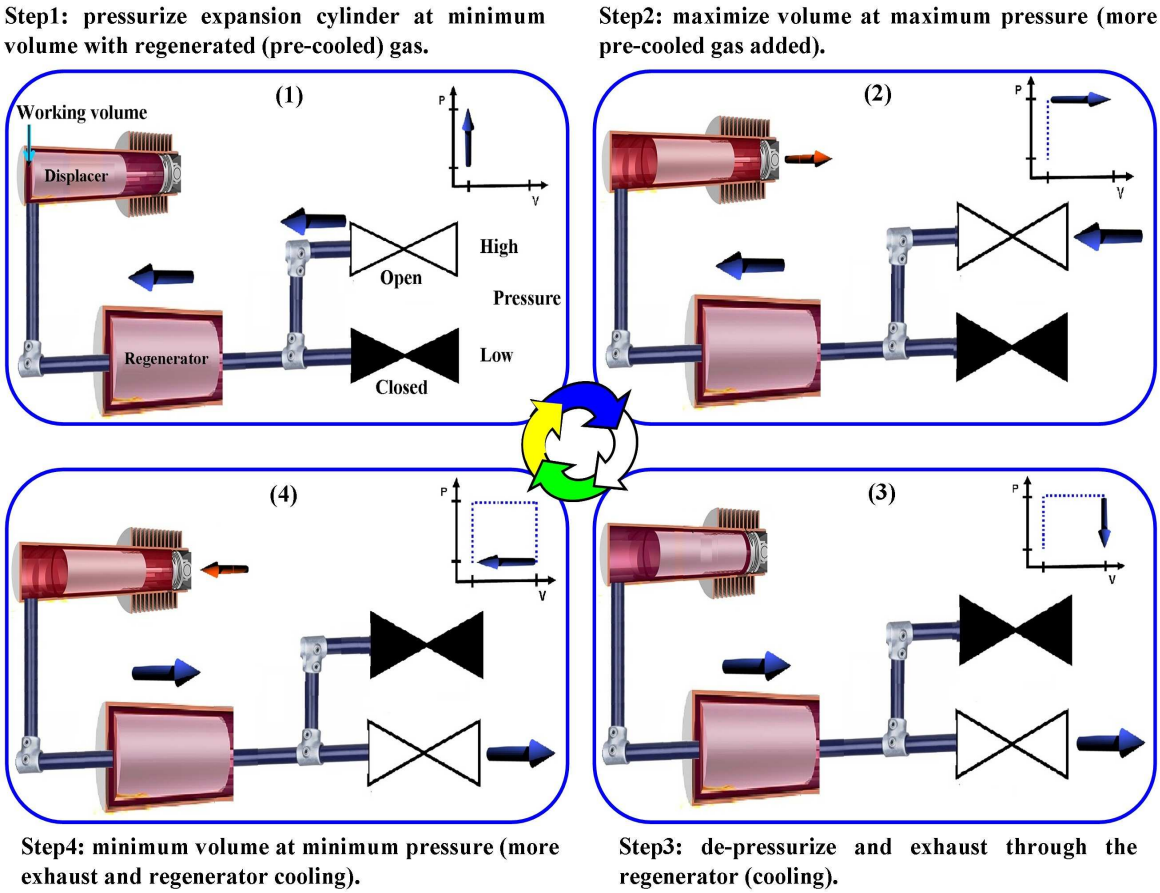

Figure A1.1: The Gifford-McMahon Refrigeration Scheme used by the CCR setup

A2: Appendix 2

A2.1 Transport characterizations of PCMO thin films

In this section, I would like to make few comments on the R (T) characterizations of PCMO. In the very initial measurements (year 2008) it was frequently observed some strange features in the R (T) data consisting of jumps (around 200-250K) and noisy behavior followed by a drop (bend) in the resistance about 130-150K (depending also upon thermal history or aging of the sample) as shown in Fig. A2.1a, while Fig. A2.1b shows a set of recent smooth measurements. On the basis of my experience, this bend is always accompanied by compliance indicator of the bias generator blinking and interchange of the voltage signs in this sequence;

For positive voltage $V_+ \rightarrow V_-$ and

For negative voltage $V_- \rightarrow V_+ \rightarrow V_-$

(it can be seen on the front panel of the nano-voltmeter).

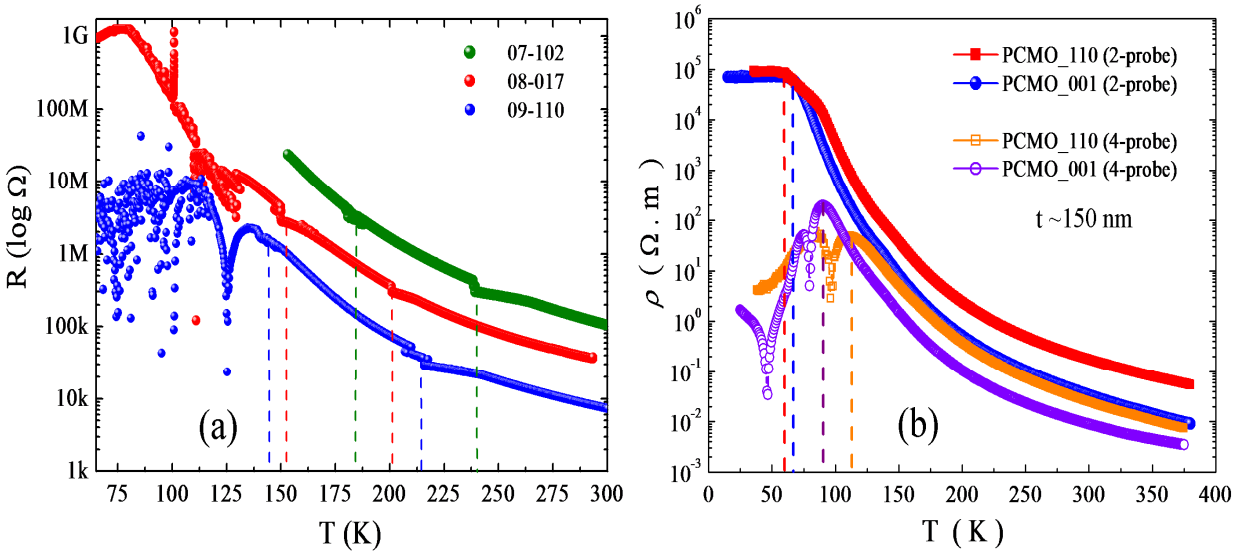

Figure A2.1: (a) A set of early transport measurements (R vs. T) for several PCMO samples, showing jumps and noisy behavior. (b) A set of recent transport measurements (ρ vs. T) showing smooth data (see text for more details).

It was difficult to analyse this data in a sense that these features were appearing at the points where phase transitions are reported in the phase diagram for bulk PCMO i.e., charge ordering temperature T_{CO} and the Néel temperature or magnetic ordering temperature , T_N, as shown by dashed lines in Fig. A2.1a. Indeed, based on our measurements alone, we were

unable to make any specific comment about the origin of these features. Because, on the one side these features in the R (T) data were very fascinating, but on the other hand in literature reported resistivity data were quite clean and smooth (at least down to 150 K) making above scenario more puzzling for us (see e.g., Fig. A2.1b that resembles with the usual data shown in literature). Moreover, the noisy behavior in the R (T) curves just before and after the drop in resistance (between 100-150K) look similar to what reported for single crystals below 40K, that was interpreted as temporal fluctuations between low and high resistance states [i]. In addition within this noisy region, the I-V curves showed strange elliptical loops. There are also reports about colossal dielectric response and multiferroic nature in charge-ordered rare earth manganites in the above temperature window [ii, iii]. Finally, a survey of the literature had made things more complex at that time. For example see Fig. 3.4, for a quick comparison (with Fig. A2.1), which is taken from Ref. [iv] reporting that in the low-temperature range ($T < T_N$) an abrupt change is observed in the temperature dependence of the resistivity which they claimed as an appearance of the metallic phase.

It is important to stress that we tried several steps, e.g., checking internal wiring of the setup (for the possible artifacts), investigating measurement techniques (2-probe and 4-probe methods), replacing measuring devices (Kithley and Agilent) and performing different tests regarding bonding (or contacts). Indeed, the measurement setup was working nicely (in healthy condition) because the measurements obtained for other compounds like, $LaMnO_3$ (LMO), YBCO, LSMO, LAO/STO and LSMO/YBCO/STO multilayers, to name a few, were in excellent agreement with the reported data in literature. Moving a step further to make a consensus that whether the system responds intrinsically or impedance is an issue, we decided to probe further the implications of our measurement procedure for the measured value of resistivity; the most important being the time delay between current application and voltage measurement.

A2.1 Issue of time delay

In view of above context, we devised a test experiment hoping that if the system intrinsically has a temperature- and phase-transition-dependent response time feature, the final result of the measurement might change with the delay. At the end of the day, indeed it does (see Fig. A2.1b or Fig. A2.2). As an example, when we increased the delay between the application of current (in pulsed mode) and the voltage measurement to 1- 2s the features started to show suppression. This change was really remarkable; subsequent measurements performed on e.g., PCMO_001 (150 nm) sample (all other PCMO samples shown in Table

3.1 were also tested) demonstrated that the resistance was slowly smoothing with increase in delay time (~ upto 6s) down to 70K. The above experiment was a big success in a sense that, it has enabled us to go down in temperature window of the order of ~ 70K more (i.e., from 160K (before delay) – 90K (after delay)).

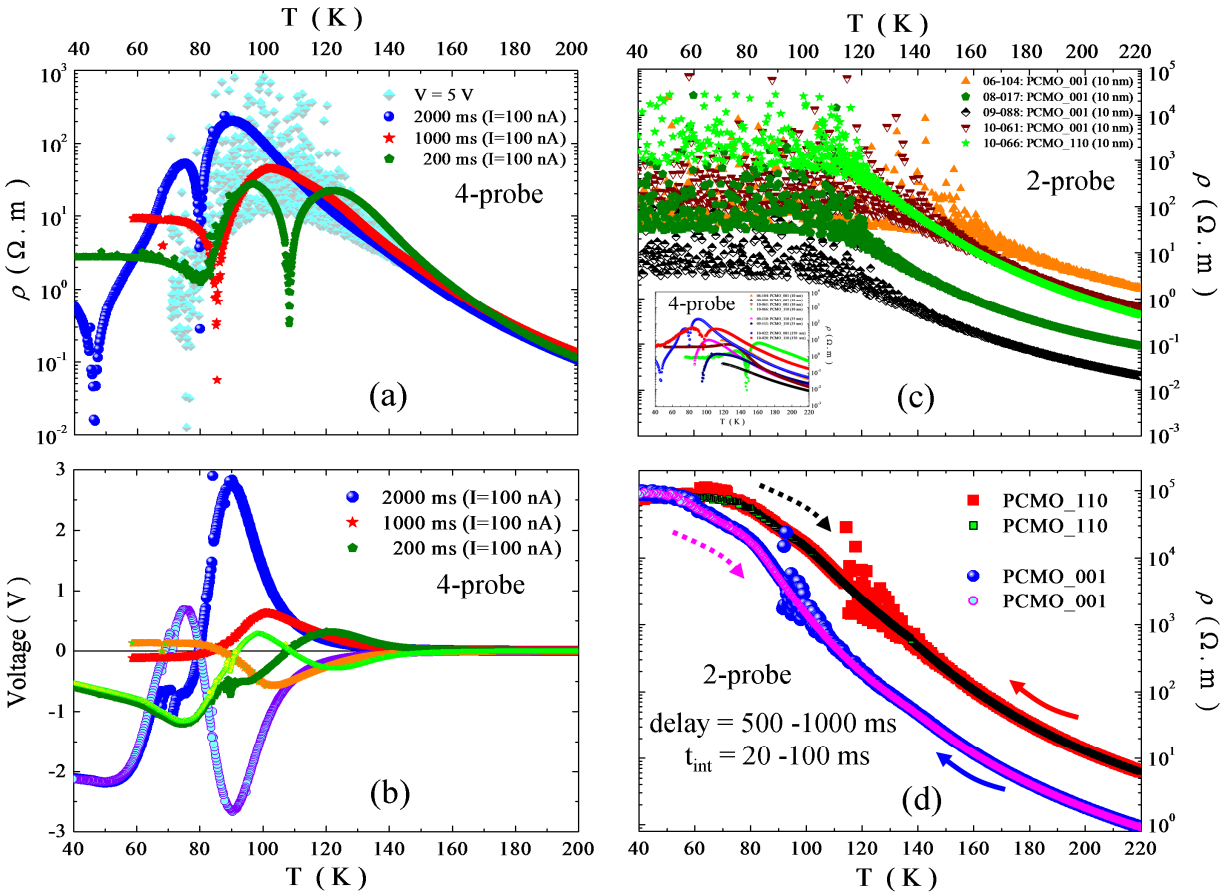

Figure A2.2: (a) Delay effect on the 4-probe resistivity of PCMO_001 (150 nm) thin film, (b) voltage dependence on the temperature for different delays recorded during the measurements shown in (a) for PCMO_001 (150 nm) sample. (c) Temperature dependence of 2-probe resistivity (inset shows 4-probe) for several PCMO samples of different thickness. (d) Delay effect on the 2-probe resistivity of PCMO_110 and PCMO_001 (150 nm) samples.

In view of above context, let me describe the Fig. A2.2 in the following few lines together with brief comments. In (a), two main issues are highlighted;

(i) Firstly, a comparison between 4-probe measurements performed in two different biasing modes namely, constant voltage and constant current. It is clearly seen that, the temperature window where PCMO is known to show magnetic transitions the data also show strange behavior. For example the characterization of PCMO in constant voltage bias typically shows a noisy behavior (whether 4-probe or 2-probe) whenever entering this regime (see also Fig. A2.2c, and A2.2d),

while the case of constant current (in pulsed mode) shows, typically, a drop (bend) in resistance (which is always accompanied by compliance indicator of the bias generator blinking).

(ii) Secondly, for the case of 4-probe (pulsed current mode) measurement performed on PCMO_001 (150 nm) sample the effect of increasing delays (from 200 – 2000 ms) is described. Quite interestingly, the usual drop in PCMO's resistance around 150K-120K (e.g., green curve for the short delay case) become smoother in the longer delay measurement (blue curve) and shifted to 90K.

The effect of voltage dependence on the temperature for different delays ranging from 200-2000 ms are shown in Fig. A2.2b, that were recorded during the measurements shown in Fig. A2.2a for the same PCMO_001 (150 nm) film. In Fig. A2.2c, the temperature dependence of 2-probe resistivity in constant voltage bias (= 5V) for several PCMO samples of same thickness (10 nm) is shown, where all samples begin to show noisy behavior around 150K, while inset shows dropping of resistances with 4-probe pulsed current mode in the same temperature window. A similar behavior is also seen in Fig. 3.2, where 2-probe and 4-probe measurements were compared for all the PCMO samples. Fig. A2.2d, describes the delay effect on the 2-probe resistivity in constant voltage bias (= 5V) of PCMO_110 and PCMO_001 (150 nm) samples. The following procedure was used for this short test experiment; the measurements were started with short delay time during cooling path (solid arrows) and after observing the start of noisy behavior the delay time was changed to loner value, interestingly measurement became smooth. The warming paths (broken arrows) were performed keeping the longer delay times, clearly, the noisy regimes were completely wiped out in this experiment.

Now coming back to the point, i.e., of making a consensus about the intrinsic response of the system (i.e., PCMO), we recorded the voltage output separately for the forward and reverse currents as a function of temperature (see Fig. A2.2b). For the case of short delay (200 ms), as the temperature is lowered below 130 K the positive voltage output (V_{+}, dark green) starts to decrease and change its sign (i.e., V_{-}) below 110K and stays negative after on. Indeed, the negative voltage output (V_{-}, light green) does the opposite, but below 100K it regains its original negative sign. It is worth mentioning here that for even lower delay values (20 ms) the voltage starts to decrease around 200K and reverse its sign at about 180K and stays negative after wards (not shown here). Now, both voltages stay negative and do not change sign even though the current is reversed in the short delay case (in my opinion

perhaps this causes to blink compliance indicator of the generator). Considering the case of longer delay (2000 ms), both voltages stay negative without changing their sign below 70K. Infact, the approximate symmetry between the voltages signals for forward and reverse currents, which is clearly seen in the longer delay case over the entire temperature range, is seen to be lost even at temperatures as high as 180 K in the short delay case.

Lastly, I would like to make few comments. A typical bell shaped hump observed in the capacitance data [iii, v] or a sharp peak observed at the CO transition in the magnetization data [vi] is not reflected strongly in the resistivity measurement, simply because the resistance value in this temperature range is small and therefore the *RC* time constant is smaller than the measurement delay. Moreover, when we increased the width of the forward (and reverse) current pulse, once again we obtained a dependence without the sharp drops at the transition points. We also measured the resistivity by two-probe method (only positive current direction), in this case again we get a featureless dependence similar to that shown in Fig. A2.2. Finally, these data appear similar to what is reported in the literature usually.

L. V. Saraf et al. [v], have performed a study on the capacitive effect and made a correlation of large dielectric response with the ordering transitions PCMO (x=0.33) thin films grown onto (100) oriented LAO substrate by PLD. Based on their results, these authors attribute the occurrence of upward and downward jumps in their capacitance data (i.e., capacitance is high) at temperatures close to the CO and spin ordering temperatures, to the existence of magnetic disorder (frustration) in the multiphase system. Indeed, it seems that the resistivity drop (bending) or initiating of noisy behavior (Fig. A2.2) in our case, also observed by others [iv, vii], and capacitance jumps [iv] are seen at the transitions when the system is driven faster than a specific time scale indicate that relaxations and reorganizations of polaronic and magnetic clusters are playing a key role. The above scenario can be easily explained on the basis of the circuit response effect [v], controlled by the impedance of PCMO film. For this purpose a graphical representation for the impedance of PCMO film, actually, controlling the circuit response effect is sketched in Fig. A2.3.

Assume a circuit element having, inherent, resistive and capacitive character (like, the case of PCMO film), driven repeatedly by currents in pulsed mode in the form of a wave form (red square wave) as shown in Fig. A2.3. For the case of a short delay measurement, the time positions are denoted by $t_{1\,(short)}$ and $t'_{1\,(short)}$, while $t_{2\,(long)}$ and $t'_{2\,(long)}$ are positions for a measurement with longer delay. Now, if the RC time constant of the sample is comparable or longer than the pulse width of the current signal, the voltage attained (dashed blue) after

forward current will take time to reverse under current reversal. Thus, a short delay measurement (i.e., $t_{1\,(short)}$ and $t'_{1\,(short)}$) would show the same sign of the voltage although it may decay in magnitude over the pulse width. This effect would be diminished or get rid of by enhancing the delay (e.g., $t_{2\,(long)}$ and $t'_{2\,(long)}$).

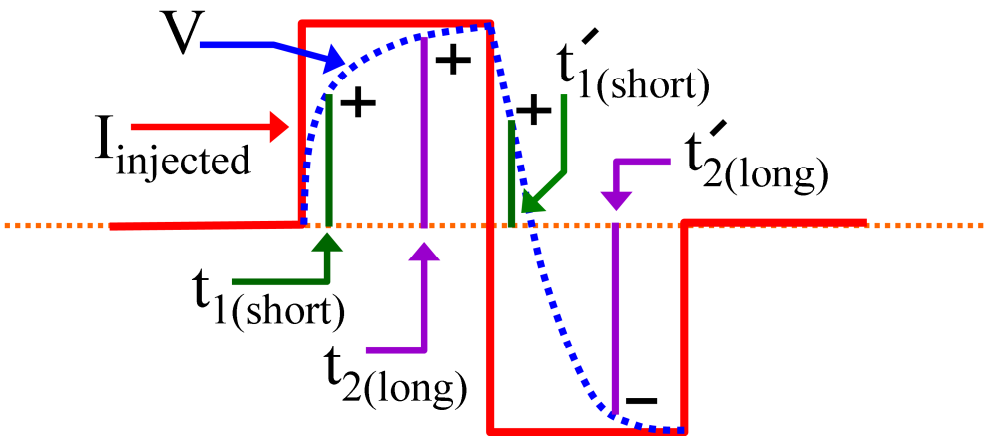

Figure A2.3**:** A graphical representation of the impedance of PCMO film controlling the circuit response effect.

In Fig. A2.4, a comparison of recent 4-probe resistivity data between PCMO_110 and PCMO_001 (both 10 nm) thin films (after delay modification), taken in constant voltage (5V) and constant current (pulsed current of 100 nA) modes, is shown. Inset show 2-probe data in constant voltage (5V) configuration for the same samples.

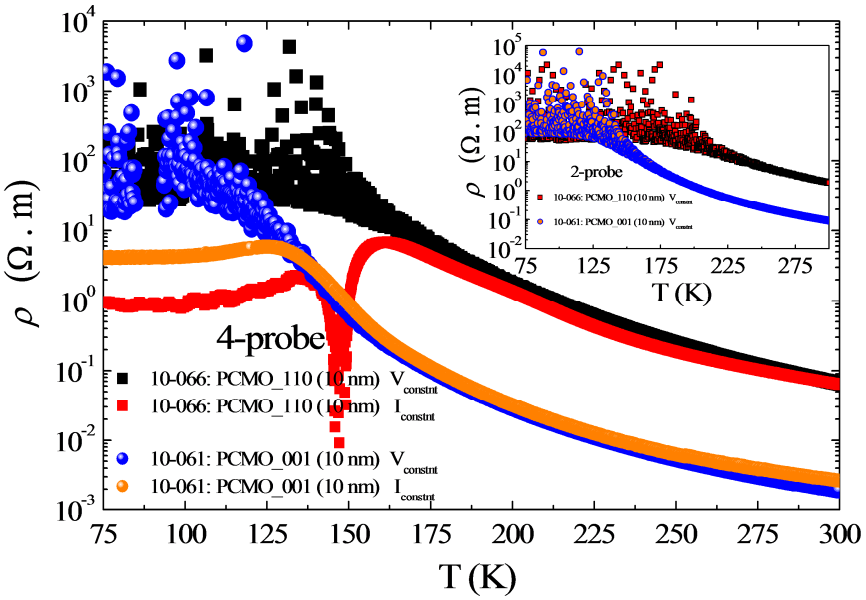

Figure A2.4**:** Comparison of 4-probe resistivity data between PCMO_110 and PCMO_001 (both 10 nm) thin films. Inset show 2-probe data for the same samples.

These measurements show qualitatively similar insulating behavior, with false drop in resistance (with 4-probe current pulsed mode) followed by starting of noisy behavior (with 4-probe and 2-probe constant voltage mode). Moreover, the drop (bend) in resistivity and the starting of noisy behavior appear at the same locations for both samples. However, it is seen that on average PCMO_110 has higher resistivity and above features appear early in the case of PCMO_110 sample if a comparison is made between same thickness values of PCMO_001 samples (see Fig. A2.4 and A2.1b).

A3: Appendix 3

A3.1 Transport characterizations of PCMO at different bias currents

In this appendix, I will briefly discuss the epitaxial stabilization of the ferromagnetic phase and the concomitant suppression of the antiferromagnetic one in PCMO films grown on (110) STO, in contrast to the bulk-like features of samples grown onto (001) STO. Indeed, the origin of the FM insulating (FMI) phase in PCMO is still controversial. Such a combination of magnetic and electronic properties is rare, but it occurs in several other manganites systems too, however in the lower doping regime $x \leq 0.25$, where Jahn–Teller electron-lattice and superexchange interactions are stronger than DE and may result in a FMI ground state sustained by a suitable ordered pattern of e_g orbitals. While the physical mechanism (i.e., the double exchange interaction) that leads to the FMM state in manganites is well known, the reason why an insulating state can persist in a DE system at higher doping, as it occurs in PCMO is less evident. The peculiarity of the insulating state of PCMO is quite spectacular since it adjoins a hidden metallic state, characterized by enormous changes in resistivity [viii] that can be reached either by application of several external perturbations. However, while magnetic or pressure induced transitions seems to be homogeneous (e.g. they involve the whole bulk system), there is some evidence that electric and radiation fields (see section 3.7) may cause transitions in phase-separated regions of the system where nucleation of metallic patches in the form of filaments within the system body have been observed.

Let us start with Fig. A3.1 which is taken from Ref. [ix], where the temperature variation of the resistance of a PCMO (x = 0.3) film deposited on Si (100) is shown for different values of the dc current. Here with increase in current the film showed an I–M transition in the low temperature range. The inset on left shows non-ohmic behavior in I–V curves, while right side inset shows a behavior similar to what we have observed in our thin films (see Fig. A2.1). Here, they interpreted this low temperature noisy behavior to temporal fluctuations between resistive states. Recall that

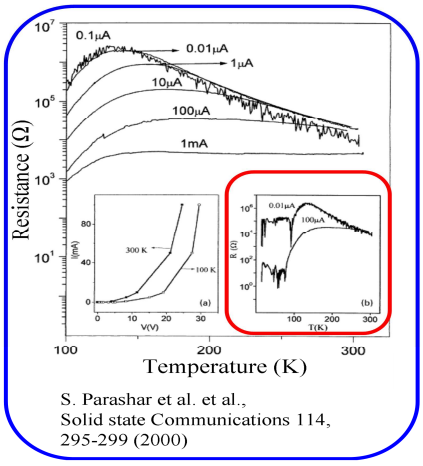

Figure A3.1: R (T) for PCMO sample showing a drop (bend) in resistance for different values of the current, inset shows similar behavior we observed. Taken from [Ref. ix].

the noisy behavior in the R (T) curve below about 130 K is similar to what reported for single crystals below 40K, which was interpreted as temporal fluctuations between low and high resistance states [x].

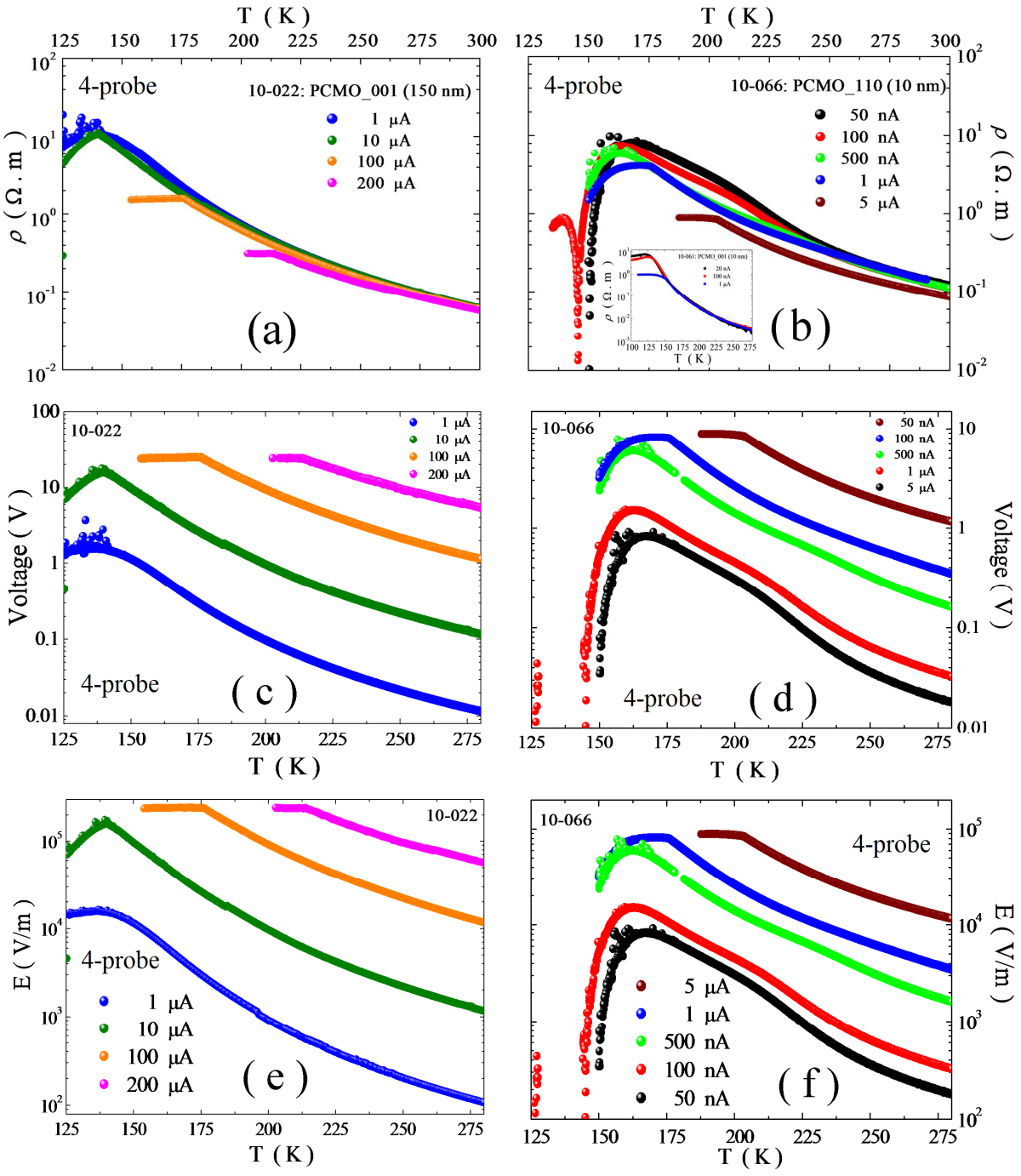

Figure A3.2: Temperature-variation of resistivity for different values of the current, (a) of a PCMO_001 (150 nm) film, and (b) of a PCMO_110 (10 nm) film, inset shows similar data for PCMO_110 (10 nm). Temperature-variation of voltage for, (c) PCMO_001 (150 nm) and (d) PCMO_110 (10 nm) samples respectively. Temperature-variation of electric field for, (e) PCMO_001 (150 nm) and (f) PCMO_110 (10 nm) samples respectively.

In Fig. A3.2, a comparison between PCMO_ (001) and PCMO_ (110) samples is presented. The temperature-variation of resistivity of a PCMO_001 (150 nm) film for different values of the current is shown in Fig. A3.2a, clearly showing that the large current values (upto 200 μA) were not able to decrease resistance. Likewise, in Fig. A3.2b the temperature-variation of resistivity for PCMO_110 (10 nm) film as a function of different values of the current (upto 5 μA) is shown, demonstrating that even a small current value was able to bring decrease in the resistance state. It is important to note the inset which shows that similar current values were not able to decrease resistance of PCMO_001 (10 nm) sample just like thick sample (PCMO_001 (150 nm)). Fig. A3.2c shows temperature-variation of voltage for the PCMO_001 (150 nm) sample, while Fig. A3.2d shows similar plot for PCMO_110 (10 nm) sample, respectively. Finally, Fig. A3.2e and A3.2f show data for electric field (E vs. T) for PCMO_001 and PCMO_110 samples respectively.

This data analysis also show voltage limit of the measuring device (reaching > 10 V) or consequently E > 10^5 V/m. Therefore, we need to further narrow down the spacing between voltage contacts (in this study we used ~ 100 μm) in order to reduce the electric field and concomitantly overcome the compliance issue which appears together with the drop (bend) in resistance with 4-probe. Furthermore, from Fig. A3.2, it also appears that on increasing current I (or current density j), the charge localization process is weakened and progressively eliminated. As displayed in the R (T) curves of Fig. A3.2b, at a temperature around 230 K, a slight difference in the resistance is seen already at low values of current (100 nA) in PCMO_110, while PCMO_001 do not show any change at these values of currents (inset Fig. A3.2b). The same current induced melting of the polarons, slightly below the charge ordering temperature, was reported in thick relaxed films of $Pr_{0.7}Ca_{0.3}MnO_3$ [xi]. We observe, however, that in PCMO_110 (10 nm) the low resistance state is achieved under a very low current (current density) if compared with the one of thick sample (Fig. A3.2a) or with the bulk. Actually, the melting of the polaron solid and a crossover to a large polaron regime of metallic conductivity can be induced by sufficiently high E and j, as extensively reported [xi, xii] since the pioneering work of Asamitsu et al. [x].

Finally, I would like to comment that the transport measurements of this highly complex material PCMO are quite tedious to obtain (in a sense that one has to sit all the day in front of the instruments looking at their front panels for the blinking of compliance indicator). Moreover, in Fig. A3.3, R (T)s for three different PCMO samples are shown, obtained by using 2-probe constant current mode. The initial warming path is shown by

dashed arrows, after 360K a clear increase in the resistance is seen, and the sample never returned back to the initial resistive stage. Therefore it is advisable to not heat too much the sample, specially, if one needs to make a comparison among the low temperatures resistivities. Moreover, it was also observed that the R (T) show a slow increase with time (moths) with respect to the first virgin run (e.g., performed after several months), and sometimes I noticed that the contacts also become diffused (dirty) i.e., clear aging effect. For the better results, however, I recommend long delays (e.g., 500-1000 ms) and the performance of the experiment in one single allotted time (e.g., 10 days) without taking the sample outside the CCR setup.

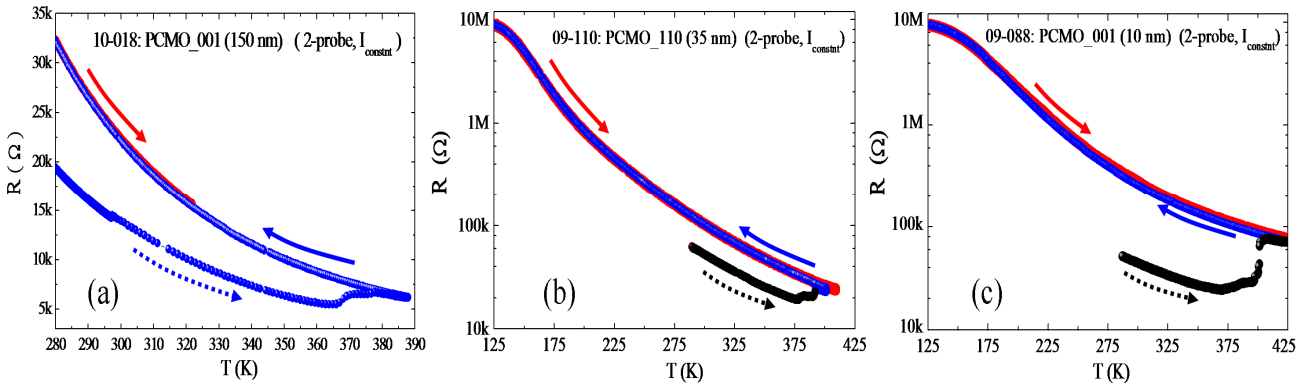

Figure A3.3: Temperature-variation of resistance for showing increase in resistance upon heating, (a) PCMO_001 (150 nm) film, (b) PCMO_110 (35 nm) film, and (c) PCMO_001 (10 nm) sample. Measurements done in 2-probe (constant current) mode.

A3.1 Substrate issue

An important issue concerning possible origin of the photoinduced resistance change is carrier injection from the substrate for films thinner than the absorption length of light. Thus not only the film but also the substrate is optically excited. Hence, the possible change in doping resulting from carrier injection from the substrate is an open point for most experiments on illuminated manganite films with a thickness of several 10 nm. Consequently, all observed effects can, in principle, have their origin either in processes in the substrate or in the film, or in both. To clarify possible origins of the photoconductivity the transport behaviour of bare LAO and NGO substrates (also bare STO substrates) is studied, with the same photon flux and electrode configuration used for the thin film samples. In Fig. A3.4, R (T) for LAO and NGO substrates both in dark and under illuminations are shown. No signs of PC are seen with 4-probe and 2-probe configurations.

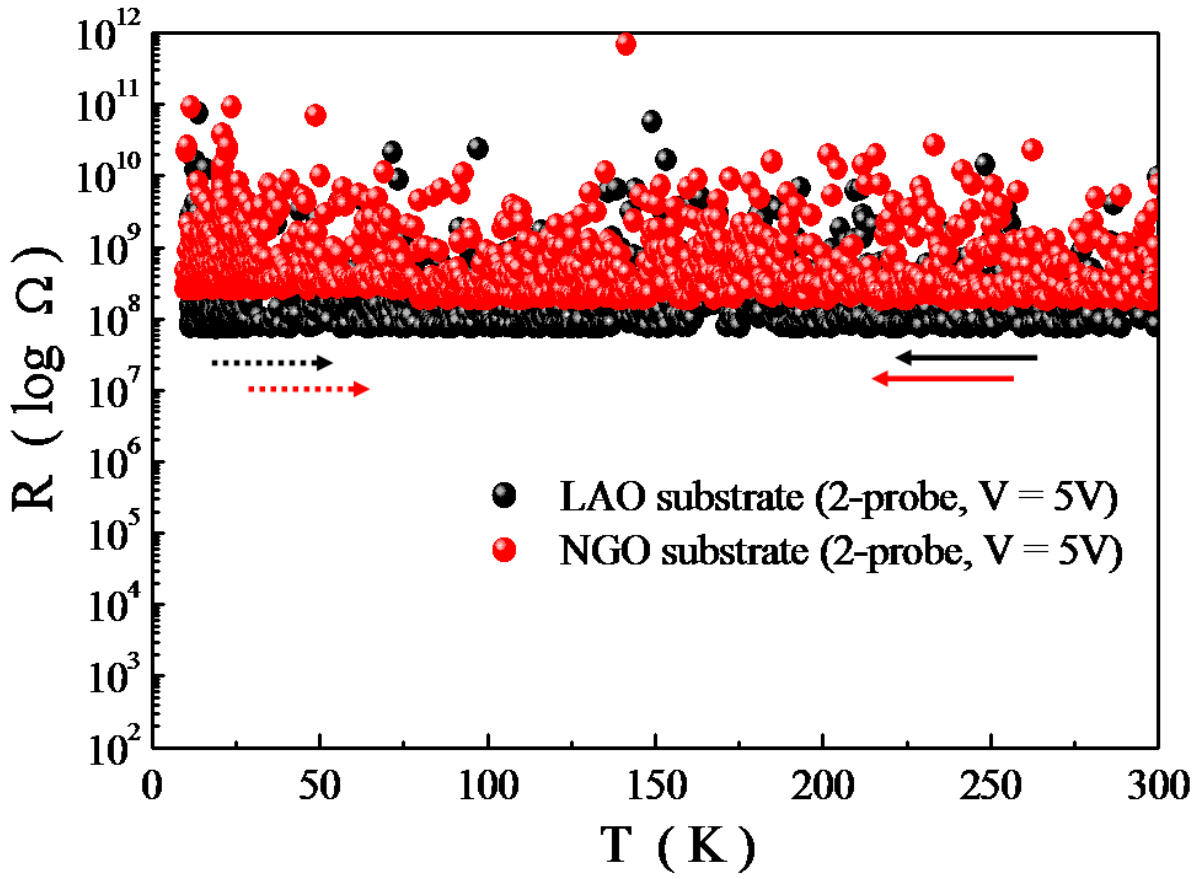

Figure A3.4: Temperature dependence of resistance measured in dark (solid arrows) and under illumination (dashed arrows) for bare, LAO and NGO substrates. The measurements were done in 2-probe constant voltage (V= 5V) mode by resorting to ultrasonic bonding on silver (sputtered) contacts of 0.1 mm apart.

A3.2 Low temperature resistance minima

Here, I would like to briefly discuss the low temperature resistance upturn. The variable temperature dependence of the sheet resistance is a nice tool which can provide further understanding the nature of the scattering in the n-type interfaces. In all the three kinds of heterostructures, in the temperature window of 90 K down to 20 K, is routinely seen a slight upturn in the sheet resistance data. This indicates, there is a possible metal-insulator (M-I) transition in this range.

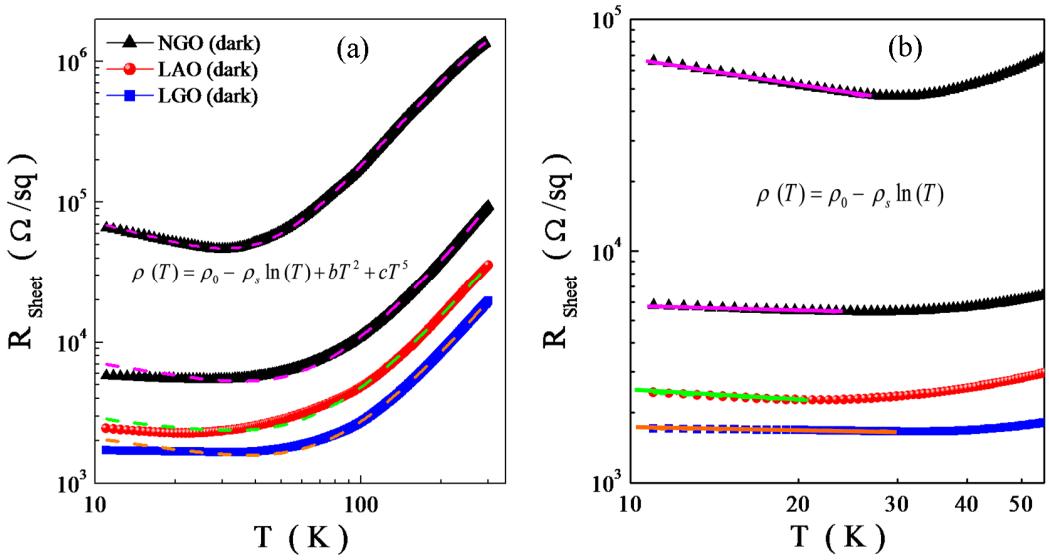

Figure A3.5: The sheet resistance vs. temperature in dark, from top to bottom; (a) of two different NGO/STO samples (black), LAO/STO (Red) and LGO/STO (blue), dashed lines are fits to Eq. A3.2, (b) same data fitted to Eq. A3.1.

This transition which is ascribed to localization could possibly be due to increased scattering effects, e.g., arising from the presence of impurity at the interface (or magnetic ions in the polar layer). Furthermore, under light irradiation a significant reduction of the resistance is seen in this region, where the increment of conductivity suppresses this resistance upturn. The scattering of conduction electrons from magnetic impurities and the presence of resistance minima at low temperatures is a well known phenomena ascribed to Kondo effect. The temperature dependence of the sheet resistance is found to be logarithmic over a wide range of temperature (~ 10 –50 K, see Fig. A3.5b). For a metallic sample having this effect in its resistivity, one can write a formula of the form

$$\rho = \rho_0 - \rho_s \ln (T) \qquad \text{(A3.1)}$$

where ρ_0 is the residual resistance, and ρ_s is the contribution of spin-scattering due to the magnetic impurities. The overall sheet resistance can be described by

$$\rho (T) = \rho_0 - \rho_s \ln (T) + bT^2 + cT^5 \qquad \text{(A3.2)}$$

where the T^2 and T^5 terms are suggestive of electron–electron and electron–phonon scattering, relevant at higher temperatures. The logarithmic term used, is for the low temperature upturn. In Fig. A3.5a, we show fits to Eq. A3.2 for all the three structures. Clearly, NGO sample with high R_{sheet} value shows a very nice fit (dashed line), while there is a slight mismatch seen at low temperature for those samples where the upturn become less evident. Fig. A3.5b shows only the low temperature region, where low temperature resistance upturns are fitted to Eq. A3.1. This result is in consistent with previous reports on oxide interfaces [80].

A4: Appendix 4

A4.1 List of samples characterized by me during this PhD research work

Serial number	Sample name	Substrate	Material (s)
			TMO interfaces
1	10-024	STO (001)	LTO (12 uc)
2	10-043	STO (001)	TiO_2
			NGO
3	08-059	STO (001)	NGO (?? uc)
4	08-081	STO (001)	NGO (07 uc)
5	10-005	STO (001)	NGO (12 uc)
6	10-007	STO (001)	NGO (12 uc)
7	10-021	STO (001)	NGO (11 uc)
8	10-027	STO (001)	NGO (12 uc)
8	10-058	STO (001)	NGO (12 uc)
10	10-067	STO (001)	NGO (12 uc)
11	11-078	STO (001)	NGO (06 uc)
12	11-082	STO (001)	NGO (12 uc)
13	11-097	STO (001)	NGO (12 uc)
			LAO
14	08-020	STO (001)	LAO (04 uc)
15	09-107	STO (001)	LAO (12 uc)
16	10-026	STO (001)	LAO (12 uc)
17	10-057	STO (001)	LAO (17 uc)

Serial number	Sample name	Substrate	Material (s)
18	10-071	STO (001)	LAO (?? uc)
19	10-072	STO (001)	LAO (?? uc)
20	11-079	STO (001)	LAO (12 uc)
21	11-080	STO (001)	LAO (21 uc)
22	11-090	STO (001)	LAO (12 uc)
23	11-093	STO (001)	LAO (12 uc)
24	11-096	STO (001)	LAO (12 uc)
25	11-100	STO (001)	LAO (10 uc)
26	11-102	STO (001)	LAO (05 uc)
27	11-103	STO (001)	LAO (11 uc)
28	11-115	STO (001)	LAO (12 uc)
29	11-116	STO (001)	LAO (12 uc)
			LGO
30	10-010	STO (001)	LGO (12 uc)
31	10-031	STO (001)	LGO (12 uc)
32	10-048	STO (001)	LGO (20 uc)
33	10-054	STO (001)	LGO (12 uc)
34	11-081	STO (001)	LGO (20 uc)
35	11-083	STO (001)	LGO (12 uc)
36	11-084	STO (001)	LGO (20 uc)
37	11-085	STO (001)	LGO (20 uc)
38	11-086	STO (001)	LGO (20 uc)
39	11-088	STO (001)	LGO (12 uc)
40	11-089	STO (001)	LGO (12 uc)
41	11-092	STO (001)	LGO (12 uc)

Serial number	Sample name	Substrate	Material (s)
42	11-095	STO (001)	LGO (12 uc)
43	11-098	STO (001)	LGO (12 uc)
44	11-099	STO (001)	LGO (12 uc)
45	11-110	STO (001)	LGO (12 uc)
46	11-113	STO (001)	LGO (08 uc)
			LMO
47	07-043	STO (001)	LMO
48	LMO-A	STO (001)	LMO
49	LMO-B	STO (001)	LMO
			HTc Superconductors
50	10-001	STO (001)	YBCO
51	10-033	LAO (001)	YBCO
52	10-053	LAO (001)	YBCO
53	10-060	LAO (001)	YBCO
54	08-021	STO (001)	YBCO
			Manganite Multilayers
55	09-010	STO (001)	LSMO/YBCO (top)
56	09-019	STO (001)	YBCO/LSMO (top)
57	08-145	NGO (110)	LSMO(5 uc)/STO(15 uc) top layer
58	08-149	NGO (110)	LSMO(5 uc)/LAO(15 uc) top
59	08-155	NGO (110)	LSMO(5 uc)/PCMO(15 uc) top
56	08-156	NGO (110)	LSMO(4 uc)/PCMO(15 uc) top
57	08-166	NGO (001)	LSMO(4 uc)/PCMO(15 uc) top

Serial number	Sample name	Substrate	Material (s)
			PCMO (Manganites)
58	06-104	STO (001)	PCMO (10 nm)
59	07-102	STO (001)	PCMO (50 nm)
60	08-017	STO (001)	PCMO (11 nm)
61	09-088	STO (001)	PCMO (10 nm)
62	09-110	STO (110)	PCMO (35 nm)
63	09-111	STO (110)	PCMO (35 nm)
64	10-018	STO (001)	PCMO (150 nm)
65	10-020	STO (110)	PCMO (150 nm)
66	10-022	STO (001)	PCMO (150 nm)
67	10-061	STO (001)	PCMO (10 nm)
68	10-066	STO (110)	PCMO (10 nm)
69	09-014	STO (001)	LSMO

Fig. A4.1, showing R vs. number of u.c. at room temperature (300K) for several samples of NGO, LGO and LAO based interfaces grown on STO (001).

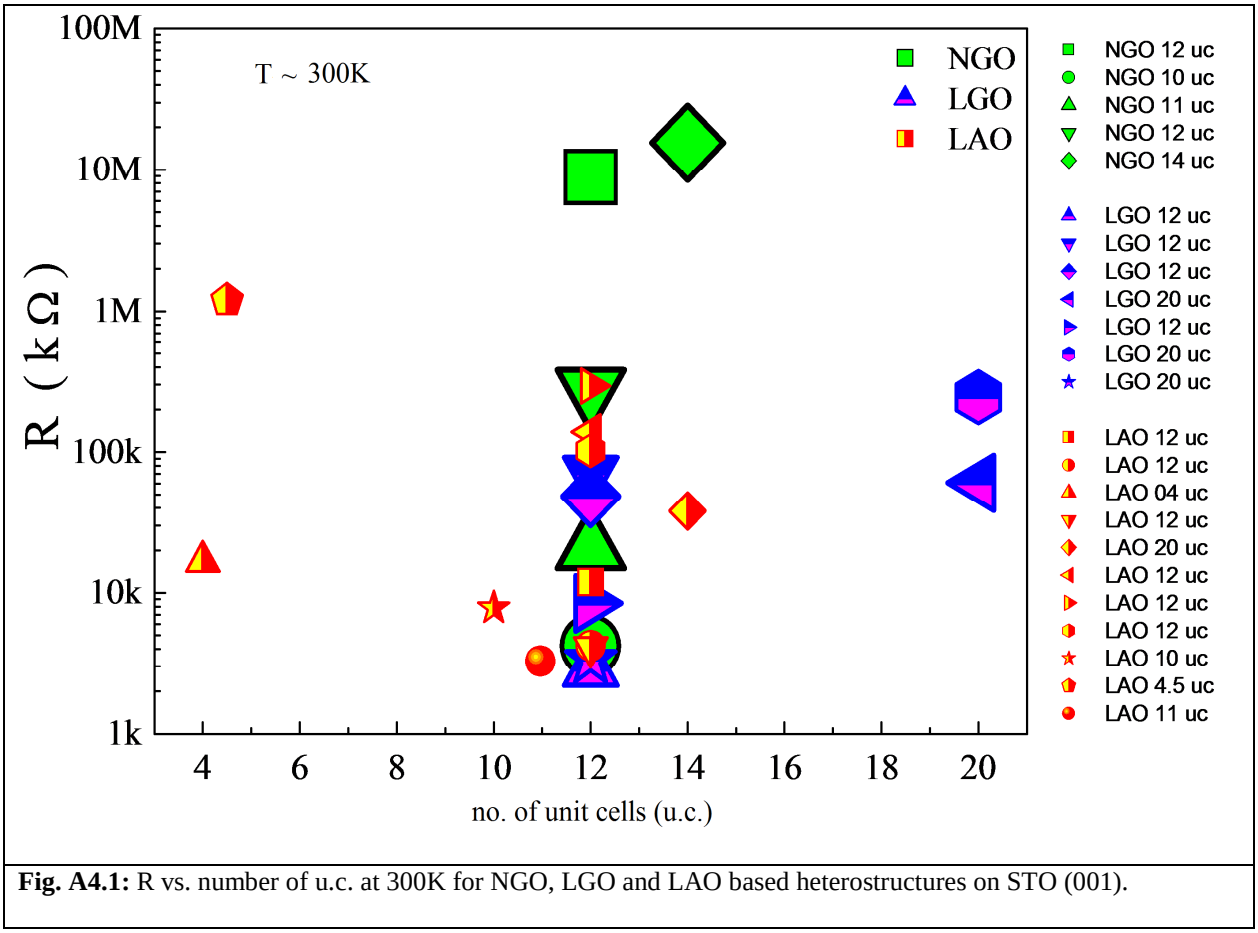

Fig. A4.1: R vs. number of u.c. at 300K for NGO, LGO and LAO based heterostructures on STO (001).

Fig. A4.2, showing R vs. time at room temperature (300K) for two samples each of NGO, LGO and LAO based interfaces grown on STO (001), respectively.

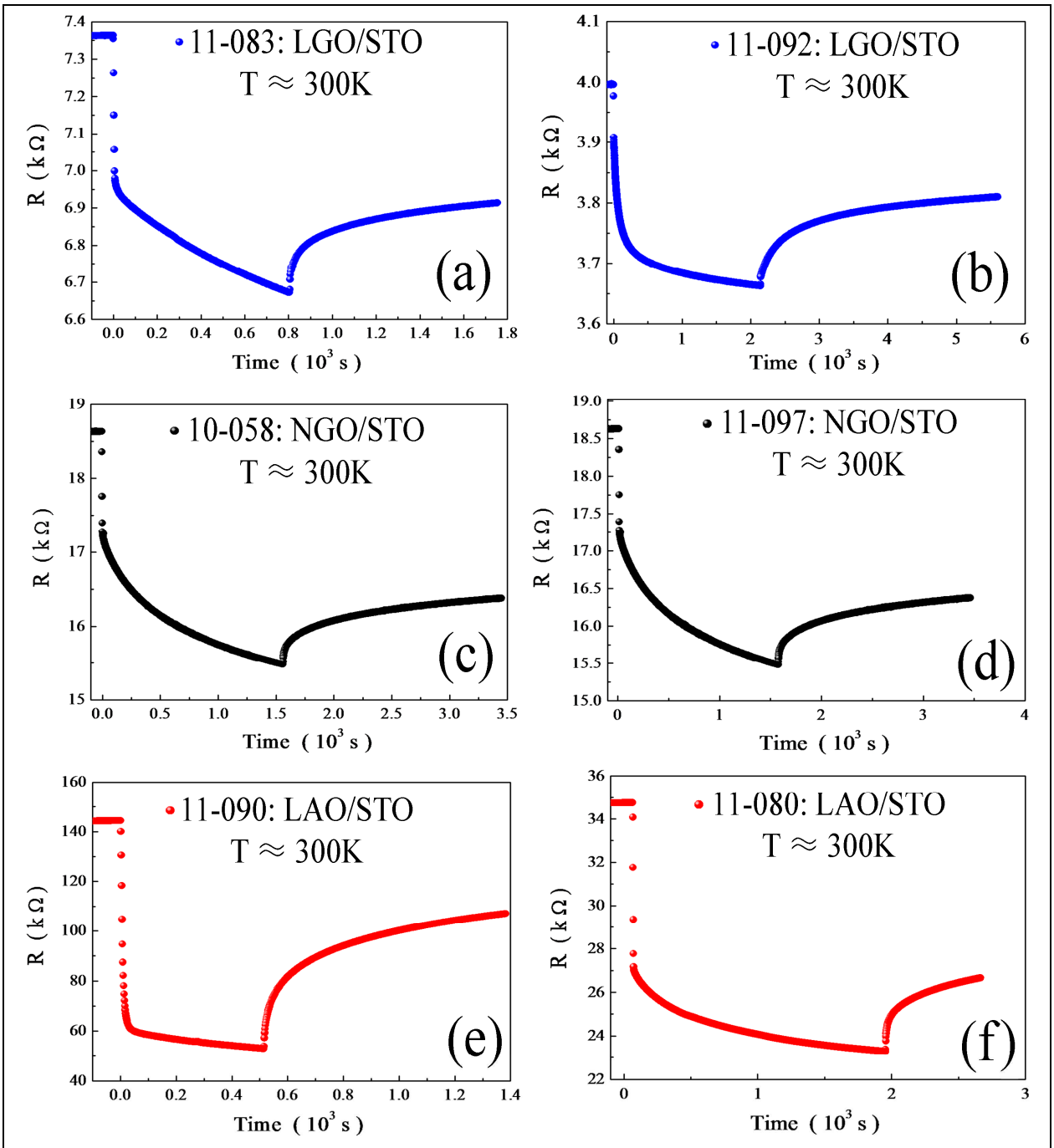

Fig. A4.2: R vs. time at 300K for (a, b) two LGO/STO, (c, d) two NGO/STO, and (e, f) two LAO/STO samples respectively.

A5: Appendix 5

A5.1 Photoinduced phase transition experiment on PCMO

In order to explore this metallic phase claimed in Ref. [xiii], I tried PIPT experiment on 07-102: PCMO_001 (50 nm) sample by selecting infra red (IR) and green wavelengths of the pulsed laser (type: Q-switched (pulsed) Nd:YAG) with power~ 95 mJ/pulse at 1064 nm (IR) and 88 mJ/pulse pulse at 532 nm (green), having repetition rate of 0.1 Hz, respectively, from room temperature down to 150K, but we saw no sign of it. The outcome of this experiment resulted in no change in the resistance except very feeble traces of heating effects in this temperature window (Fig. A5.1).

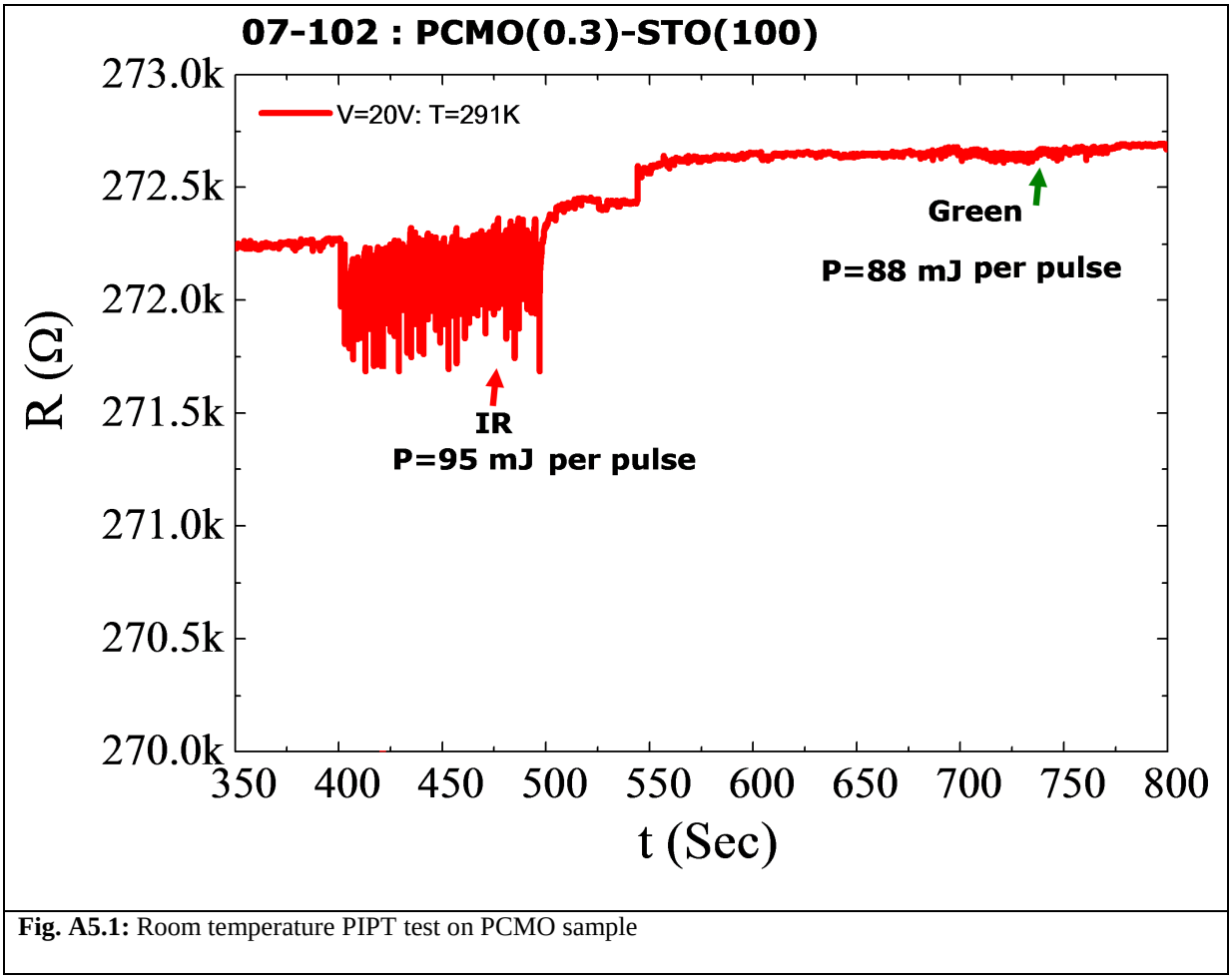

Fig. A5.1: Room temperature PIPT test on PCMO sample

References

[1] A. Ohtomo and H.Y. Hwang. “A high-mobility electron gas at the $LaAlO_3/SrTiO_3$ heterointerface". Nature, 427, 423, (2004)

[2] W. Meevasana, P. D. C. King, R. H. He, S-K. Mo, M. Hashimoto, A. Tamai, P. Songsiriritthigul, F. Baumberger and Z-X. Shen. “Creation and control of a two-dimensional electron liquid at the bare SrTiO3 surface.” Nature materials 2943, 114-118 (2011)

[3] Elbio Dagotto. “Complexity in Strongly Correlated Electronic Systems.” Science309, 257 (2005)

[4] Ariando, X. Wang, G. Baskaran, Z. Q. Liu, J. Huijben, J. B. Yi, A. Annadi, A. Roy Barman, A. Rusydi, S. Dhar, Y. P. Feng, J. Ding, H. Hilgenkamp & T. Venkatesan. “Electronic phase separation at the $LaAlO_3/SrTiO_3$ interface.” Nature Communications 2, 1192 (2011)

[5] Y. Tomioka, A. Asamitsu, H. Kuwahara, Y. Moritomo, and Y. Tokura. “Magnetic-field-induced metal-insulator phenomena in $Pr_{1-x}Ca_xMnO_3$ with controlled charge-ordering instability.” PRB 53, R1689 (1996)

[6] A. Asamitsu, Y. Tomioka, H. Kuwahara, Y. Tokura. “Current switching of resistive states in magnetoresistive manganites.” Nature 388, 50 (1997).

[7] Y. Moritomo, H. Kuwahara, Y. Tomioka, Y. Tokura, “Pressure effects on charge-ordering transitions in Perovskite manganites” Phys. Rev. B 55, 7549 (1997)

[8] M. Fiebig, K. Miyano, Y. Tomioka, and Y. Tokura. “Visualization of the Local Insulator-Metal Transition in $Pr_{0.7}Ca_{0.3}MnO_3$.” Science 280, 1925 (1998).

[9] V. Kiryukhin, D. Casa, J.P. Hill, B. Keimer, A. Vigliante, Y. Tomioka, Y Tokura. “An X-ray-induced insulator–metal transition in a magnetoresistive manganite.” Nature 386, 813 (1997).

[10] Yoshinori Tokura. “Photoinduced Phase Transition: A Tool for Generating a Hidden State of Matter.” J. Phys. Soc. Jpn. 75, 011001 (2006)

[11] H. Ichikawa, S. Nozawa, T. Sato, A. Tomita, K. Ichiyanagi, M. Chollet, L. Guerin, N. Dean, Andrea Cavalleri, S. Adachi, T. Arima, H. Sawa, Y. Ogimoto, M. Nakamura, R. Tamaki, K. Miyano and S. Koshihara.“Transient photoinduced ‘hidden’ phase in a manganite.” Nature materials 10, 101-105 (2011)

[12] A. Rastogi , A. K. Kushwaha , T. Shiyani , A. Gangawar , and R. C. Budhani. “Electrically Tunable Optical Switching of a Mott Insulator–Band Insulator Interface.” Adv. Mater. 22, 4448–4451(2010)

[13] Pavlo Zubko, Stefano Gariglio, Marc Gabay, Philippe Ghosez, and Jean-Marc Triscone. "Interface Physics in Complex Oxide Heterostructures." Annu. Rev. Condens.Matter Phys. 2:141–65 (2011).

[14] G. H. Jonker, J. H. Van Santen, Physica 16, 337 (1950).

[15] D. G. Schlom, L.-Q. Chen, X. Pan, A. Schmehl and M. A. Zurbuchen. "A thin film approach to engineering functionality into oxides." Journal of the American Ceramic Society 91, 2429-2454 (2008).

[16] V.M. Goldschmidt. "Geochemistry", Oxford: Oxford University Press (1958).

[17] J.B. Goodenough. "Magnetism and the chemical bond", New York: Wiley-Interscience (1966).

[18] J L García-Muñoz, J Fontcuberta, M Suaaidi and X Obradors. "Bandwidth narrowing in bulk $L_{2/3}A_{1/3}MnO_3$ magnetoresistive oxides", J. Phys.: Condens. Matter 8, L787 (1996).

[19] Hwang H Y, Cheong S W, Radaelli P G, Marezio M and Batlogg B. "Lattice Effects on the Magnetoresistance in Doped $LaMnO_3$", Phys. Rev. Lett. 75, 914–917 (1995).

[20] P. G. Radaelli, Iannone G, Marezio M, Hwang H Y, Cheong S-W, Jorgensen J D and Argyriou D N. "Structural effects on the magnetic and transport properties of perovskite $A_{1-x}A_x'MnO_3$ (x=0.25, 0.30)", Phys. Rev. B 56, 8265–8276 (1997).

[21] J. M. D. Coey, M. Viret and S. von Molnar. "Mixed valence manganites", Adv. Phys. 48 (2), 167 (1999)

[22] E. Dagotto, T. Hotta and A. Moreo. "Colossal magnetoresistance materials: the key role of phase separation", Physics Reports 344: p. 1-153 (2001).

[23] A. M. Haghiri-Gosnet, J. P. Renard. "CMR manganites: physics, thin films and devices", J. Phys. D: Appl. Phys. 36, R127 (2003).

[24] A. J. Millis. "Theory of CMR Manganites, in Colossal Magnetoresistive oxides", ed. Y. Tokura, Gordon and Breach, London (1999).

[25] H. A. Jahn, E. Teller, Proc. Roy. Soc. A161, 220 (1937).

[26] D I Khomskii. "Role of orbitals in the physics of correlated electron systems", Physica Scripta, 72(5):CC8, (2005).

[27] Y. Tokura and N. Nagaosa. "Orbital Physics in Transition-Metal Oxides", Science, 288 (5465):462-468, (2000).

[28] J. Barratt, M. R. Lees, G. Balakrishnan, D. McK Paul, Appl. Phys. Lett. 68, 424 (1996).

[29] M. Hervieu, A. Barnab_e, C. Martin, A. Maignan, and B. Raveau. "Charge disordering induced by electron irradiation in colossal magnetoresistant manganites". Phys. Rev. B, 60(2):R726-R729, (1999)

[30] S. Blundell, Magnetism in condensed matter, Oxford U.P., New York, (2001).

[31] M. Uehara, S. Mori, C.H. Chen, S.W. Cheong. "Percolative phase separation underlies colossal magnetoresistance in mixed-valent manganites", Nature 399, 560-563 (1999).

[32] D. Saurel, A. Brûlet, A. Heinemann, C. Martin, S. Mercone, C. Simon. "Magnetic field dependence of the magnetic phase separation in $Pr_{1-x}Ca_xMnO_3$ manganites studied by small-angle neutron scattering", Phys. Rev. B 73, 094438 (2006).

[33] von Helmolt R, Wecker J, Holzapfel B, Schultz L and Samwer K. "Giant negative magnetoresistance in perovskitelike $La_{2/3}Ba_{1/3}MnO_x$ ferromagnetic films", Phys. Rev. Lett. 71, 2331–2333 (1993)

[34] A. P. Ramirez. "Colossal magnetoresistance." Journal of Physics: Condensed Matter 9, 8171-8199 (1997).

[35] J. Fontcuberta, B. Martínez, A. Seffar, S. Piñol, J. L. García-Muñoz and X. Obradors. "Colossal Magnetoresistance of Ferromagnetic Manganites: Structural Tuning and Mechanisms." Physical Review Letters, 76 (7): 1122 (1996).

[36] Baibich M N, Broto J M, Fert A, Nguyen Van Dau F, Petroff F, Etienne P, Creuzet G, Friedrich A and Chazelas J. "Giant Magnetoresistance of (001)Fe/(001)Cr Magnetic Superlattices", Phys. Rev. Lett. 61, 2472-2475 (1988).

[37] Gr¨unberg P, Schreiber R, Pang Y, Brodsky M B and Sowers H. "Layered Magnetic Structures: Evidence for Antiferromagnetic Coupling of Fe Layers across Cr Interlayers", Phys. Rev. Lett. 57, 2442-2445 (1986).

[38] M. Bowen, M. Bibes, A. Barthelemy, J. P. Contour, A. Anane, Y. Lemaitre and A. Fert. "Nearly total spin polarization in $La_{2/3}Sr_{1/3}MnO_3$ from tunneling experiments". Applied Physics Letters 82(2): 233-235 (2003).

[39] M. Gajek, M. Bibes, S. Fusil, K. Bouzehouane, J. Fontcuberta, A. Barthélémy and and A. Fert. "Tunnel junctions with multiferroic barriers", Nature Materials 6, 296 – 302 (2007).

[40] Kathrin Dörr. "Ferromagnetic manganites: spin-polarized conduction versus competing interactions." J. Phys. D: Appl. Phys. 39, R125–R150 (2006).

[41] R. Werner, A. Yu. Petrov, L. Alvarez Miño, R. Kleiner, D. Koelle, and B. A. Davidson. "Improved tunneling magnetoresistance at low temperature in manganite junctions grown by molecular beam epitaxy", Appl. Phys. Lett. 98, 162505 (2011)

[42] Monsma D J, Lodder J C, Popma Th J A and Dieny B. "Perpendicular hot electron spin-valve effect in a new magnetic field sensor: The spin-valve transistor." Phys. Rev. Lett. 74, 5260-5263 (1995).

[43] Dijken S van, Jiang X and Parkin S S P. "Giant magnetocurrent exceeding 3400% in magnetic tunnel transistors with spin-valve base layers." Appl. Phys. Lett. 83, 951 (2003).

[44] Y. Ohno, D. K. Young, B. Beschoten, F. Matsukura, H. Ohno & D. D. Awschalom. "Electrical spin injection in a ferromagnetic semiconductor heterostructure", Nature 402, 790-792 (1999).

[45] Dmitry V Efremov, Jeroen Van Den Brink, and Daniel I Khomskii. "Bond- versus site-centred ordering and possible ferroelectricity in manganites." Nat Mater, 3(12):853-856 (2004).

[46] A. Daoud-Aladine, J. Rodríguez-Carvajal, L. Pinsard-Gaudart, M. T. Fernández-Díaz, and A. Revcolevschi. "Zener Polaron Ordering in Half-Doped Manganites", PRL 89, 097205 (2002).

[47] H. A. Kramers , "L'interaction Entre les Atomes Magnétogènes dans un Cristal ParamagnétiquePhysica 1." 182 (1934).

[48] P. W. Anderson. "Antiferromagnetism. Theory of superexchange interaction", Phys. Rev. 79, 350-356 (1950).

[49] C. Zener. "Interaction between the d-Shells in the Transition Metals. II. Ferromagnetic Compounds of Manganese with Perovskite Structure", Physical Review 82(3), 403 (1951).

[50] P. W. Anderson and H. Hasegawa, "Considerations on Double Exchange", Physical Review 100(2), 675 (1955).

[51] W. Westhäuser, S. Schramm, J. Hoffmann and C. Jooss. "Comparative study of magnetic and electric field induced insulator-metal-transitions in $Pr_{1-x}Ca_xMnO_3$ films", Eur. Phys. J. B 53, Number 3, 323-331 (2006).

[52] Ryoichi Kajimoto, Hidenori Mochizuki and Hideki Yoshizawa. "Ferromagnetic insulating phase in $Pr_{1-x}Ca_xMnO_3$", Physica B: Condensed Matter, Volumes 329-333, Part 2, Pages 738-739 (2003); J Geck, P Wochner, S Kiele, R Klingeler, A Revcolevschi, M v Zimmermann, B Büchner and P Reutler. "Orbital order induced ferromagnetic insulating properties." 2004 New J. Phys. 6, 152 (2004).

[53] P.-G. de Gennes."Effects of Double Exchange in Magnetic Crystals", Phys. Rev. 118, 141–154 (1960)

[54] Z. Jirak, S. Krupicka, Z. Simsa, M. Dlouha, and S. Vratislav. "Neutron diffraction study of $Pr_{1-x}Ca_xMnO_3$ perovskites", J. Magn. Magn.Mat. 53, 153 (1985).

[55] P. Chaudhari, R.H. Koch, R.B. Laibowitz, T.R. McGuire, and R.J. Gambino. "Critical-Current Measurements in Epitaxial Films of $YBa_2Cu_3O_{7-x}$ Compound". Phys. Rev. Lett. 58, 2684 (1987)

[56] M. Kawasaki, K. Takahashi, T. Maeda, R. Tsuchiya, M. Shinohara, O. Ishiyama, T. Yonezawa, M. Yoshimoto, and H. Koinuma. "Atomic Control of the $SrTiO_3$ Crystal Surface", Science 266, 1540 (1994).

[57] Gertjan Koster, Guus Rijnders, Dave H.A. Blank , Horst Rogalla. "Surface morphology determined by (001) single-crystal SrTiO3 termination", Physica C 339, 215 (2000).

[58] O.N. Tufte and P.W. Chapman. "Electron Mobility in Semiconducting Strontium Titanate", Phys. Rev.155, 796 (1966).

[59] A. Bhattacharya, M. Eblen-Zayas, N.E. Staley, W.H. Huber, and A.M. Goldman."Micromachined $SrTiO_3$ single crystals as dielectrics for electrostatic doping of thin films", Appl. Phys. Lett., 85, 997 (2004)

[60] H.-M. Christen, J. Mannhart, E.J. Williams, and C. Gerber. "Dielectric properties of sputtered $SrTiO_3$ films", Phys. Rev. B 49, 12095 (1994).

[61] M. Lippmaa, N. Nakagawa, and M. Kawasaki. “Dielectric Properties of Homoepitaxial SrTiO3 Thin Films Grown in the Step-Flow Mode”, Journal of Electroceramics 4, 365 (2000).

[62] E. Sawaguchi, A. Kikuchi, and Y. Kodera. “Dielectric Constant of Strontium Titanate at Low Temperatures”. J. Phys. Soc. Japan 17, 1666 (1962).

[63] J. Xing, K. Zhao, H. B. Lu, X. Wang, G. Z. Liu, K. J. Jin, M. He, C. C. Wang, and G. Z. Yang. “Visible-blind, ultraviolet-sensitive photodetector based on SrTiO3 single crystal”, Optics letters 32, 2526 (2007)

[64] R.W. Simon, C.E. Platt, A.E. Lee, G.S. Lee, K.P. Daly, M.S. Wire, and J.A. Luine. “Low-loss substrate for epitaxial growth of high-temperature superconductor thin films."APL, 53, 2677(1988).

[65] H. Lehnert, H. Boysen, J. Schneider, F. Frey, D. Hohlwein, P. Radaelli, and H. Ehrenberg. “A powder diffraction study of the phase transition in LaAlO3". Z. Kristallogr., 412, 536, 2000.

[66] S.A. Hayward, F.D. Morrison, S.A.T. Redfern, E.K.H. Salje, J.F. Scott, K.S. Knight, S. Tarantino, A.M. Glazer, V. Shuvaeva, P. Daniel, M. Zhang, and M.A. Carpenter. “Transformation processes in LaAlO3: Neutron diffraction, dielectric, thermal, optical, and Raman studies". Phys. Rev. B, 72, 054110, 2005.

[67] D. de Ligny and P. Richet. “High-temperature heat capacity and thermal expansion of SrTiO3 and SrZrO3 perovskites". Phys. Rev. B, 53, 3013, 1996.

[68] B.C. Chakoumakos, D.G. Schlom, M. Urbanik, and J. Luine. “Thermal expansion of LaAlO3 and (La,Sr)(Al,Ta)O3, substrate materials for superconducting thin-film device applications". Journ. Appl. Phys., 83, 1979, 1998.

[69] P. Delugas, V. Fiorentini, and A. Filippetti. “Dielectric properties and long wavelength optical modes of the high-k oxide LaAlO3". Phys. Rev. B, 71, 134302 (2005).

[70] P. W. Tasker. “The stability of ionic crystal surfaces”, J. Phys. C 12, 4977 (1979)

[71] Claudine Noguera. “Polar oxide surfaces”, J. Phys: Condens. Matter 12, 367 (2000).

[72] Ariana Pojani, Fabio Finocchi, Claudine Noguera. “Polarity on the SrTiO 3 (111) and (110) surfaces”, Surface Science 442, 179 (1999).

[73] Charles B. Duke. “Semiconductor Surface Reconstruction: The Structural Chemistry of Two-Dimensional Surface Compounds”, Chem. Rev. 96, 1237 (1996).

[74] N. Nakagawa, H.Y. Hwang, and D.A. Muller. “Why some interfaces cannot be sharp". Nature Materials, 5, 204 (2006).

[75] G.A. Baraff, J.A. Appelbaum, and D.R. Hamann. “Self-Consistent Calculation of the Electronic Structure at an abrupt GaAs-Ge Interface". Phys. Rev. Lett., 38, 237 (1976).

[76] W.A. Harrison, E.A. Kraut, J.R. Waldrop, and R.W. Grant. “Polar heterojunction interfaces". Phys. Rev. B, 18, 4402 (1978).

[77] S. Okamoto and A.J Millis. “Electronic reconstruction at an interface between a Mott insulator and aband insulator". Nature, 428, 630 (2004).

[78] S. Okamoto and A.J Millis. “Theory of Mott insulator-band insulator heterostructures". Phys. Rev. B, 70, 075101 (2004)

[79] S Thiel, G Hammerl, A Schmehl, CW Schneider, and J Mannhart. “Tunable quasi-two-dimensional electron gases in oxide heterostructures”. Science 313(5795):1942-1945 (2006).

[80] A Brinkman, M Huijben, M Van Zalk, J Huijben, U Zeitler, J. C Maan, W. G Van Der Wiel, G Rijnders, D. H. A Blank, and H Hilgenkamp. “Magnetic effects at the interface between non-magnetic oxides”. Nat Mater, 6(7):493-496 (2007).

[81] N Reyren, S Thiel, A. D Caviglia, L. F Kourkoutis, G Hammerl, C Richter, C. W Schneider, T Kopp, A.-S Ruetschi, D Jaccard, M Gabay, D. A Muller, J.-M Triscone, and J Mannhart. “Superconducting interfaces between insulating oxides”. Science, 317(5842):1196-1199 (2007).

[82] A. D Caviglia, S Gariglio, N Reyren, D Jaccard, T Schneider, M Gabay, S Thiel, G Hammerl, J Mannhart, and J.-M Triscone. “Electric field control of the $LaAlO_3/SrTiO_3$ interface ground state”, Nature, 456(7222):624-627 (2008).

[83] A. Kalabukhov, R. Gunnarsson, J. Borjesson, E. Olsson, T. Claeson, and D. Winkler, Physical Review B 75, 121404 (2007).

[84] Yunzhong Chen, N. Pryds, J. E. Kleibeuker, G. Koster, J. Sun, E. Stamate, B. Shen, G. Rijnders, and Søren Linderoth. “Metallic and Insulating Interfaces of Amorphous SrTiO3-Based Oxide Heterostructures.” Nano Lett. 11, 3774–3778 (2011)

[85] M. Esposito, M. Bator, M. Döbeli, T. Lippert, C. W. Schneider, and A. Wokaun. “Negative ions: The overlooked species in thin film growth by pulsed laser deposition” APL 99, 191501 (2011)

[86] C. W. Schneider, M. Esposito, I. Marozau, K. Conder, M. Doebeli, Yi Hu, M. Mallepell, A. Wokaun, and T. Lippert. “The origin of oxygen in oxide thin films: Role of the substrate.” APL97, 192107 (2010)

[87] Maurice J-L, Carr´et´ero C, CasanoveM-J, Bouzehouane K, Guyard S, Larquet ´E and Contour J-P. “Electronic conductivity and structural distortion at the interface between insulators SrTiO3 and LaAlO3”, Phys. Status Solidi a 203, 2209 (2006).

[88] Vonk V, Huijben M, Driessen K J I, Tinnemans P, Brinkman A, Harkema S and Graafsma H. “Interface structure of SrTiO3/LaAlO3 at elevated temperatures studied in situ by synchrotron x rays”, Phys. Rev. B 75, 235417 (2007)

[89] P. R. Willmott et al. “Structural basis for the conducting interface between $LaAlO_3$ and $SrTiO_3$”, Phys. Rev. Lett. 99, 155502 (2007)

[90] Scott A. Chambers. “Understanding the mechanism of conductivity at the $LaAlO_3/SrTiO_3$(001) interface.” Surface Science 605, 1133-1140 (2011)

[91] C. Cantoni, J. Gazquez, F. Miletto Granozio, M. P. Oxley, M. Varela, A. R. Lupini, S. J. Pennycook,C. Aruta, U. Scotti di Uccio, P. Perna, D. Maccariello. “Electron transfer and ionic displacements at the origin of the 2D electron gas atthe LAO/STO interface: Direct measurements with atomic-column spatial resolution.” Unpublished.

[92] D. Dijkkamp, T. Venkatesan, X. D. Wu, S. A. Shaheen, N. Jisrawi, Y. H. Min-Lee, W. L. Mclean, M. Croft, Appl. Phys. Lett. **51**, 619 (1987).

[93] A. Inam, M. S. Hegde, X. D. Wu, T. Venkatesan, P. England, P. F. Miceli, E. W. Chase, C. C. Chang, J.-M. Tarascon, J. B. Wachtman, *Appl. Phys. Lett*. **53**, 908 (1988).

[94] D.B. Chrisey, G.K. Hubler, Pulsed laser deposition of thin films, John Wiley & Sons, New York (1994).

[95] C. Aruta, S. Amoruso, R. Bruzzese, X. Wang, D. Maccariello, F. Miletto Granozio, and U. Scotti di Uccio. "Pulsed laser deposition of SrTiO3 /LaGaO3 and SrTiO3 /LaAlO3: Plasma plume effects," APL 97, 252105 (2010)

[96] Alessia Sambri, "Pulsed laser deposition of complex transition metal oxides: plume expansion and film growth"-PhD Thesis, Universita degli Studi di Napoli Federico II, 2007

[97] Milan Radović, "Low dimensional Ti-oxide based structures: surfaces, interfaces and ultrathin films of $SrTiO_3$ and TiO_2"-PhD Thesis, Universita degli Studi di Napoli Federico II, 2008

[98] P. J. Dobson N. Norton J. H. Neave, B. A. Joyce, "Dynamics of film growth of GaAs by MBE from Rheed observations" Applied Physics A: Materials Science & Processing, 31:1, (1983).

[99] J. M. Van Hove, P. Pukite, P. I. Cohen, and C. S. Lent, "Rheed streaks and instrument response", Journal of Vacuum Science and Technology A: Vacuum, Surfaces, and Films, 1(2):609-613, 1983.

[100]Yoshinori Konishi, Zhong Fang, Makoto Izumi, Takashi Manako, Masahiro Kasai, Hideki Kuwahara, Masashi Kawasaki, Kiyoyuki Terakura and Yoshinori Tokura. "Orbital-State-Mediated Phase-Control of Manganites." J. Phys. Soc. Jpn. 68, 3790 (1999)

[101] A. Geddo Lehmann, F. Congiu, N. Lampis, F. Miletto Granozio, P. Perna, M. Radovic, and U Scotti di Uccio, PRB 82, 014415 (2010)

[102] F. Ricci, M. F. Bevilacqua, F. Miletto Granozio, and U. Scotti di Uccio, Phys. Rev. B 65 (2002) 155428

[103] K. Vijaya Sarathy, S. Parashar, A.R. Raju and C.N.Rao. "Mechanism of hopping conduction in charge-ordered rare earth manganites", Solid State Sciences 4, 353 (2002)

[104] N.F. Mott. "Metal-Insulator Transitions", Taylor and Francis, Londen, 1990

[105] Coey J M D, Viret M, Ranno L and Ounadjela K. "Electron localization in mixed-valence manganites", Phys. Rev. Lett. 75, 3910 (1995)

[106] N.F. Mott, Conduction in Non-Crystalline Materials, Clarendon Press, Oxford (1993).

[107] N.F. Mott. "Conduction in glasses containing transition metal ions", J. Non-Cryst. Solids **1**, 1-17 (1968).

[108] S. Schramm, J. Hoffmann and Ch. Jooss, J. Phys.: Condens. Matter 20 (2008) 395231.

[109] Ch. Jooss, L. Wu, T. Beetz, R. F. Klie, M. Beleggia, M. A. Schofield, S. Schramm, J. Hoffmann, and Y. Zhu, Proc. Natl. Acad. Sci. U. S. A. 104, 13597 (2007).

[110] Goodenough, J.B., Zhou, J.S.. "Condensed-matter physics - New forms of phase segregation", Nature **386**, 229 - 230 (1997)

[111] N. Biškup, A. de Andrés, and J. L. Martinez,"Origin of the colossal dielectric response of $Pr_{0.6}Ca_{0.4}MnO_3$." PRB 72, 024115 (2005)

[112] Silvana Mercone, Alexandre Wahl, Alain Pautrat, Michaël Pollet, and Charles Simon, "Anomaly in the dielectric response at the charge-orbital-ordering transition of Pr0.67Ca0.33MnO3." PRB 69, 174433 (2004)

[113] Claudy Rayan Serrao, A Sundaresan and C N R Rao. "Multiferroic nature of charge-ordered rare earth manganites." J. Phys.: Condens. Matter **19,** 496217 (2007)

[114] V. G. Prokhorov, G. G. Kaminsky, V. S. Flis, and Young Pak Lee. "Temperature dependence of resistance of $Pr_{0.65}Ca_{0.35}MnO_3$ films prepared by pulsed laser deposition." Low Temp. Phys**.** 25, 792 (1999)

[115] Y. P. Lee, V. G. Prokhorov , J. Y. Rhee, K. W. Kim, G. G. Kaminsky and V. S. Flis. "The controlled charge ordering and evidence of the metallic state in $Pr_{0.65}Ca_{0.35}MnO_3$ films." J. Phys.: Condens. Matter 12, L133-L138 (2000)

V. G. Prokhorov, K. W. Kim, and Y. P. Lee, "Transport of Carriers in Perovskite Oxides: Manganites, Cobaltites, Cuprates." Journal of Korean Physical Society 36, 398 (2000).

V.G. Prokhorov, G.G. Kaminsky, V.S. Flis, Y.P. Lee, K.W. Kim, I.I. Kravchenko. "Influence of charge ordering and phase separation on transport properties of $Pr_{0.65}Ca_{0.35}MnO_3$ films." Physica B: Condensed Matter 307, 239-246 (2001)

[116] R. Laiho, K. G. Lisunov, E. Lahderanta, V. N. Stamov and V. S. Zakhvalinskii, J. Phys.: Condens. Mater 13 (2001) 1233

[117] S. Parashar, E.E. Ebenso, A.R. Raju, C.N.R. Rao, "Insulator–metal transitions induced by electric and magnetic fields, in thin films of charge-ordered $Pr_{1-x}Ca_xMnO_3$." Solid State Communications 114, 295–299 (2000)

[118] K. Miyano, T. Tanaka, Y. Tomioka, and Y. Tokura, Phys. Rev. Lett. **78**, 4257 (1997).

[119] Matteo Rini, R. Tobey, N. Dean, J. Itatani, Y. Tomioka, Y. Tokura, R. W. Schoenlein and Andrea Cavalleri. "Control of the electronic phase of a manganite by mode-selective vibrational excitation." Nature **449**, 72-74 (2007)

[120] D. Polli, M. Rini, S. Wall, R. W. Schoenlein, Y. Tomioka, Y. Yokura, G. Cerullo, and A. Cavalleri. "Coherent orbital waves in the photo-induced insulator–metal dynamics of a magnetoresistive manganite." Nature materials 6, 643-647 (2007)

[121] R. Cauro, A. Gilabert, J. P. Contour, R. Lyonnet, M.-G. Medici, J.-C. Grenet, C. Leighton, and Ivan K. Schuller. "Persistent and transient photoconductivity in oxygen-deficient $La_{2/3}Sr_{1/3}MnO_{3-\delta}$ thin films." PRB 63, 174423 (2001)

[122] E Beyreuther, A Thiessen, S Grafström, K. Dörr and L M Eng. "Large photoconductivity of oxygen-deficient $La_{0.7}Ca_{0.3}MnO_3/SrTiO_3$ heterostructures." J. Phys.: Condens. Matter 22, 175506 (2010)

[123] A. Ohtomo and H.Y. Hwang. "A high-mobility electron gas at the $LaAlO_3/SrTiO_3$ heterointerface". Nature, 427, 423, (2004)

[124] S. Thiel, G. Hammerl, A. Schmehl, C. W. Schneider, and J. Mannhart, Tunable Quasi-Two-Dimensional Electron Gases in Oxide Heterostructures, Science 313 (2006) 1942-1945

[125] S. A. Pauli and P. R. Willmott, Conducting interfaces between polar and non-polar insulating perovskites, J. Phys.: Condens. Matter 20 (2008) 264012-(1-9)

[126] W. Siemons et al., Origin of Charge Density at LaAlO3 on SrTiO3 Heterointerfaces: Possibility of Intrinsic Doping, Phys. Rev. Lett. 98 (2007) 196802-(1-4);

[127] Wolter Siemons, Gertjan Koster, Hideki Yamamoto, Theodore H. Geballe, Dave H. A. Blank, and Malcolm R. Beasley, "Experimental investigation of electronic properties of buried heterointerfaces of $LaAlO_3$ on $SrTiO_3$". PRB 76, 155111 (2007)

[128] A. Brinkmanet al., Magnetic effects at the interface between non-magnetic oxides, Nature Mater. 6 (2007) 493-496

[129] A. Kalabukhov, R. Gunnarsson, J. Börjesson, E. Olsson, T. Claeson, and D. Winkler, Effect of oxygen vacancies in the SrTiO3 substrate on the electrical properties of theLaAlO3⁄SrTiO3 interface, Phys. Rev. B 75 (2007) R121404-(1-4)

[130] M. Huijben, A. Brinkman, G. Koster, G. Rijnders, H. Hilgenkamp, and D. H. A. Blank, Structure–Property Relation of SrTiO3/LaAlO3 Interfaces, Adv. Mater. 21 (2009) 1665-1677

[131] M. Basletić, J.-L. Maurice, C. Carrétéro, G. Herranz, O. Copie, M. Bibes, E. Jacquet, K. Bouzehouane, S. Fusil, and A. Barthélémy, Mapping the spatial distribution of charge carriers in LaAlO3/SrTiO3 heterostructures, Nature Mater. 7 (2008) 621-625.

[132] J. Goniakowski, F. Finocchi, and C. Noguera, Polarity of oxide surfaces and nanostructures, Rep. Prog. Phys. 71 (2008) 016501-(1-55).

[133] P. Perna, D. Maccariello, M. Radovic, U. Scotti di Uccio, I. Pallecchi, M. Codda, D. Marré, C. Cantoni, J. Gazquez, M. Varela, S. Pennycook, and F. Miletto Granozio, Conducting interfaces between band insulating oxides: The LaGaO3 /SrTiO3 heterostructure, Appl. Phys. Lett. 97, 152111 (2010)

[134] C. Aruta, S. Amoruso, R. Bruzzese, X. Wang, D. Maccariello, F. Miletto Granozio, and U. Scotti di Uccio, Pulsed laser deposition of SrTiO3 /LaGaO3 and SrTiO3 /LaAlO3: Plasma plume effects, Appl. Phys. Lett. 97 (2010) 252105-(1-3)

[135] G. Koster, B. L. Kropman, G. J. H. M. Rijnders, D. H. A. Blank, and H. Rogalla, Quasi-ideal strontium titanate crystal surfaces through formation of strontium hydroxide, Appl. Phys. Lett. 73, (1998) 2920.

[136] L.Q. Jiang**,** J. Guo, H. Liu, M. Zhu, X. Zhou, P. Wu, and C. Li, "Prediction of lattice constant in cubic perovskites". J. Phys. Chem. Solids, vol. 67, p. 1531, 2006.

[137] U. Scotti di Uccio, C. Cantoni, A. Gadaleta, D. Maccariello, D. Marré, F. Miletto Granozio, I. Pallecchi, D. Paparo, P. Perna, M. Riaz, and C. Aruta, Photoconductivity of interfaces between oxide band insulators hosting a 2-dimensional electron gas: the case of NdGaO3/SrTiO3 unpublished.

[138] A. Savoia, D. Paparo, P. Perna, Z. Ristic, M. Salluzzo, F. Miletto Granozio, U. Scotti di Uccio, C. Richter, S. Thiel, J. Mannhart, and L. Marrucci, Polar catastrophe and electronic reconstructions at the LaAlO3/SrTiO3 interface: evidence from optical second harmonic generation, Phys. Rev. B 80, (2009) 075110; S. Amoruso,C. Aruta, R. Bruzzese, X. Wang, and U. Scotti di Uccio, Substrate heating influence on the deposition rate of oxides during pulsed laser deposition in ambient gas, Appl. Phys. Lett. 98, (2011) 101501.

[139]A. Kalabukhov, Yu. A. Boikov, I.T.Serenkov,V.I.Sakharov, J.B¨orjesson, N. Ljustina, E. Olsson,D.Winkler and T. Claeson, Eur. Phys. Lett. **93** 37001(2011)

[140] C. Aruta, S. Amoruso, R. Bruzzese, X. Wang, D. Maccariello, F. Miletto Granozio, and U. Scotti di Uccio Appl. Phys. Lett. **97**, 252105 (2010)

[141] C. Aruta, S. Amoruso, G. Ausanio, R. Bruzzese, E. Di Gennaro, M. Lanzano, F. Miletto Granozio, Muhammad Riaz, U. Scotti di Uccio, and X. Wang, "Conductive $LaAlO_3/SrTiO_3$ and $LaGaO_3/SrTiO_3$ interfaces at high oxygen pressure in the shock-wave regime of pulsed laser deposition." in preparation

[142] W. Schneider, M. Esposito, I. Marozau, K. Conder, M. Doebeli, Yi Hu, M. Mallepell, A. Wokaun, and T. Lippert,
Appl. Phys. Lett. **97**, 192107 (2010)

[143] Yunzhong Chen, Nini Pryds, Jos´ee E. Kleibeuker, Gertjan Koster, Jirong Sun, Eugen Stamate, Baogen Shen,
Guus Rijnders, and Søren Linderoth Nano Letters **11**,3774 (2011)

[144] Wolter Siemons, Gertjan Koster, Hideki Yamamoto, Theodore H. Geballe, Dave H. A. Blank, and Malcolm R. Beasley, "Experimental investigation of electronic properties of buried heterointerfaces of $LaAlO_3$ on $SrTiO_3$". PRB 76, 155111 (2007)

[145] Wolter Siemons, Mark Huijben, Guus Rijnders, Dave H. A. Blank, Theodore H. Geballe, Malcolm R. Beasley, and Gertjan Koster, "Dielectric-permittivity-driven charge carrier modulation at oxide interfaces" PRB 81, 241308R (2010)

[146] C. W. Bark, D. A. Felker, Y. Wang, Y. Zhang, H. W. Jang, C. M. Folkman, J. W. Park, S. H. Baek, H. Zhou, D. D. Fong, X. Q. Pan, E. Y. Tsymbal, M. S. Rzchowski, and C. B. Eom, "Tailoring a two-dimensional electron gas at the $LaAlO_3/SrTiO_3$(001) interface by epitaxial strain." PNAS 108, 4720 (2010).

[147] W.M. Lü, X. Wang, Z. Q. Liu, S. Dhar, A. Annadi, K. Gopinadhan, A. Roy Barman, H. B. Su, T. Venkatesan, and Ariando, "Metal-insulator transition at a depleted $LaAlO_3/SrTiO_3$ interface: Evidence for charge transfer induced by $SrTiO_3$ phase transitions". APL99, 172103 (2011).

[148] F. W. Lytle, “X Ray Diffractometry of Low Temperature Phase Transformations in Strontium Titanate.” J. Appl. Phys. 35, 2212 (1964).

[149] E. Arslan, S. Bütün, S. Bora Lisesivdin, M. Kasap, S. Ozcelik, E. Ozbay, J. Appl. Phys. 103, 103701 (2008)

[150] H. J. Queisser, D. E. Theodorou, Phys. Rev. B 33, 4027 (1986)

[151] A. Rubano, D. Paparo, F. Miletto Granozio, U. Scotti di Uccio, L. Marrucci, Phys. Rev. B 76, 125115 (2007)

[152] A. Rubano, D. Paparo, M. Radović, A. Sambri, F. Miletto Granozio, U. Scotti di Uccio, L. Marrucci, Appl. Phys. Lett. 92, 021102 (2008)

[153] A. Rubano, D. Paparo, F. Miletto Granozio, U. Scotti di Uccio, L. Marrucci, J. Appl. Phys. 106, 103515 (2009)

[154] C. Bell, S. Harashima, Y. Kozuka, M. Kim, B. G. Kim, Y. Hikita, H.Y. Hwang, Phys. Rev. Lett. 103, 226802 (2009)

[155] C. Aruta, S. Amoruso, R. Bruzzese, X. Wang, D. Maccariello, F. Miletto Granozio, and U. Scotti di Uccio, Pulsed laser deposition of SrTiO3 /LaGaO3 and SrTiO3 /LaAlO3: Plasma plume effects, Appl. Phys. Lett. 97 (2010) 252105-(1-3)

[156] A. D. Caviglia, S. Gariglio, N. Reyren, D. Jaccard, T. Schneider, M. Gabay, S. Thiel, G. Hammerl, J. Mannhart, J.-M. Triscone., Nature (London) 456, 624 (2008).

References (Appendix)

[i] A. Asamitsu, Y. Tomioka, H. Kuwahara, Y. Tokura, Nature 388, 50 (1997).

[ii] N. Biškup, A. de Andrés, and J. L. Martinez, "Origin of the colossal dielectric response of $Pr_{0.6}Ca_{0.4}MnO_3$." PRB 72, 024115 (2005)

[iii] Silvana Mercone, Alexandre Wahl, Alain Pautrat, Michaël Pollet, and Charles Simon, "Anomaly in the dielectric response at the charge-orbital-ordering transition of Pr0.67Ca0.33MnO3." PRB 69, 174433 (2004); Claudy Rayan Serrao, A Sundaresan and C N R Rao. "Multiferroic nature of charge-ordered rare earth manganites." J. Phys.: Condens. Matter **19,** 496217 (2007)

[iv] V. G. Prokhorov, G. G. Kaminsky, V. S. Flis, and Young Pak Lee. "Temperature dependence of resistance of $Pr_{0.65}Ca_{0.35}MnO_3$ films prepared by pulsed laser deposition." Low Temp. Phys**.** 25, 792 (1999);

Y. P. Lee, V. G. Prokhorov , J. Y. Rhee, K. W. Kim, G. G. Kaminsky and V. S. Flis. "The controlled charge ordering and evidence of the metallic state in $Pr_{0.65}Ca_{0.35}MnO_3$ films." J. Phys.: Condens. Matter 12, L133-L138 (2000);

V. G. Prokhorov, K. W. Kim, and Y. P. Lee, "Transport of Carriers in Perovskite Oxides: Manganites, Cobaltites, Cuprates." Journal of Korean Physical Society 36, 398 (2000);

V.G. Prokhorov, G.G. Kaminsky, V.S. Flis, Y.P. Lee, K.W. Kim, I.I. Kravchenko. "Influence of charge ordering and phase separation on transport properties of $Pr_{0.65}Ca_{0.35}MnO_3$ films." Physica B: Condensed Matter 307, 239-246 (2001)

[v] L. V. Saraf, S. B. Ogale, Z. Chen, R. P. Godfrey, T. Venkatesan, and R. Ramesh, "Correlation of large dielectric response with the ordering transitions in $Pr_{0.67}Ca_{0.33}MnO_3$." PRB 62, R11 961 (2000)

[vi] A. Geddo Lehmann, F. Congiu, N. Lampis, F. Miletto Granozio, P. Perna, M. Radovic, and U Scotti di Uccio, Phys. Rev. B 82 (2010) 014415

[vii] A. Asamitsu, Y. Tomioka, H. Kuwahara, Y. Tokura, Nature 388, 50 (1997);

N. Biškup, A. de Andrés, and J. L. Martinez,"Origin of the colossal dielectric response of $Pr_{0.6}Ca_{0.4}MnO_3$." PRB 72, 024115 (2005);

Silvana Mercone, Alexandre Wahl, Alain Pautrat, Michaël Pollet, and Charles Simon, "Anomaly in the dielectric response at the charge-orbital-ordering transition of Pr0.67Ca0.33MnO3." PRB 69, 174433 (2004);

Claudy Rayan Serrao, A Sundaresan and C N R Rao. "Multiferroic nature of charge-ordered rare earth manganites." J. Phys.: Condens. Matter **19,** 496217 (2007)

[viii] Y. Tokura (Ed.), Colossal Magnetoresistive Oxides, Gordon & Breach Science Publishers, London, 1999

[ix] S. Parashar, E.E. Ebenso, A.R. Raju, C.N.R. Rao, "Insulator–metal transitions induced by electric and magnetic fields, in thin films of charge-ordered $Pr_{1-x}Ca_xMnO_3$." Solid State Communications 114, 295–299 (2000)

[x] A. Asamitsu, Y. Tomioka, H. Kuwahara, Y. Tokura, Nature 388, 50 (1997).

[xi] S. Schramm, J. Hoffmann and Ch. Jooss, J. Phys.: Condens. Matter 20 (2008) 395231.

[xii] S. Mercone, A Wahl,C Simon, and C Martin, Phys Rev B 65 214428 (2002);
A Guha, N Khare, A K Raychaudhuri and CNR Rao, Phys Rev B 62, R11941 (2000);
A Guha A K Raychaudhuri, A R Raju and CNR Rao, Phys Rev B 62, 5320 (2000)

[xiii] D. Polli, M. Rini, S. Wall, R. W. Schoenlein, Y. Tomioka, Y. Yokura, G. Cerullo, and A. Cavalleri. "Coherent orbital waves in the photo-induced insulator–metal dynamics of a magnetoresistive manganite." Nature materials 6, 643-647 (2007).